EXPERIMENTAL AND NUMERICAL INVESTIGATION OF AEROSOL SCAVENGING BY SPRAYS

A Dissertation

by

ANDREW S. GOLDMANN

Submitted to the Office of Graduate Studies of
Texas A&M University
in partial fulfillment of the requirements for the degree of

DOCTOR OF PHILOSOPHY

December 2009

Major Subject: Nuclear Engineering

EXPERIMENTAL AND NUMERICAL INVESTIGATION OF AEROSOL SCAVENGING BY SPRAYS

A Dissertation

by

ANDREW S. GOLDMANN

Submitted to the Office of Graduate Studies of
Texas A&M University
in partial fulfillment of the requirements for the degree of

DOCTOR OF PHILOSOPHY

Approved by:

Chair of Committee,	Yassin Hassan
Committee Members,	William Marlow
	Karen Vierow
	Debjyoti Banerjee
Head of Department,	Raymond J. Juzaitis

December 2009

Major Subject: Nuclear Engineering

ABSTRACT

Experimental and Numerical Investigation of Aerosol Scavenging by Sprays.
(December 2009)
Andrew S. Goldmann, B.S., University of New Mexico; M.S., University of New Mexico
Chair of Advisory Committee: Dr. Yassin Hassan

In the event of a hypothetical nuclear reactor accident, the combination of plant design, operator training, and safety procedures result in low level risks to the general public; however, an additional offsite consequence mitigation system has the potential to substantially decrease the amount of radioactive material that could reach a population zone in a postulated accident scenario. An experimental and numerical investigation of airborne particulate scavenging by water sprays was conducted as part of a consequence mitigation study. Previous researchers have experimentally studied the removal of aerosols by sprays, but only in a confined region. The experiment conducted in this research used an expansive region where sprays could significantly affect the flow fields in the spray region.

Experimentation showed an expected trend of higher particle collection efficiencies with increased residency time within the spray region, with the highest average overall collection efficiency found to be $70.6 \pm 3.2\%$ at an air flow rate of 0.53 m/s and a water flow rate of 0.84 gpm. This general trend is expected because a longer residency time leads to an increased probability of particle-drop interaction. Collection efficiencies were also found to increase with increased particle number density. The numerical investigation was done using a deterministic method and a Monte Carlo method. Each model shows promise based on theoretical limitations of drop size for the experimental conditions. The theory demonstrates that particle-drop relative

velocity as well as the sizes significantly affect collection efficiency. An alternative study was conducted to determine the collection efficiency of non-wettable particles since the dust used in the experiment is hydrophobic. Computational Fluid Dynamics (CFD) models were also performed to determine the flow fields that developed within the experiment spray region and substantiate differences in the experimental and numerical models.

This dissertation is dedicated to my family and friends.

ACKNOWLEDGMENTS

The author wishes to thank Dr. Yassin Hassan and Dr. William Marlow for providing technical insight and general guidance on the topic of this report, and to Dr. Karen Vierow and Dr. Debjyoti Banerjee for agreeing to serve on my committee. The author also would like to thank Carlos Ortiz and Jim Sweeny for their assistance with the experiment. A special thanks goes to Sandia National Laboratories and the Nuclear Regulatory Commission for funding this project, specifically Randy Gauntt (SNL) who encouraged me to work on the project. The author also appreciates the help of Steve Webb (SNL) with CFD questions, Lawrence C. Sanchez (SNL) for general guidance and encouragement, Aaron Totemeier for creating the LaTeXtemplate used for this dissertation, and Kevin Hogan for general help with LaTeXquestions and being a "sounding board" for ideas related to this topic.

NOMENCLATURE

Abbreviations:

AFR	Air Flow Rate
ANSI	American National Standards Institute
CCI	Core-Concrete Interaction
CD	Central Differencing
CFD	Computational Fluid Dynamics
CPU	Central Processing Unit
CV	Control Volume
DOE	Department of Energy
EPA	Environmental Protection Agency
ESF	Engineered Safety Feature
FV	Finite Volume
GSD	Geometric Standard Deviation
GTP	Generic-Tee-Plenum
HPS	Health Physics Society
ISO	International Standards Organization
LUD	Linear Upwind Differencing
MARS	Monotone Advection and Reconstruction Scheme
MCNP	Monte Carlo Neutral Particle Code
MMD	Mass Mean Diameter
NIOSH	National Institute for Occupational Safety and Health
NRC	Nuclear Regulatory Commission
PDPA	Phase-Doppler Particle Analyzer
RNG	Random Number Generator
SDOM	Standard Deviation of the Mean
VMD	Volume Mean Diameter

WFR	Water Flow Rate

Symbols:

a	Mean Inter-Particle Area
A	Area
C	Aerosol Concentration in Sampling Probe
C_c	Cunningham Collection Factor
C_D	Drag Coefficient
C_o	Aerosol Concentration in Free Stream
d	Diameter, m
$\bar{D}$	Mean Diameter
F_d	Drag Force
F_{dif}	Diffusiophoretic Force
F_e	Electrostatic Force
F_g	Gravitational Force
F_{th}	Thermophoretic Force
G	Multiplier for RNG
K	Constant
l	Length
m	Mass
M	M-Bit Integer for RNG
n	Concentration
n_d	Number of Drops per Spray Layer
N	Number of Measurements or Bins
N_D	Number Density
p_o	Initial Number of Particles
P_b	Legendre's Function of the First Kind
$\dot{Q}$	Mass Flow Rate

Q_b	Legendre's Function of the Second Kind
R	Random Number
Re	Reynolds Number
s	Mean Inter-Drop Length
S	Seed Number
Stk	Stokes Number
t	Time
u	Gas Velocity
v	Particle Velocity
V	Volume
$\bar{x}$	Mean Value of Measurements

Greek symbols:

β	Limiting Radius for Particle-Drop Interaction
δ	Uncertainty
η	Collection Efficiency
γ	Surface Tension
μ	Viscosity
ϕ	Velocity Potential
ψ	Stream Function
ρ	Density
σ_x	Standard Deviation of the Sample
$\sigma_{\bar{x}}$	Standard Deviation of the Mean
Θ	Sampling Probe Mis-Alignment Angle

Subscripts:

c	Collector
ds	Downstream Filter

g	Gas
i	i^{th} Measurement or Bin
l	Liquid
p	Particle
t	Total
us	Upstream Filter

TABLE OF CONTENTS

Page

Page

LIST OF TABLES

TABLE Page

LIST OF FIGURES

FIGURE Page

FIGURE Page

FIGURE Page

FIGURE Page

1. INTRODUCTION

When the term aerosol is used one typically thinks of propellants from cleaning products. Although this is not incorrect, it does not fully encompass the definition of an aerosol. An aerosol is any collection of solid or liquid particles that are suspended in a gas. This means that airborne biological material (e.g. pollen, viruses), clouds, dust, fumes, and smoke can all be considered aerosols [1].

There are several government agencies that are interested in aerosol research. The Environmental Protection Agency (EPA) and the National Institute for Occupational Safety and Health (NIOSH) are concerned with air quality control, with NIOSH focusing on workplace exposure to particulate matter [2], while the Department of Energy (DOE) and the Nuclear Regulatory Commission (NRC) are interested in controlling emissions of radioactive particulate matter in the event of a hypothetical nuclear reactor accident. While these agencies have specific reasons for their research, the impetus is the same: aerosol mitigation.

The genesis for this research is the potential benefit that an aerosol scavenging engineered safety feature (ESF) could provide in the event of a hypothetical nuclear reactor accident with releases to the environment. Aerosol scavenging can be achieved through chemical absorption, nucleation, and by impaction [3]. The focus of this research will be impaction scavenging since it is the primary removal mechanism for the aerosol sizes considered.

This dissertation follows the style of International Journal of Heat and Mass Transfer.

1.1 Radioactive Aerosols

Radioactive aerosols are aerosols that have an ionization potential associated with them. They can be generated in nature, cosmogenic or terrestrial origin, or by man-made activities [4]. Although the aerosols from terrestrial origin (radon and thoron) are of some concern, the motivation for this research is due to radioactive aerosols from a hypothetical nuclear reactor accident.

Radioactive aerosols can be generated in a severe accident from overheating of the reactor leading to melting of the core and its structural components or from core-concrete interactions (CCIs) in the event of vessel failure [5]. In both cases, aerosols form when vapors from the melt and/or CCIs are transported to a cooler region and condense. When aerosols are generated purely from a melted core, the aerosol composition is typically between one-quarter and one-half volatile fission products with the remainder being control and structural material [6].

The size of radioactive aerosols in a nuclear power plant environment can be $0.1\mu m$ or larger [4]. The wide range of sizes are due to the complex environment in which vaporization, condensation, fragmentation, and coagulation can all occur. The smaller particles are typically generated by condensation or combustion processes while the larger particles are generated by mechanical processes such as fragmentation [4]. The size of aerosols is important to know because human respiratory deposition is size dependent, with the largest deposition fraction of about 90% occuring at discrete values of $4\mu m$ and $0.01\mu m$ [1]. The result of removing these discrete particle sizes from the atmosphere is a significant reduction in dose to plant workers, first responders, and the general public in the event of a hypothetical reactor accident with releases to the atmosphere.

1.2 Containment Aerosol Removal

The removal of aerosols inside reactor containment can be accomplished by natural or engineered processes. The natural processes that remove aerosols in containment include coagulation, Brownian diffusion, turbulent diffusion and inertia, thermophoresis, diffusiophoresis, and gravitational settling [7]. Engineered systems that remove aerosols include containment and drywell sprays, steam suppression pools, and ice condensers.

Although the engineered systems help remove aerosols from the containment atmosphere, they were not originally designed for that purpose. All three engineered systems were designed to suppress steam pressurization during design basis accidents [8, 9]. While these systems are effective at reducing airborne particles within the containment, there currently are no engineered system that remove aerosols from the environment in the event of containment failure or containment bypass failures.

1.3 Research Goals

There are three main goals of this research, the first of which was to perform an experimental study of the effectiveness of water sprays at removing airborne contaminants. The experiment was designed to simulate an aerosol release to the environment with sprays as the means of removal. The airborne contaminant was simulated using a non-radioactive, non-hydrophobic standardized test dust. The test dust does not simulate all the physics of aerosols released during a severe reactor accident, but is sufficient for demonstrating the primary removal mechanism.

The second goal was to compare the experimental results to a theoretical analysis of the problem. A deterministic method for aerosol collection by sprays developed by Cheng [10] was used for the analysis. A Monte Carlo approach was then developed and compared to the deterministic analysis results. Unfortunately, the only available impaction collection efficiency curves are for hydrophobic aerosols. A the-

oretical analysis of impaction collection efficiency due to a spherical obstacle for non-hydrophobic aerosols was conducted to rectify this deficiency.

Finally, Computation Fluid Dynamic (CFD) simulations were performed as a supplement to the experimental and theoretical studies. The third goal is to use the results from the CFD simulations to characterize the flow fields generated by the sprays where experimental data was either ambiguous or unavailable and are used to explain the differences in experimental and theoretical results. The CFD software chosen for this project was STAR-CD, which is a commercially available code. STAR-CD has the ability to model water sprays but does not have the ability to model collisions between aerosol and spray droplets.

2. PREVIOUS RESEARCH

Aerosol mitigation has multiple applications in several fields. For example, dust control is important for reducing worker related illnesses and prevention of dust explosions in geological mining operations [10, 11], gaseous scavenging is used to help facilitate chemical reaction [12], and in the era of atmospheric nuclear weapons testing research was required to study the washout of radionuclides by rain [13–15]. As a result, experimental and analytical research has been conducted on a "micro" scale, focusing on collection by individual spherical body collectors, and on a "macro" scale, by studying the collection of aerosols by sprays.

2.1 Distinct Drop Collection

The main focus of this research is aerosol mitigation by sprays, but it is beneficial to understand the physics of aerosol collection by a distinct drop before exploring collection by sprays. Collection efficiency can generally be defined as the ratio of the cross-sectional area of the original aerosol stream, created by the grazing trajectory of the aerosol particle, to the total cross-sectional area of the collector [16], an example of which can be seen in Figure 2.1. Since both the cross-sectional areas are taken to be a circle, the ratio can be describe as a ratio of the radii, with the original aerosol stream from the grazing trajectory definded as β and the collector defined as R, as seen in Figure 2.1. Prior experimental and theoretical research related to distinct drop collection will be presented in the following sections.

2.1.1 Experimental Work

There are few experimental studies regarding the collection of aerosol particles by spherical body collectors. The majority of the published and referenced work found are from the 1950s [16] and 1960s [17, 18], which are still being used today as

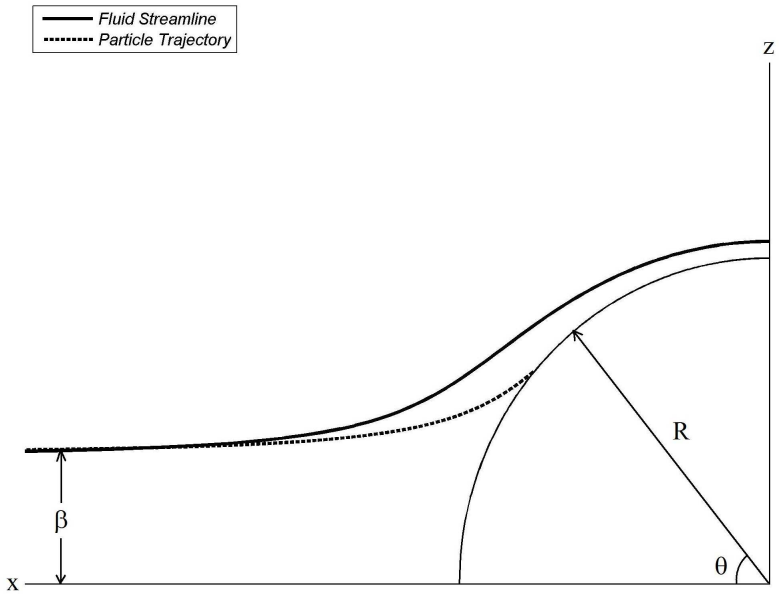

Fig. 2.1. Particle Trajectory

a comparison to theoretical work. Each study uses a unique aerosol material and measurement methods, details of which will be discussed.

Ranz and Wong

Ranz and Wong [16] conducted their work in the early 1950s at University of Illinois. They were interested in collection of dust and smoke particles for air cleaning equipment. They approached the problem by first considering the fundamental physics involved in aerosol particle motion and developed a mathematical statement of the problem. They compared their theoretical work with those of previous researchers and then carried out experimental research to verify the theory. This section will focus on their experimental work and results.

The spherical body collector used in the experiment was a 900 micron diameter platinum sphere that was formed by melting the end of a 5-mil platinum wire. The collector was placed in a venturi-shaped nozzle through which the aerosol stream

could be direct during the test runs. The relative velocities of the aerosol stream used in these studies were 1.2 to 9.7 m/s. The amount of impacted aerosols was found by measuring the difference in conductance of a water bath before and after washing the spherical collector.

The aerosol was generated from a condensation aerosol generator, using concentrated sulfuric acid as the aerosol material. The acid concentration in the aerosol particles was said to be nearly constant at 50.5 weight% sulfuric acid. The aerosol particles produced by the generator had a uniform diameter in the range of 0.3 to 1.4 microns at a generation rate of 1.0 to 1.5 milligrams of aerosol material per minute.

The experimental data of Ranz and Wong [16] is presented as a figure, of which the numerical data is difficult to obtain. Therefore, the experimental data presented in Figure 2.2 are estimated from the figure presented in Ranz and Wong [16], and several other references [19–22]. The figure shows the collection efficiency with respect to the Stokes number (Stk), which is the ratio of the stopping distance of the particle to the characteristic dimension of the obstacle. The Stokes number is defined as [1],

$$Stk = \frac{\rho_p u d_p^2 C_c}{9\mu_g d_c} \tag{2.1}$$

where ρ_p is the particle density, u is the velocity, d_p is the particle diameter, C_c is the Cunningham correction factor, μ_g is the gas viscosity, and d_c is the collector diameter. The Cunningham correction factor is a correction for slip near the surface of a particle. Typically the gas velocity near the surface is taken to be zero, but this assumption does not hold for small particles, whose size is close to the gas mean free path. For this research, however, C_c is taken to be unity because the size of the dust particles are greater than $1\mu m$, which is where the correction becomes less significant.

Figure 2.2 is representative of inertial impaction only, since impaction by interception and electrophoresis is considered to be negligible. There were no values of the collection efficiency, η, measured beyond 80% because the experimental conditions for high efficiencies caused re-entrainment of aerosol particles that had already

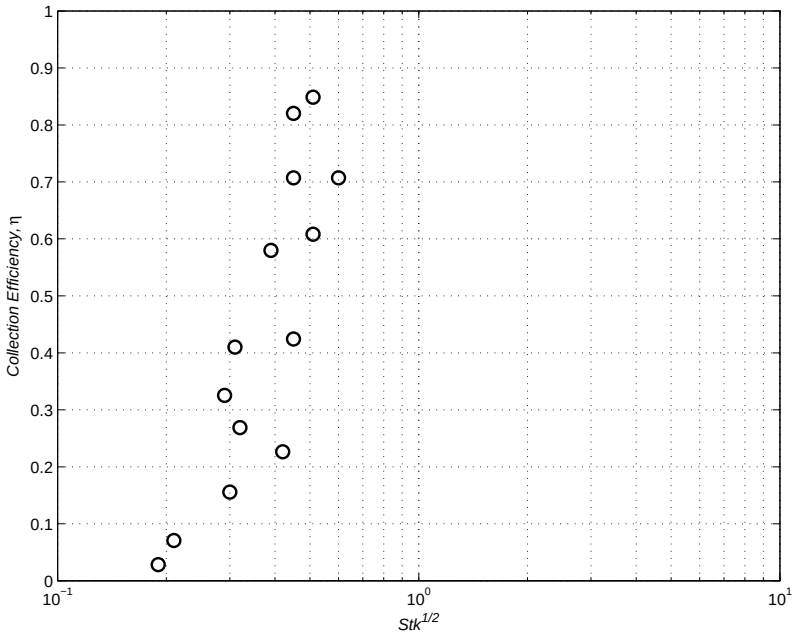

Fig. 2.2. Impaction Collection Efficiency of Sulfuric Acid Aerosols on a Spherical Body Collector [16]

been collected. The authors note that their experimental data follows the theoretical curve of Langmuir and Blodgett [23], which will be presented in Section 2.1.2, closely at low efficiencies, but is above the theoretical curve at higher efficiencies.

Walton and Woolcock

Walton and Woolcock [17] noted that a system comprised of a dust cloud and water sprays is extremely complex, and therefore decided to simplify the problem by considering the action of one water drop moving through the dust cloud. There dust collection research was primarily focused on applications in the mining industry. They employed two methods for determining the impaction collection efficiency experimentally. The first method allowed water drops to fall through a static dust cloud, while the second method reversed the process and had a dust cloud flowing past a water drop.

The stationary cloud method consisted of a steady stream of uniform water drops falling through a static cloud of dust particles in a closed chamber. The uniform size water drops were formed by use of a micro-burette, which provided a continuous stream of drops from the tip of a hypodermic needle. The drop size was regulated by a controlled air flow over the tip of the needle. The dust cloud was made by a spinning disk sprayer, which creates the dust by feeding a liquid onto a rapidly rotating disk. The dust size created by this method yielded particle sizes of 15 to 50 microns in diameter depending on the speed of the rotating disk. Dust particles were made of methylene blue ($C_{16}H_{18}N_3SCl$), which yields a blue solution when dissolved in water.

In the aforementioned method, the stream of drops were directed to fall through a small entrance hole at the top of the chamber and out an exit hole into a glass jar. The velocity of the drops was measured by a photographic method using stroboscopic illumination. Aerosol particles that exited the chamber were kept from entering the glass jar by use of a horizontal air flow that was sufficient to remove the particles but too small to affect the falling drop. The amount of dust collected by the falling drops was determined by measuring the density of coloration, due to the methylene blue, with a spector-photometer.

A practical limitation of this method was that it was extremely sensitive to collection of particles smaller than 12 microns due to the drop residency time in the dust cloud. Particle sizes larger than 12 microns could not be used because the cloud concentration measurement could not produce accurate or reliable results. As a result, only a limited number of experiments were conducted with this method.

The experiment was carried out for drop diameters, d_c, of 2600 microns and 500 microns with dust particle diameters, d_p, of 48 microns and 12 microns. The smaller water drops reached their terminal velocities while the larger ones did not. The dust particle density, ρ_a, is 1300 kg/m^3 and the carrier gas density, ρ_g, and viscosity, μ_g, were taken to be 1.2 kg/m^3 and $1.8E-05 kg/m \cdot sec$, respectively. Table 2.1

presents the results collected for the stationary cloud method. They show that the collection efficiency increases with increasing aerosol diameter and decreasing drop diameter. It should be recalled however that the larger drops did not reach their terminal velocities.

Table 2.1
Stationary Cloud Method Experimental Results

Drop Diameter $[\mu m]$	**Aerosol Diameter** $[\mu m]$	**Velocity** $[m/sec]$	**Collection Efficiency** $[\eta]$
2600	48	3.3	0.79
2600	12	3.3	0.36
500	48	2.1	0.96
500	12	2.1	0.57

The stationary drop method was developed to overcome the difficulties of stationary cloud method. In the stationary drop method the dust cloud is carried past a static drop. This method allowed the researchers to increase the residency time and use particles smaller than 12 micron, although a disadvantage of this method was the amount of liquid available for post experiment measurements.

The dust cloud was created of the same material (methylene blue) and formed in the same manner as described in the stationary cloud method. The dust was made to travel upward through a vertical tube toward the static water drop. Dust velocities could be determined by the known diameter of the tube and the measured air flow rate, but was also measured by stroboscopic illumination photography. The water drop was suspended from a fine glass capillary tube and placed in the central region of the vertical tube. The size of the drop was controlled by a micrometer syringe and measured with the aid of a microscope.

The experiment used drops that were 500 to 2000 microns in diameter and dust particles that were in the respirable range (less than 5 microns in diameter). The relative drop velocity ranged from 2.0 to 6.7 m/s, and could be controlled by simply adjusting the cloud velocity. The results of the experiment are shown in Figure 2.3.

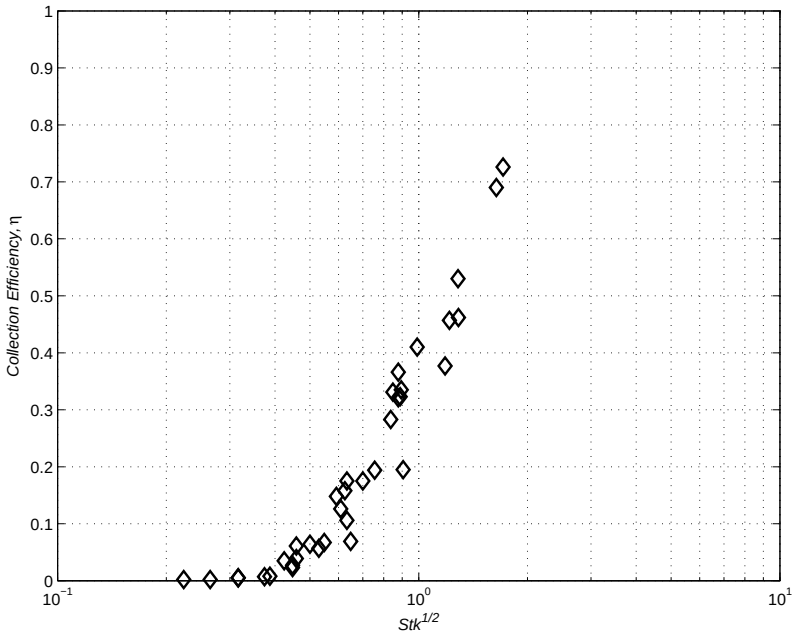

Fig. 2.3. Impaction Collection Efficiency of Methylene Blue Aerosols on a Spherical Body Collector [17]

Starr and Mason

Starr and Mason [18] conducted a set of experiments in the mid-1960s. They were interested in the removal of industrial pollutants, biological organisms and dust, and radioactive debris from the atmosphere by falling raindrops and snowflakes. They used three types of aerosol particles for their experiments including Lycoperdon spores ($d_p = 4.5\mu m$), Ustilago Nuda spores ($d_p = 5.2\mu m$), and grains of Paper Mulberry pollen($d_p = 12.8\mu m$), all of which were chosen because of their nearly spherical shape.

The water drops of uniform size were produced using the same method as in the Walton and Woolcock stationary cloud method. Again, that method delivered a steady flow of water to a hypodermic needle where the drops were blown off by a regulated flow of air. The drop sizes are determined by collecting them on a strip of photographic film. When the drops impact the film they produce a circular stain that is a function of their diameter and independent of the drop velocity. During an experimental run the film is replaced with a clean glass plate, where the drops are collected and the particles are later counted. The aerosol particles are injected into the system by use of a bursting-diaphragm, which bursts at about 7 atmospheres, but the procedure allows the region to reach steady state before the drops are allowed to fall through. Figure 2.4 presents the results of these experiments.

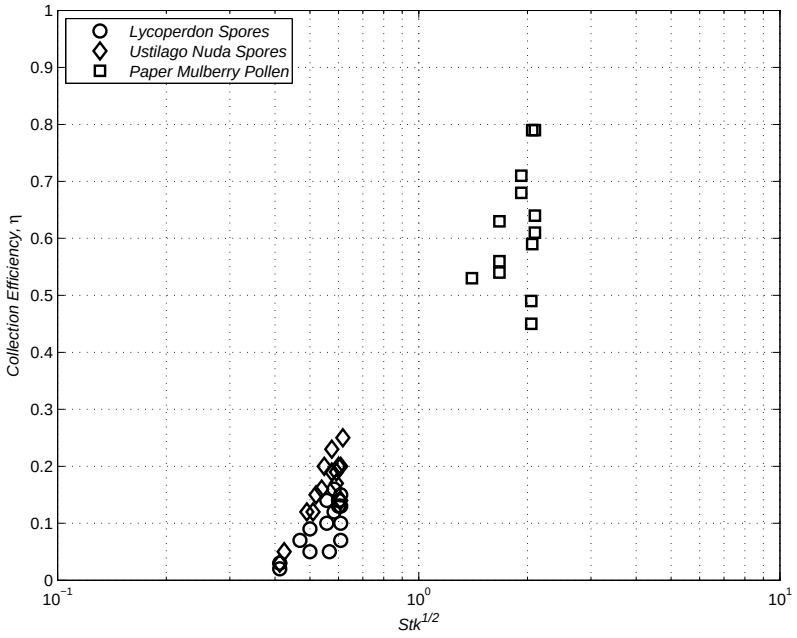

Fig. 2.4. Impaction Collection Efficiency of Several Organic Aerosols on a Spherical Body Collector [18]

The largest source of data errors come from particle counting. Other sources of error are from the drop size and velocity measurements as well as any type of

inhomogeneities in the dust cloud. The overall probable errors for collection efficiency range from 10 to 20 percent for large to small drops, respectively.

Experiment Comparison

A quick comparison of the experimental data presented in Section 2.1.1 exhibit a disparity between the Ranz and Wong data to the other data, as can be seen in Figure 2.5. Ranz and Wong show a higher collection efficiency at smaller Stokes numbers. Prodi [21] suggests that the data taken by Ranz and Wong was done at Reynolds Numbers (Re) greater than 1000. It is possible that the strategy of using a platinum spherical collector, and the method used to create the collector, could produce independent results. Another possible explanation for the higher collection efficiency would be that some of the sulfuric acid aerosol particles could have been collected by the platinum wire aft of the sphere. This is because the way the collection was measured was by washing the sphere and wire in a water bath and measuring the change in conductance.

2.1.2 Theoretical Approach

Theoretical studies on collection efficiency have been conducted by a number of researchers [19, 21–27], all of which have used the same basic strategy to solve the problem. The approach involves solving a system of equations describing the flow around a sphere and the equation of motion for a particle contained in that flow. This section will discuss the system of equations used to solve the collection efficiency problem.

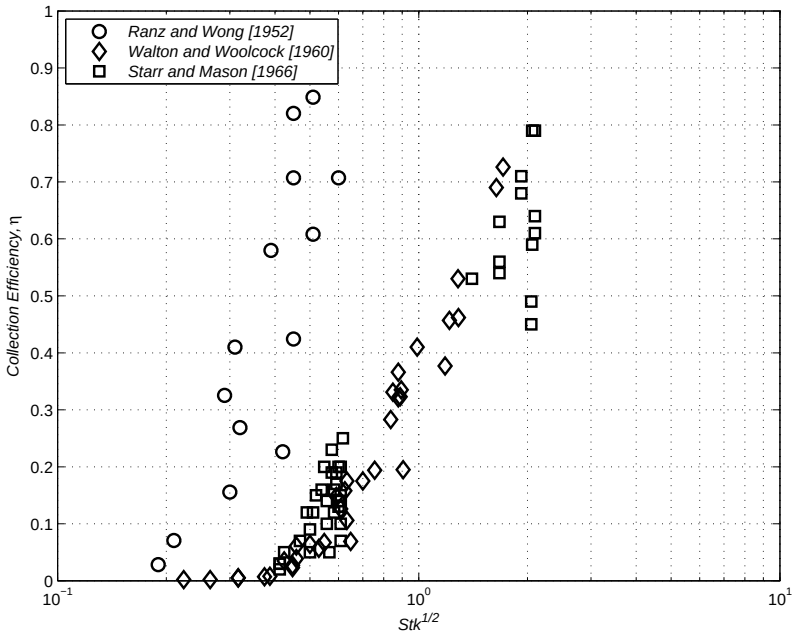

Fig. 2.5. Impaction Collection Efficiency on a Spherical Body Collector

Flow Around a Sphere

A simplifying assumption has been made by earlier researchers to solve for the fluid flow field around a sphere. The assumption is that the flow field can be described by an inviscid, irrotational, and incompressible flow. Pemberton [28] suggests that as long as the ratio of the aerosol particle size to the collector size is small, that it is reasonable to assume potential flow. The equations that describe potential flow around a sphere are given as [27],

$$u_{g,x} = 1 - \frac{2x^2 - y^2}{2(x^2 + y^2)^{2.5}} \tag{2.2}$$

$$u_{g,y} = \frac{-3xy}{2(x^2 + y^2)^{2.5}} \tag{2.3}$$

The derivation of Equations 2.2 and 2.3 are not defined in the searched literature. Dorsh [26] suggests they are derived from the classical equation for nonviscous flow

about a sphere. A method for solving the potential flow field around a sphere using Stokes stream functions is described later in Section 4.3.

Particle Equation of Motion

Newton's second law of motion is used to calculate the aerosol particle trajectory. Newton's second law states that the sum of the forces on a particle equals its mass times acceleration, $\Sigma F = ma$. When expanded, this equation takes the form [21]

$$m\frac{dv_p}{dt} = F_g + F_d + F_{th} + F_{dif} + F_e \tag{2.4}$$

where F_g is the force due to gravity, F_d is the drag force, F_{th} is the thermophoretic force, F_{dif} is the diffusiophoretic force, and F_e is the electrostatic force. The gravitational, drag, and electrostatic forces are relatively self-explanatory, although the drag force will be discussed in further detail later in this section. The thermophoretic force is the force due to molecular collisions with the particle in a temperature gradient, which results in a force diametric to the gradient. The diffusiophoretic force exists when there is a molecular concentration gradient, typically in the presence of condensation or evaporation [21].

Certainly, there are other forces that may apply to a specific analysis, in which case they would need to be addressed. For example, for extremely small particles Brownian motion becomes a significant factor in particle collection. Typically, most of the forces are considered to be negligible when calculating the inertial impaction efficiency curve, with the exception of the drag force.

The drag force can be described by the general form of Newton's resistance equation, given by Equation 2.5. Equation 2.5 reduces to the drag force due to Stokes's law for $Re < 1$, given by Equation 2.6. The coefficient of drag for a sphere is dependent on Re, and is given by Equation 2.7 [1].

$$F_d = C_D\frac{\pi}{8}\rho_g d_p^2 v^2 \tag{2.5}$$

$$F_d = 3\pi\mu v d_p \tag{2.6}$$

$$C_D = \begin{cases} \frac{24}{Re} & Re < 1 \\ \frac{24}{Re}(1 + 0.15Re^{0.687}) & 1 \leq Re < 1000 \\ 0.44 & Re \geq 1000 \end{cases} \tag{2.7}$$

The drag force is decomposed into its x and y components and used to solve the equation of motion. The velocity, v, is replaced with the relative velocity, $(u_g - v_p)$, in the drag force and Reynolds equations. In the case of Equation 2.5, v^2 is replaced with $(u_g - v_p)|u_g - v_p|$. This treatment will not only give the magnitude of the drag force but also the direction. The relative velocity is used because the particle is initially taken to be moving with the streamlines when it is far away from the obstacle, therefore the relative velocity defines the change in forces when the particle starts to deviate from the streamline.

Discussion of Results

Earlier researchers solved for the grazing trajectory with the aid of differential analyzers [23] or modern computers [29]. Langmuir and Blodgett [23] did the earliest found theoretical study for impaction collection efficiency. They derived an equation for impaction collection efficiency with a spherical body collector in an ideal flow given by,

$$\frac{\eta}{1-\eta} = 0.82\left[Stk - \frac{1}{12}\right]^{1.04} \tag{2.8}$$

Slinn [29] solved a somewhat more complicated set of equations describing the particle flow and trajectory. The semi-empirical relationship derived from that set of data is given by,

$$\eta = \left[\frac{Stk - \frac{1}{12}}{Stk + \frac{7}{12}}\right]^{\frac{3}{2}} \tag{2.9}$$

The results of these separate analyses are shown in Figure 2.6. As can be seen by Figure 2.6, the result arrived at by Slinn is not so different than that arrived at by Langmuir and Blodgett. When compared to the experimental work, found in Figure 2.7, the theoretical analysis is in good agreement with the work done by Walton and Woolcock.

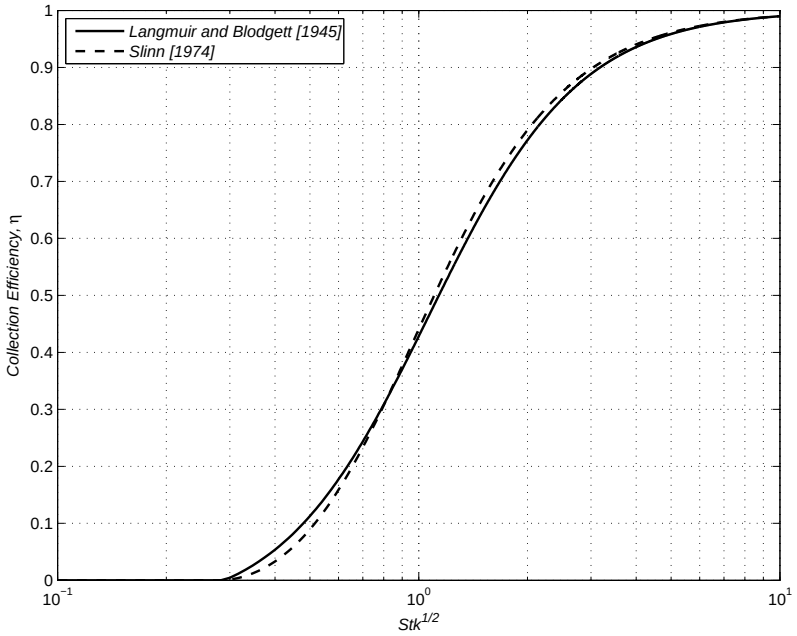

Fig. 2.6. Theoretical Approximations of Impaction Collection Efficiency

Recall, most of the body and surface forces on the particle were ignored in the calculation. This suggests that the agreement with experimental research [17, 29] confirms that the dominating force in an inertial impaction calculation is the drag force. Possible reasons for the disparity with the Ranz and Wong research have been discussed previously in Section 2.1.1.

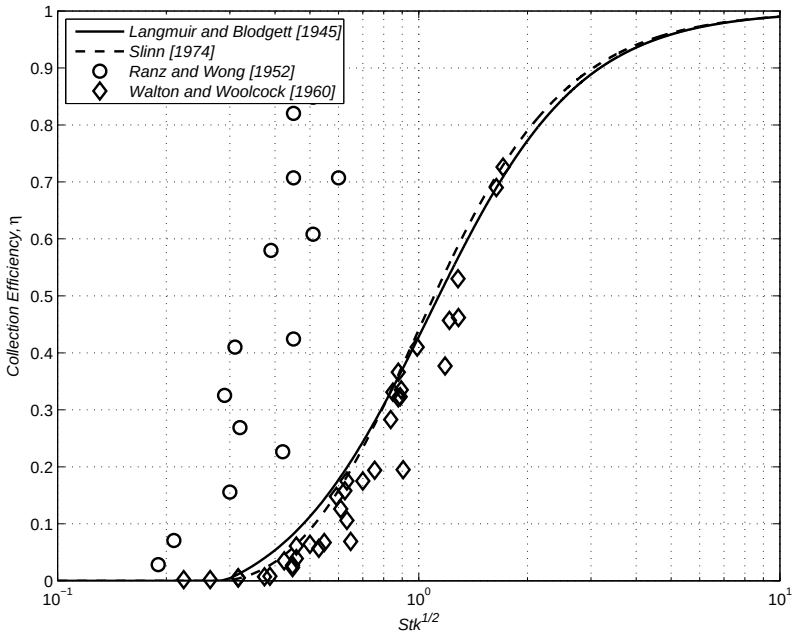

Fig. 2.7. Comparison of Theoretical and Experimental Impaction Collection Efficiency

2.2 Collection by Sprays

Collection efficiencies by sprays, including gravity driven sprays (*e.g. rain*) and high pressure sprays, have been studied less than due to discrete drops. This may be attributed to the added complexity of the system and the difficulty controlling some of the variables. Systems with sprays have a size distribution of drops that can can interact with both aerosol particles and other drops. The flow fields produced by multiple drops can also add an element of uncertainty. These conditions do not lend themselves to an experimentally or theoretically friendly situation.

2.2.1 Experimental Work

Experimental work has been done regarding the scavenging action of rain [13, 30] and the collection efficiency due to high pressure sprays [11, 31]. A disadvantage of

the work studying the scavenging action of rain is that a plethora of experimental variable are difficult to control, since experiments were conducted outdoors. As a result, the work presented in this section are from high pressure spray experiments, more specifically the work done by Tomb *et al.* [11]. These experiments also more closely match the conditions of the experiment conducted in this research.

Tomb *et al.* [11] were conducting a laboratory investigation of the effectiveness of doped and un-doped sprays at controlling respirable coal dust. They used pulverized Pittsburgh coal dust that was maintained at a concentration of about 40 mg/m^3 and had an upper size limit of 75 μm. The dust was given a velocity of 100 fpm in an 18 in diameter duct that was 25 ft long. The spray was located in the center of the duct and oriented parallel and counter-current to the flow of aerosols.

Dust samples were taken upstream and downstream of the spray using impingers. The air flow rate through the impingers was maintained at 0.1 cfm. The samples were analyzed with a Model T Coulter counter calibrated to measure particles 0.68 to 1 μm and 1 μm bin sizes after that up to 10 μm. Tests were initially performed without sprays to determine the aerosol concentration gradient across the duct as well as aerosol wall deposition. Those tests proved that the aerosol loss between the impingers was negligible and that single point measurement at the center of the duct was representative of the concentration and size distribution across the cross-section of the duct.

Tomb *et al.* selected four spray nozzles for their experiments. Each nozzle was used at four operating pressures and three tests were run at each pressure. Only nozzle four was used for the experiments with added surfactants. Table 2.2 [11] presents the matrix of nozzle operational parameters for the un-doped cases. Velocities were estimated from Bernoulli's equation.

The results follow a general trend similar to the trend found in the discrete drop experiments. The collection efficiency increases with increasing velocity, in the case of the experiments conducted by Tomb *et al.* this corresponds to the increased

Table 2.2
Spray Nozzle Operational Parameters

Nozzle	**Pressure** $[psig]$	$\dot{Q}$ $[gal/min]$	$\bar{D}$ $[\mu m]$	**Velocity** $[m/sec]$
1	60	0.49	950	25.85
1	100	0.63	670	33.40
1	150	0.78	630	40.80
1	200	0.90	460	47.20
2	60	0.78	360	15.80
2	100	1.01	300	20.50
2	150	1.24	250	25.00
2	200	1.43	225	28.90
3	60	1.18	400	15.80
3	100	1.52	340	20.50
3	150	1.86	280	25.00
3	200	2.15	250	28.90
4	60	1.70	500	15.80
4	100	2.20	450	20.50
4	150	2.70	390	25.00
4	200	3.10	325	28.90

nozzle pressure. The collection efficiency also increases with an increased flow rate. Figures 2.8 to 2.11 show the results from the un-doped experiments. Experiments with the added surfactants showed a greater collection efficiency of about 10%. No explanation is given as to why the surfactant would increase collection efficiency, but it is probably due to the reduced liquid surface tension. The decrease in surface tension reduces the required velocity that the particle must have to be collected by the drop. This phenomenon will be discussed in Section 4.3.

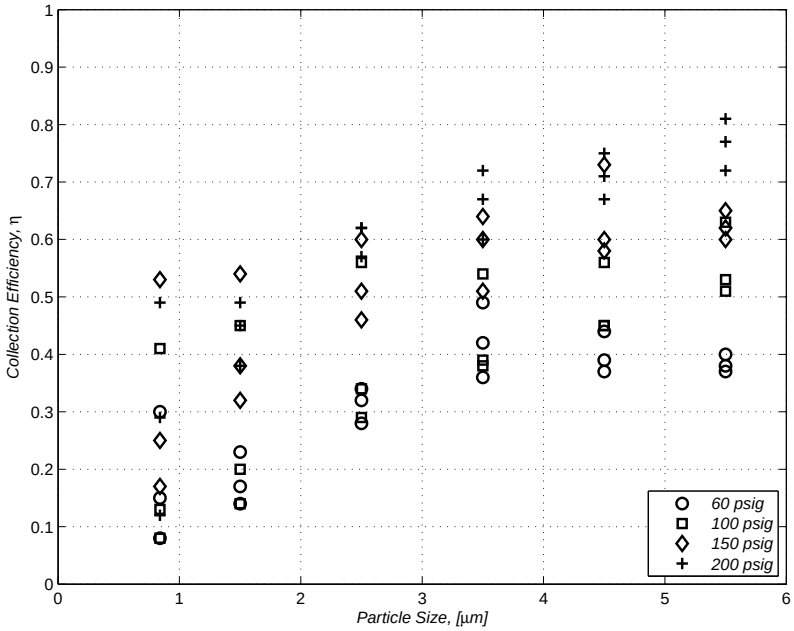

Fig. 2.8. Nozzle 1 Suppression Efficiency for Tomb *et al.* Experiments [11]

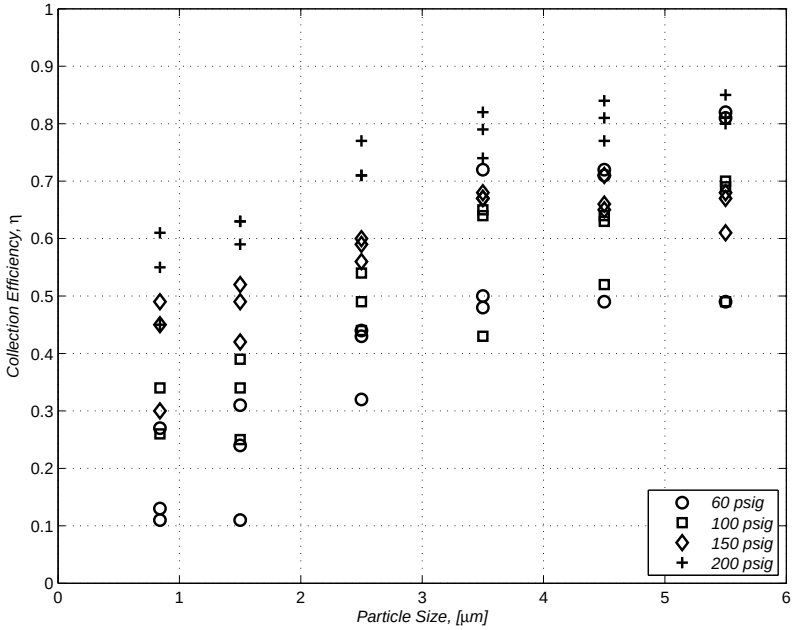

Fig. 2.9. Nozzle 2 Suppression Efficiency for Tomb *et al.* Experiments [11]

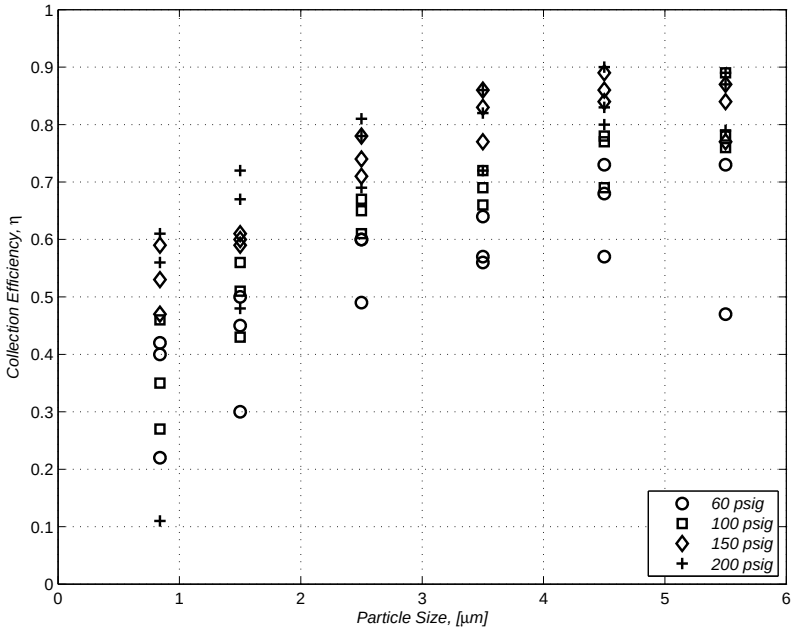

Fig. 2.10. Nozzle 3 Suppression Efficiency for Tomb *et al.* Experiments [11]

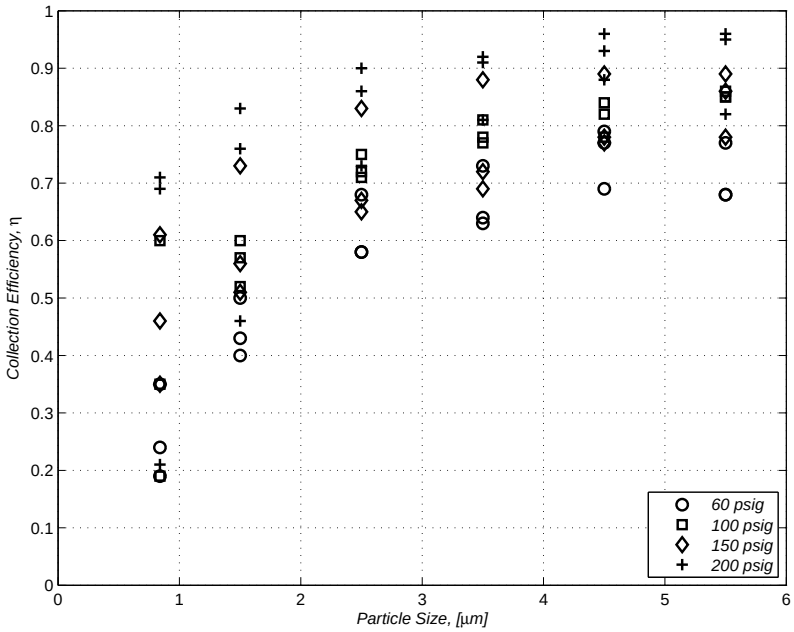

Fig. 2.11. Nozzle 4 Suppression Efficiency for Tomb *et al.* Experiments [11]

2.2.2 Theoretical Approach

Researchers [10, 15, 17, 28] have taken various approaches to solve the collection efficiency of water sprays. A simplified technique taken by Walton and Woolcock [17] will be presented in this section as an introduction to the theory. The detailed procedure taken by Cheng [10] will be discussed in Section 4.1. The reader is directed to Greenfield [15] and Pemberton [28] for yet another approach to the problem.

Walton and Woolcock [17] begin their analysis by considering the simple case of a spray falling under the effect gravity. In this case, the spray is taken to be uniformly distributed across an area, A. If a volume of water, V, is transformed into a spray with drops of diameter, d_c, then the cross-sectional area swept out by the drops is

$$\frac{\frac{1}{4}V\pi d_c^2}{\frac{1}{6}\pi d_c^3} = \frac{3V}{2d_c} \tag{2.10}$$

If we now take the definition for collection efficiency from the discrete drop study and apply it to Equation 2.10 we can estimate the total area of cleared aerosols to be $\frac{3V\eta}{2d_c}$. The fraction of aerosols removed from the total area, A, will then be

$$\frac{\Delta n}{n} = \frac{3V\eta}{2Ad_c} \tag{2.11}$$

where n is the aerosol concentration. Equation 2.11 is only the amount of aerosol removed through a single layer of spray. The solution for multiple layers of spray is given by

$$n = n_o e^{\left[\frac{-3V\eta}{2Ad_c}\right]} \tag{2.12}$$

where n_o is the initial aerosol concentration.

The results for the collection efficiency of a gravity driven spray, with an aerosol density of 1370 kg/m^3, are shown in Figures 2.12 to 2.15 compared to the collection efficiency of the high pressure sprays. The data was obtained using the discrete drop collection efficiency results experimentally determined by Walton and Woolcock [17] and Equation 2.12. It is clearly visible that the higher drop velocities have a better

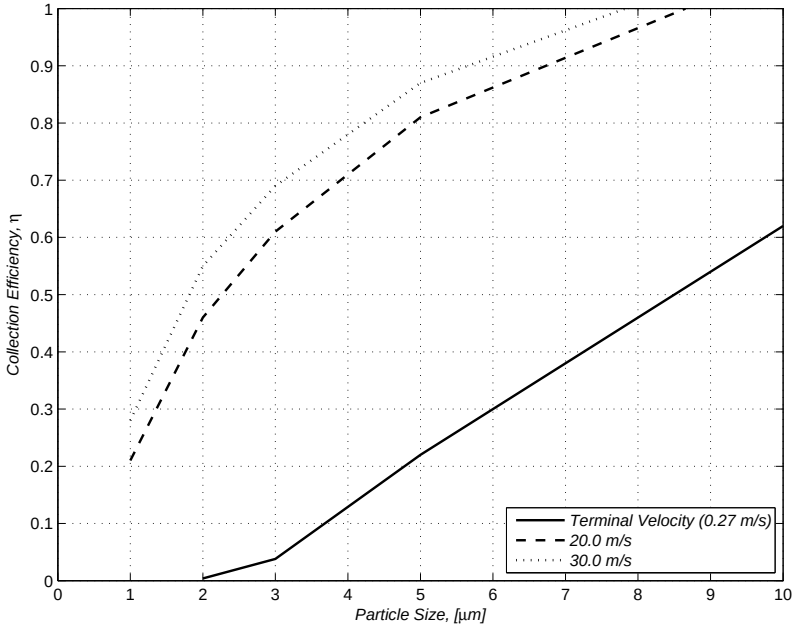

Fig. 2.12. Spray Theoretical Collection Efficiency, $d_c = 100\mu m$

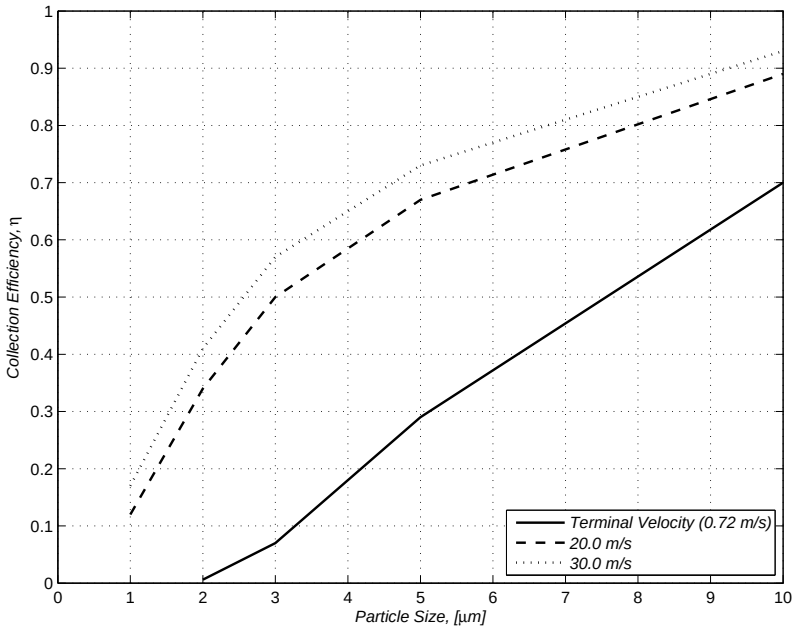

Fig. 2.13. Spray Theoretical Collection Efficiency, $d_c = 200\mu m$

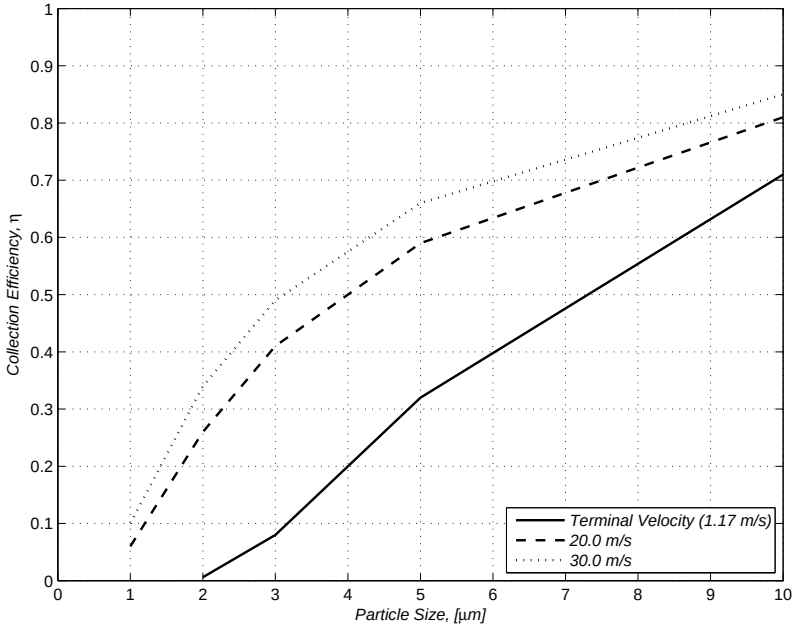

Fig. 2.14. Spray Theoretical Collection Efficiency, $d_c = 300\mu m$

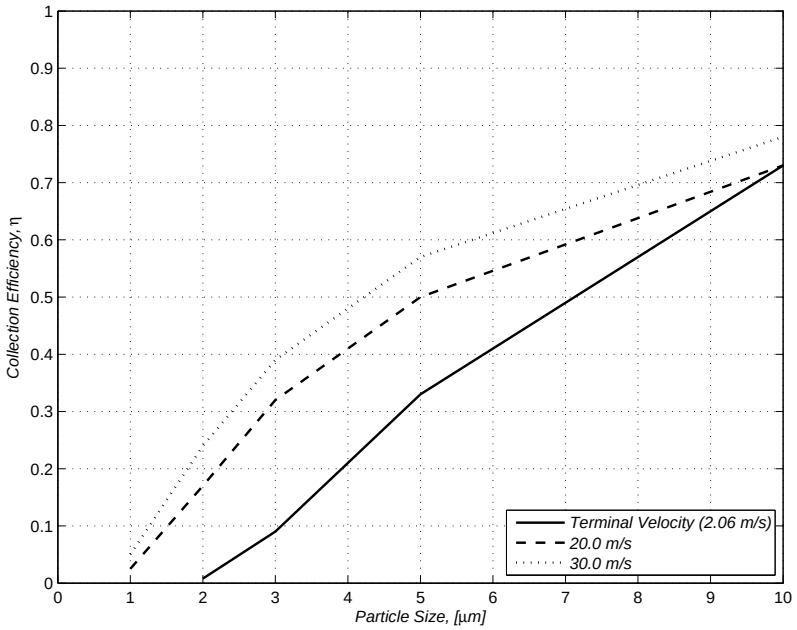

Fig. 2.15. Spray Theoretical Collection Efficiency, $d_c = 500\mu m$

collection efficiency, although that benefit decreases slightly as the drop size becomes larger.

An interesting comparison made by Walton and Woolcock is the volume of water required to remove 90% of airborne dust ($\rho_p = 1370 kg/m^3$). Significant reductions in water volume are needed for the higher spray velocities for the smaller diameter aerosol particles. There is a diminishing return as the aerosol particles become larger. Table 2.3 presents these results [17].

Table 2.3
Gallons of H_2O Required to Remove 90% of Airborne Dust per 1000 ft^3

Drop Diameter $[\mu m]$	**Aerosol Diameter** $[\mu m]$	**Drop Falling at Terminal Velocity**	**Drop Falling at 20 m/s**	**Drop Falling at 30 m/s**
100	2	240	8.8	5.6
100	3	90	6.5	4.5
100	5	6.8	5.0	3.6
100	10	1.0	3.8	2.8
200	2	240	7.7	5.2
200	3	40	5.3	3.8
200	5	9.2	3.9	2.9
200	10	1.5	3.0	2.3
300	2	260	8.2	5.2
300	3	26	5.2	3.6
300	5	6.8	3.6	2.7
300	10	1.9	2.6	2.1
500	2	160	10.1	6.0
500	3	22	5.4	3.7
500	5	6.7	3.5	2.5
500	10	2.6	2.4	1.9

3. EXPERIMENT

An experiment studying the collection of aerosol particles by sprays was completed at Texas A&M University's Riverside Campus to complement the data that has been obtained by previous researchers. The goal of the experiment was to determine the collection efficiency of a poly-disperse aerosol by high pressure spays. The experiment setup and procedure will be discussed in the following sections along with the methods used to post-process the raw data and the results and analysis.

3.1 Setup

The experimental setup can be divided into two regions. The upstream region, where the dust induction system, generic-tee-plenum, and upstream aerosol sampling probe are located and the spray and downstream region, which consists of an expansive region where five spray nozzles are located and a downstream aerosol sampling probe. All duct work used to connect regions of the experiment are cylindrical with a diameter of 14 inches. The experiment also required ancillary equipment and materials.

3.1.1 Upstream Region

The dust induction system consists of a high capacity blower and the dust atomizer system. The blower has a capacity of 60,000 cfm, but only a small fraction of this capacity is used for the experiment (roughly 1500 cfm). The dust atomizer system is essentially the same as an air assisted atomizer nozzle [32]. The air flow from the blower entrains a stream of slow moving stirred dust into the upstream duct work by use of the pressure differential created by the two flows.

The flow from the dust induction system advances to a generic-tee-plenum (GTP), see Figure 3.1. The GTP is basically a rectangular mixing chamber used when a 90°

change of direction in the flow is desired. The mixing chamber is needed because the same forces discussed for collection by body collectors are at work anytime the flow changes direction. For example, a smooth changing 90° elbow will produce a particle size gradient across the cross section of the duct.

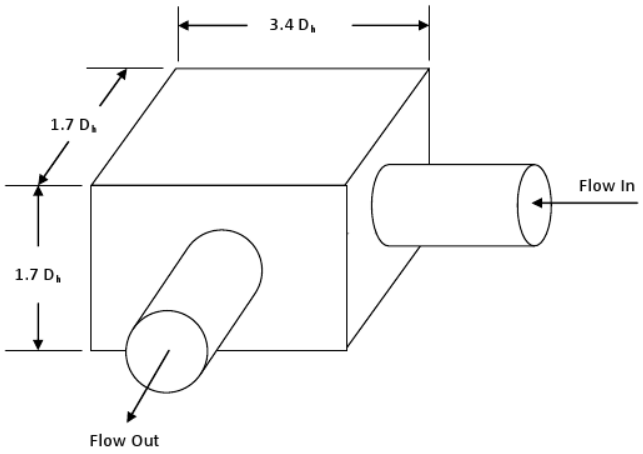

Fig. 3.1. Generic-Tee-Plenum

A single point representative sample of a uniform aerosol concentration and size distribution is desired, the requirements of which are based on the criteria of ANSI/HPS-N13.1-1999. The mixing quality from this standard is quantified by the coefficients of variation (COV) [33], defined by

$$COV = \frac{\sqrt{\frac{1}{1-N}\sum_{i=1}^{N}(x_i - \bar{x})^2}}{\bar{x}} \tag{3.1}$$

where N is the number of points sampled in the cross-sectional area of the duct, x_i is the value of the variable measured at the i^{th} grid location, and $\bar{x}$ is the mean value of the measurements. The grid of measurement points should encompass at least two-thirds of the central cross-sectional area of the duct in accordance with the guidelines set out by the EPA.

According to Han *et al.* [33], the mixing standard states that the COV of velocity should not exceed 20% over the area defined by the EPA grid. The maximum concentration of the tracer gas at any point in the grid should not exceed 30% of the average concentration across the grid. The Reynolds number must also exceed 10^4. The results of the work by Han *et al.* are summarized in Table 3.1.

Table 3.1
Mixing Characteristics at 4 Duct Diameters Downstream of a Mixing Element

	Velocity		**Gas Concentration**		**Particle Concentration**	
Mixing Element	COV	STDEV	COV	STDEV	COV	STDEV
90° elbow	6.7%	0.9%	17.7%	3.1%	27.5%	1.1%
Commercial mixer[a]	10.3%	1.5%	7.6%	1.1%	8.8%	0.8%
Commercial mixer[b]	6.7%	1.4%	4.7%	1.0%	8.0%	0.5%
SH-GTP	5.9%	0.7%	6.4%	0.7%	6.4%	0.9%
SV-GTP	5.3%	0.9%	7.6%	1.0%	6.1%	0.6%
LH-GTP	5.1%	0.6%	5.1%	0.8%	7.4%	0.9%

[a] at elbow inlet

[b] at elbow outlet

Table 3.1 shows that the GTP can be used for single point measurements if they are taken at least 4 duct diameters downstream of the GTP. The GTP used in this experiment has a height of 24 inches, a width of 24 inches, and a length of 48 inches.

Aerosol samples are taken using a fluidized bed aerosol capture system, referred to as impingers by Tomb [11] in Section 2.2.1. The system, see Figure 3.2, consists of a sampling probe that is placed in the aerosol laden air flow, which should be a representative sample of a uniform concentration and size distribution, as previously discussed. The flow from the probe goes to a filter holder that is sealed by use of an O-ring. The flow through the collector is generated by a pump and measured with a

rotameter and a pressure gauge [34]. The upstream aerosol sampler is located 1 ft prior to the spray region.

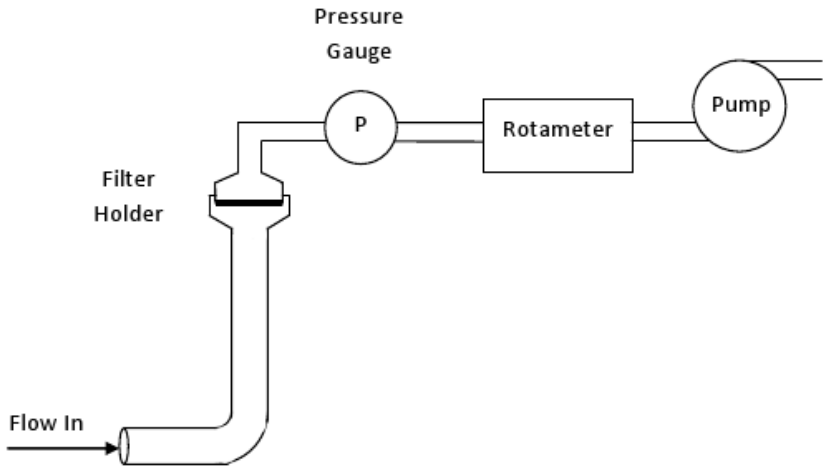

Fig. 3.2. Experiment Aerosol Capture System

3.1.2 Spray and Downstream Region

The spray region is an expansive region in which the aerosol scavenging occurs. The region is a 7 ft long, 2 ft wide, 6 ft high enclosed region that contains five evenly spaced spray nozzles. The nozzles are located beneath the induced air inlet and are directed upward and 45° into the air flow and are spaced 1 ft apart, see Figure 3.3.

There are five Spray Systems Co. Fulljet 1/4GG-1 model nozzles in the spray region. Each nozzle has a capacity of 0.21 gpm and a spray half angle of 28° at a water pressure of 50 psi [35]. The volume mean diameter (VMD) is roughly 850 microns, although no geometric standard deviation (GSD) is listed [35]. The VMD, also known as the mass mean diameter (MMD), is the diameter for which half of

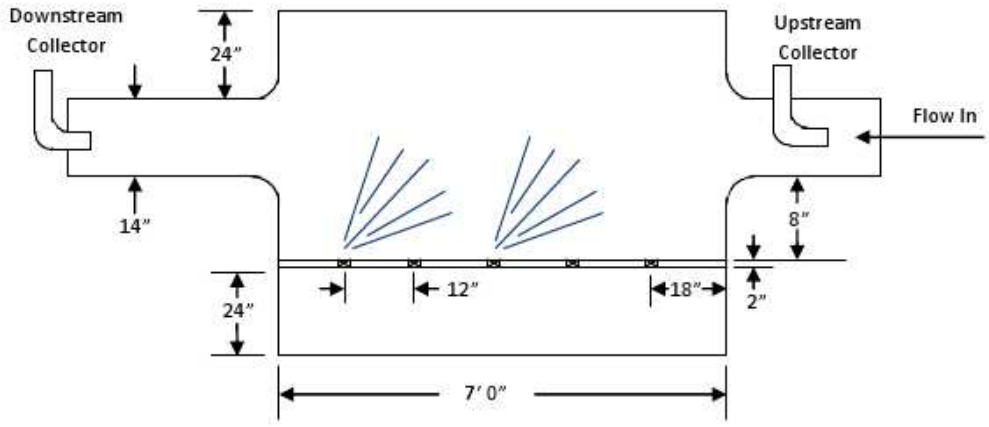

Fig. 3.3. Experimental Setup

the volume or mass contributes to particles larger and smaller than the VMD [1]. As mentioned previously, the sprays are directed in the positive z-direction and are adjustable in θ $(0 < \theta < 2\pi)$ and ϕ $(0 < \phi < \pi)$.

The downstream region contains another aerosol sampling probe identical to the one described in Section 3.1.1. The aerosol sampler is located at the end of the exit duct work, measured to be 5 feet downstream of the spray region.

3.1.3 Other Equipment and Materials

The particulate matter used as an aerosol is fine Arizona test dust. Fine Arizona test dust, which is an International Standards Organization (ISO) approved dust, is an insoluble dust that has an approximate density of 2650 kg/m^3. The composition of the dust is listed in Table 3.2 and the particle cumulative volume distribution shown in Table 3.3 [36].

Fibrous paper filters are used in the aerosol collectors. The filters have a mat weave with fibers ranging from 0.1 to 100 μm in diameter. The filters have a porosity of 60% to 99% with a thickness of 0.15 to 0.5 mm. Particle collection is found

Table 3.2
Arizona Test Dust Composition

Chemical	**Mass Fraction**[%]
SiO_2	68 to 76
Al_2O_3	10 to 15
Fe_2O_3	2 to 5
Na_2O	2 to 4
CaO	2 to 5
MgO	1 to 2
TiO_2	0.5 to 1
K_2O	2 to 5

throughout the depth of the filter. High collection efficiencies require low air velocities and pressure drops are found to be relatively low. Fibrous paper filters are susceptible to moisture and have a relatively low filtration efficiency for sub-micron particles [34].

3.2 Procedure

A number of variables were changed between experimental runs including: the air flow rate, water flow rate, and nozzle geometry. The aerosol concentration also changed, but only as a by-product of changing the air flow rate. Three air flow rates were tested during the course of experimentation, which were 105 ft/min, 635 ft/min, and 1250 ft/min. The water flow rate was changed by changing the number of active nozzles. Two water flow rates were used, 0.84 gpm and 0.42 gpm, in addition too test cases run with zero nozzles activated. The nozzle geometry was changed by simply activating and deactivating specific nozzles, keeping the spray angle constant

Table 3.3
Arizona Test Dust Size Distribution

Size[μm]	**Maximum Volume Fraction**[%]
1	2.5 to 3.5
2	10.5 to 12.5
3	18.5 to 22
4	25.5 to 29.5
5	31 to 36
7	41 to 46
10	50 to 54
20	70 to 74
40	88 to 91
80	99.5 to 100
120	100

for each geometry. There were three geometries used, which are shown in Figure 3.4. The duration of the experimental runs were timed and recorded.

Prior to any experimentation, the filters used in the aerosol samplers were weighed and the blower was set to the desired flow rate and allowed to come to steady state. Filters were weighed with a Mettler Toledo scale, model AB104-S. The test dust was mixed prior to use because of possible stratification that may have taken place while in the storage container.

Since a single point aerosol sampling setup is used, care had to be taken to ensure isokinetic sampling was taking place. The isokinetic sampling procedure is used to ensure a representative aerosol sample enters the sampling probe. This occurs when the sampling probe is aligned to be parallel with the incoming gas streamlines and the gas that enters the probe is also at the free stream velocity [1].

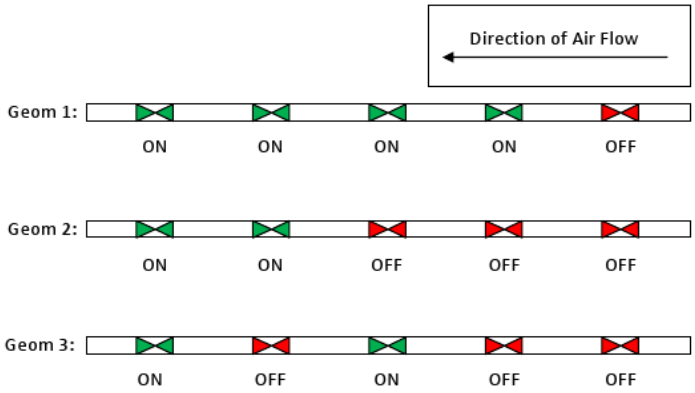

Fig. 3.4. Experiment Nozzle Geometries

When the probe is mis-aligned, the error in the concentration measured is based on the Stokes number, Stk, and the angle of mis-alignment, Θ. When $Stk > 6$, the maximum error in concentration is described by $\frac{C}{C_o} = \cos\Theta$, where C is the concentration in the probe and C_o is the concentration in the free stream. For the smaller Stk ($0.01 < Stk < 6$), the concentration ratio is defined as Equation 3.2 [1]. Figure 3.5 illustrates how significant the error can be if the probes are mis-aligned.

$$\frac{C}{C_o} = 1 + (\cos\Theta - 1)\left[1 - \frac{1}{1 + 0.55(Stk \cdot e^{(0.022\Theta)})e^{0.25 \cdot (Stk \cdot e^{(0.022\Theta)})}}\right] \tag{3.2}$$

After filters were loaded in the aerosol sampling probes, the integrity of the filter holder seal had to be checked. The seal is checked by first recording the pressure when the assembly is known to be capped-off properly and then simply monitoring the pressure afterwards to ensure the proper seal is sustained [34]. The filters were immediately weighed and then weighed again after a few days to allow them to reach equilibrium with the environment.

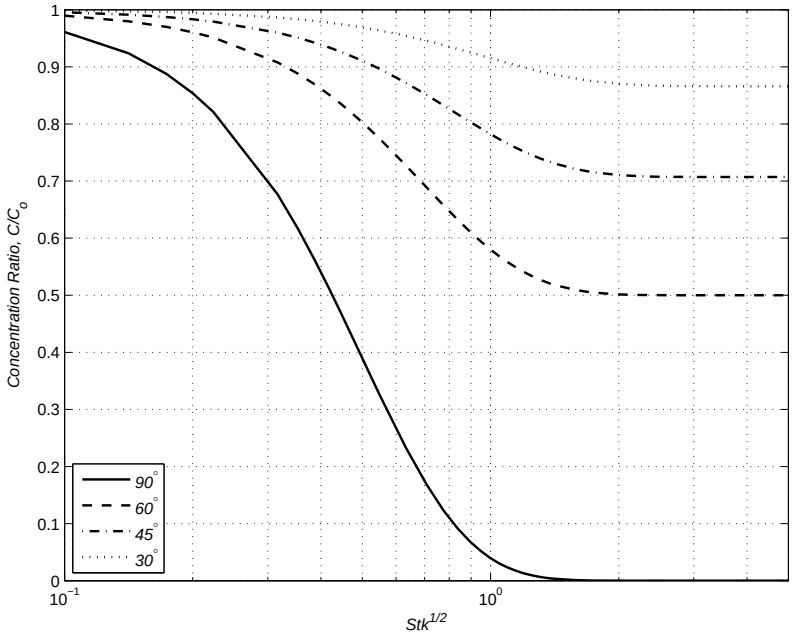

Fig. 3.5. Effect of Sampling Probe Mis-Alignment

3.3 Data Post-Processing

Post-processing was required to obtain results from the experiment raw data. As a first step, measurement uncertainties had to be determined to carry out the uncertainty analyses. Filter weights then had to be corrected for the pump flow rates and aerosol number densities had to be calculated from the system air flow rates, filter weights, and test durations. Also, overall collection efficiencies could be calculated.

The measurements for pump flow rate, pump pressure, and time were all taken using reliable analog instruments. Reasonable estimates of the measurement uncertainties can be made by the researcher using the instrument scale and the length between markings [37]. The instrument used to measure the pump flow rate had increments of 5 *SCFH*, so readings were estimated to be within $\pm$ 1 *SCFH*. The

pressure gauge had increments of 2 *inches wc*, leading to an error of ± 0.5 *inches wc*. An analog watch was used to measure the run durations giving an error of ± 1 *sec*.

Multiple measurements of the system air flow rate and filter weights were done on the same quantity to determine the statistical uncertainty in those measurements. The standard deviation of the mean (SDOM), $\sigma_{\bar{x}}$, was calculated in this case to estimate the uncertainty. The maximum SDOM value was chosen to be conservative. The SDOM was calculated to be ± 8.96 ft/min for the air flow and ± 0.0001 grams for the filter weights. The SDOM is given by [37]

$$\sigma_{\bar{x}} = \frac{\sigma_x}{\sqrt{N}} \tag{3.3}$$

where σ_x is the standard deviation or average uncertainty of the individual measurements, and N is the number of measurements. The standard deviation is calculated by [37]

$$\sigma_x = \sqrt{\frac{1}{N-1}\sum_{i=1}^{N}(x_i - \bar{x})^2} \tag{3.4}$$

The pump flow rates varied slightly between experimental runs. As a consequence, the filter weights had to be corrected. The correction was carried out by non-dimensionalizing the collected pump flow rate data and then multiplying the mass of particulate matter collected by the non-dimensionalized numbers. Standard error propagation equations, given by Taylor [37], were used to calculate the uncertainty.

When summations or differences are taken with data, the uncertainty is calculated by taking the quadratic sum of all measured uncertainties, as in Equation 3.5. The fractional uncertainty for products and quotients can be calculated by taking the sum in quadrature of the original fractional uncertainties, as in Equation 3.6. When raising a measurement to a power, the uncertainty is just the fractional uncertainty times the absolute value of the power. Finally, if the measurement is multiplied by

an exact number, the uncertainty is just multiplied by the absolute value of the exact number.

$$\delta x = \sqrt{(\delta x_1)^2 + (\delta x_2)^2 + \cdots + (\delta x_i)^2} \tag{3.5}$$

$$\frac{\delta x}{|x|} = \sqrt{\left(\frac{\delta x_1}{x_1}\right)^2 + \left(\frac{\delta x_2}{x_2}\right)^2 + \cdots + \left(\frac{\delta x_i}{x_i}\right)^2} \tag{3.6}$$

The initial aerosol number densities were calculated since they could not be directly measured using the equipment available for the experiment. The number density per particle size, given by Equation 3.7 was calculated using the mass collected on the upstream filter, the air flow rate, test duration, particle cumulative volume fraction, and the mass per particle size.

$$N_{D,i} = \frac{\phi_i m_{us}}{\dot{Q}_g m_{p,i} \Delta t} \tag{3.7}$$

In Equation 3.7, $N_{D,i}$ is the number density of the i^{th} particle size given by the particle size distribution, ϕ_i is the volume fraction of the i^{th} size, m_{us} is the total mass of aerosol particles on the upstream filter, Δt is the run duration, $\dot{Q}_g$ is the air flow rate, and $m_{p,i}$ is the particle mass for the i^{th} size. The total number density is calculated by a simple summation of the particle size number densities, $\sum_{i=1}^{N} N_{D,i}$. The uncertainties were calculated using the same propagation equations given by Taylor [37].

The data collected allowed the overall collection efficiency to be calculated, but not the collection efficiency for each particle size. This is because only the total aerosol particle mass was measured on the upstream and downstream filters, with the particle size distribution leaving the spray region having been changed due to the capture process. As a result, the overall collection efficiency calculation was defined simply by

$$\eta = \frac{m_{us} - m_{ds}}{m_{us}} \tag{3.8}$$

where m_{ds} is the total aerosol mass on the downstream filter. Again, error propagation calculations were performed for these calculations.

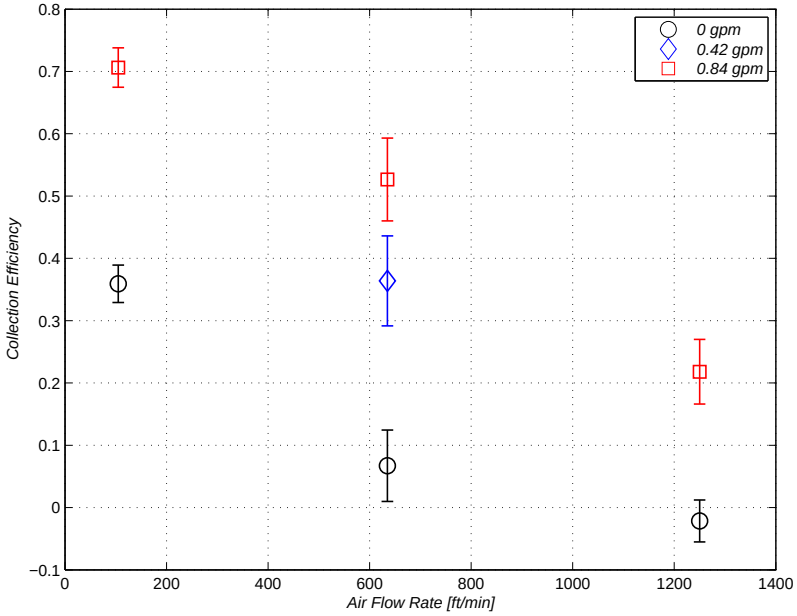

Fig. 3.6. Average Overall Collection Efficiency versus Air Flow Rate

3.4 Results and Analysis

The average overall collection efficiency for the experiment are presented in Figures 3.6 and 3.7, organized for air flow rate and water flow rate, respectively. The general trend of the figures show an expected result of increased collection efficiency with increased water flow rate and decreased air flow rate. The increased collection efficiency for larger water flow rates is expected because of the increased probability of interaction due to the increased number of drops. The higher collection efficiencies for the decreased air flow rates is anticipated because the particle residency time within the spray region rises, again leading to a larger probability of interaction. In essence, if looked at from the particles point of view, an increased number of drops are perceived because they are in the spray region for a longer duration.

The overall collection efficiency was also plotted against the non-dimensionalized aerosol number density, and again sorted by air flow rate and water flow rate. Figure 3.8 presents the results sorted by the air flow rate. The collection efficiencies

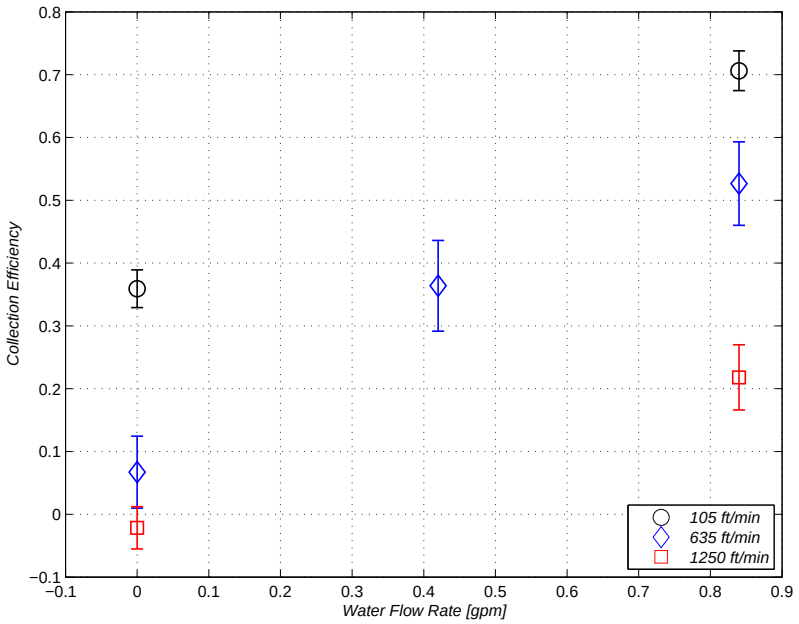

Fig. 3.7. Average Overall Collection Efficiency versus Water Flow Rate

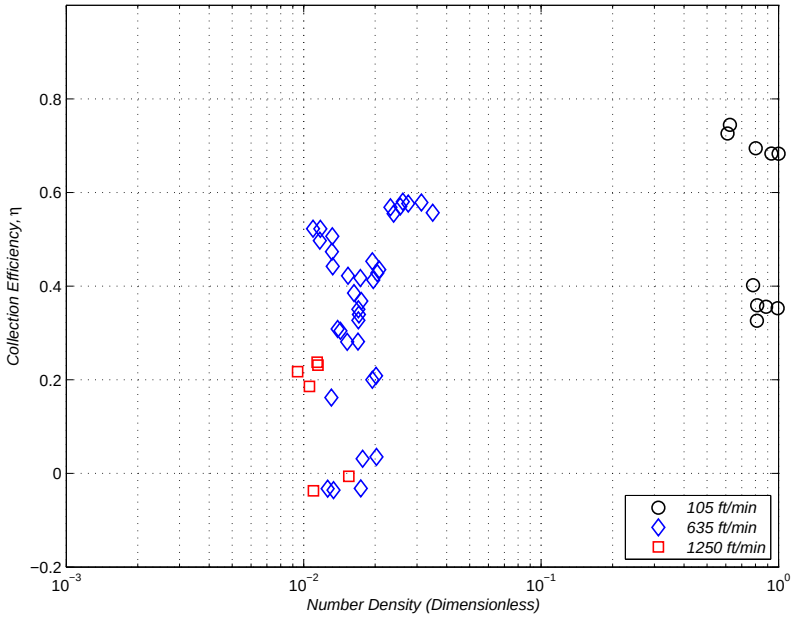

Fig. 3.8. Overall Collection Efficiency versus Non-Dimensionalized Number Density Sorted for Air Flow Rate

seem to be clustered according to the air flow rate, with the higher collection efficiencies located at the larger number densities. Figure 3.9 presents the same results as Figure 3.8, but highlight the data points by the water flow rate. Figure 3.9 exhibits an increased collection efficiency with increased aerosol number density as a function of the water flow rate. The uncertainties for the data in the overall collection efficiency against the non-dimensionalized number density figures were removed because the data is closely packed. As a consequence, some of the data appears to show a negative collection efficiency. This explains some of the negative efficiencies but not all of them. Some of the negative collection efficiencies may be a result of dust resupsension that may have been collecting in the spray region during other experimental runs. The uncertainty for these figures are listed Appendix B.

The effect of the nozzle geometry as described in Section 3.2 is not noticeable, except for the reduced water flow rate caused from going from four nozzles down to two. Geometries 2 and 3, shown in Figure 3.4, do not provide any discernible differ-

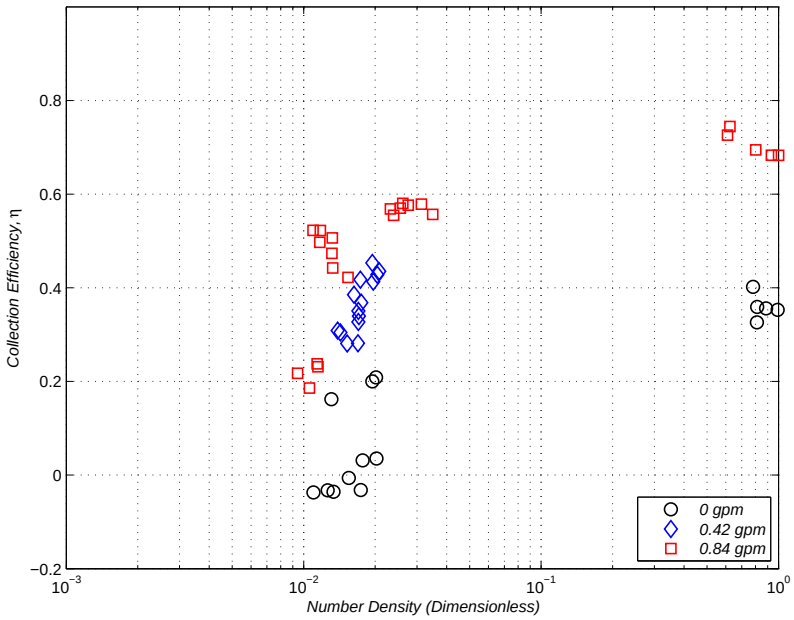

Fig. 3.9. Overall Collection Efficiency versus Non-Dimensionalized Number Density Sorted for Water Flow Rate

Table 3.4
Calculated Average Overall Collection Efficiency

Water Flow Rate, $[gpm]$	**Air Flow Rate,** $[ft/min]$	**Collection Efficiency,** 1^{st} ***weighing***	**Collection Efficiency,** 2^{nd} ***weighing***
0.00	105	0.359 ± 0.03	0.358 ± 0.03
0.00	635	0.067 ± 0.06	0.064 ± 0.06
0.00	1250	-0.022 ± 0.03	-0.043 ± 0.03
0.42	635	0.364 ± 0.07	0.364 ± 0.07
0.84	105	0.706 ± 0.03	0.705 ± 0.03
0.84	635	0.527 ± 0.07	0.539 ± 0.07
0.84	1250	0.218 ± 0.05	0.214 ± 0.05

ence in collection efficiency. Even though there was no visible affect of changing the geometry, a conclusion can not be made because only a limited number of geometries were tested in the performed experiment.

As mentioned previously, in Section 3.3, the filters were weighed twice, once right after experimentation and then again a few days later to allow them to reach equilibrium with the environmental conditions. The differenced in these weighings were almost imperceptible. A comparison of the results for the average overall collection efficiency is demonstrated in Table 3.4.

A direct comparison to the reviewed literature is difficult to make because the experimental setups were different. The reviewed literature measured collection efficiency of a mono-disperse aerosol size distribution compared to the poly-disperse distribution used in this research. Spray angles and the spray geometries are also different than in the reviewed literature. For example, Tomb *et al.* [11] measured the collection efficiency of a mono-disperse aerosol in a horizontal duct with sprays

angled to be parallel and counter current to the air flow. This research measured the collection efficiency of a poly-disperse aerosol in an expansive region with sprays angled at 45° into the air flow. This leads to differences in flow fields created by the sprays and incoming air, not to mention the difficulty in measuring the collection efficiency of discrete size aerosol particles.

4. ANALYTICAL MODELS

As a supplement to the experimental work, a numerical analysis of collection efficiency by sprays was carried out. The first model used was derived by Cheng [10] and will be referred to as the deterministic model. The second model was derived based on the same concepts as the deterministic model, but employed a Monte Carlo technique to the aerosol particle location relative to the drop. The previously surveyed literature only gives collection efficiency of single spherical body collectors for ideal collection cases, therefore an analysis of a non-ideal case had to be carried out to estimate the capture of non-wettable particles.

There are multiple assumptions taken for the theoretical analyses performed, the most notable of which is that inertial impaction is the only scavenging mechanism examined. This assumption is valid because the other collection mechanisms are insignificant, see Figure 4.1, in comparison with the particle sizes used in the experiment, with the exception of the electrostatic deposition. Electrostatic deposition is ignored because the charge on the aerosol particles and drops are not measured and can not be estimated.

Particles are considered lost after collision with no re-suspension. In the physical system, the particulate matter is hydrophobic and can possibly pass through the drop if the relative velocities are large enough. Particles may also be re-suspended when the drop hits a wall or has a collision with another drop. These phenomena amount to a small contribution to the total overall surviving aerosol cloud and will therefore be ignored.

The system of a particle cloud interacting with a drop cloud is extremely complex. With the large number of particles and drops available in the system it is a certainty that drops will collide with other drops and particles will interact with other particles. It will be assumed that this can not happen. The assumption will be made because of the added complexity that two evolving size distributions can create.

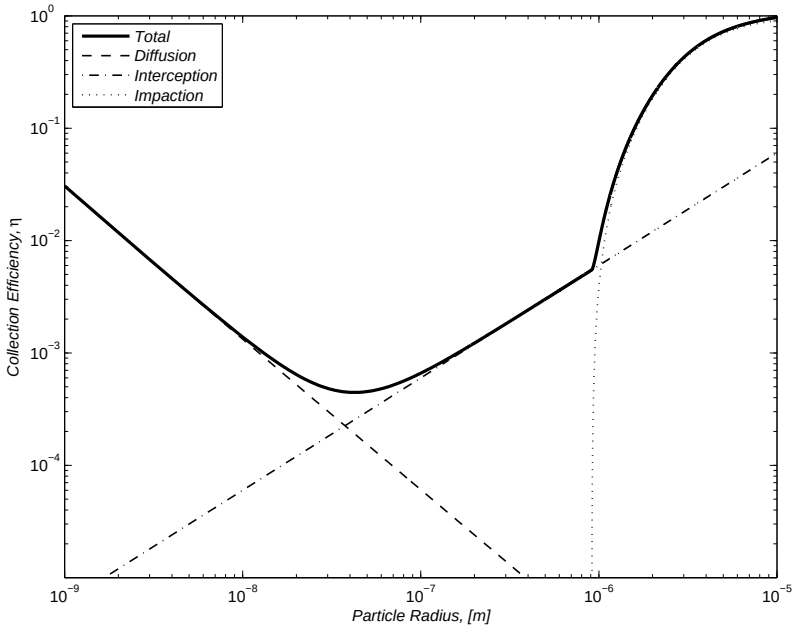

Fig. 4.1. Theoretical Collection Efficiencies

Particles and drops are assumed to be rigid spheres. More than likely, the dust particles used are not spheres, but are of an arbitrary shape. This would change the aerodynamic diameter and ultimately alter the track the particle might follow. Drops larger than about 500 microns also start to alter the spherical shape of the drop [38]. This is going to change the gas streamlines around the drop and probably alter the collection efficiency.

Heat and mass transfer are not considered. The temperature gradient in the system is small, so evaporation and condensation are most probably insignificant. The additional modeling of evaporation and condensation has a diminishing return because of the small temperature gradient.

Both the deterministic and Monte Carlo models consider a uniform drop spacing throughout the spray region and the drops are a single size. As mentioned before, the physical system is extremely complex, and the drops are not going to be uniformly

spaced. The drop number density will be higher near the nozzle exit. The assumption of uniform drop spacing is a simplifying assumption.

Inviscid, incompressible, and irrotational flow is assumed when solving for the flow around a sphere. Potential flow is a valid assumption because in the current analysis only the front side of the drop is being considered as the collection surface, and in general flow separation will not occur before the grazing trajectory is reached. There is some interest in the additional collection due to wake capture, but that will not be studied here.

4.1 Deterministic Model

The deterministic model employed for the theoretical analyses performed was derived by Cheng [10]. The equations were developed to estimate the collection efficiency of airborne particles by sprays using the concept of evenly distributed sprays and particles. It was assumed that the particles were uncharged and larger than 0.5 μm. Consequently, inertial impaction was the only collection mechanism considered. The equations only deal with mono-disperse particle and drop size distributions.

The model developed by Cheng assumes uniform spacing between drops and particles. Using this spacing relationship is a logical choice for a rudimentary model because it allows averaging of some of the variables and it is easy to visualize the interactions in the system. The mean inter-drop length, s, is given by

$$s = d_c \left(\frac{A \cdot l}{6 V_l} \right)^{\frac{1}{3}} \tag{4.1}$$

where A is the cross-sectional area of the spray region, l is the length of the spray region, and V_l is the total volume of liquid to be atomized. The mean inter-drop length can then be used to determine the number of drop layers in the region, Equation 4.2, and ultimately the number of drops per layer, Equation 4.3.

$$n_d = \frac{l}{s} = \left[\frac{6 V_l}{\pi A d_c^3} \right]^{\frac{1}{3}} l^{\frac{2}{3}} \tag{4.2}$$

$$\frac{A}{s^2} = \frac{6V_l}{\pi d_c^3}\frac{1}{n_d} \tag{4.3}$$

The mean inter-particle area, a, perpendicular to particle flow can be calculated using Equation 4.4. In Equation 4.4, V_g is the total volume of the spray region and p_o is the initial number of particles that collide with the first drop layer.

$$a = \frac{V_g}{p_o \cdot l} \tag{4.4}$$

At this point the collection efficiency of a discrete drop, as derived by Langmuir and Blodgett [23] and experimentally determined by Walton and Woolcock [17], is used to determine the number of particles captured by the drops. The number of particles captured by the first layer of drops, p_1, is

$$p_1 = p_o \eta \frac{3lV_l}{2d_c V_g n_d} \tag{4.5}$$

Using Equations 4.4 and 4.5 and the number of drop layers, the total number of particles captured by the spray can be determined. This calculation can be done on a per layer basis, or the total collection efficiency can be calculated by

$$\eta_{tot} = 1 - \left[1 - \eta \frac{3l\dot{Q}_l}{2d_c \dot{Q}_g n_d}\right]^{n_d} \tag{4.6}$$

where $\dot{Q}_l$ and $\dot{Q}_g$ are the water flow rate and air flow rate, respectively.

The outlined equations will calculate the collection efficiency of a single particle size for a discrete drop size. To calculate the collection efficiency for the particle size distribution reported in Section 3.1.3 the above equations had to be repeated for each particle size. Then the total collection efficiency could be determined by a summation of discrete particle size collection efficiencies. A parametric study on the affect of drop size could then be performed.

4.2 Monte Carlo Model

The Monte Carlo model borrows some of the features of the deterministic model, specifically the idea of a mean inter-drop length and number of particles on a unit

area basis. Although the number of particles per unit area are calculated in the same manner, the way the value is utilized is different. Instead of taking the particles as being evenly spaced, their location relative to the drop is randomly sampled.

The random number generator (RNG) used is the default RNG provided by MATLAB. RNGs are not truly random and cannot be truly random because they are generated by a computer. They are pseudo-random sequences of numbers that appear to be randomly sampled from a uniform distribution on the interval (0,1). RNGs typically must pass a series of tests to ensure they are undoubtedly generating a pseudo-random sequence of numbers. It will be assumed that the MATLAB default RNG is sufficiently generating a pseudo-random sequence of numbers without running these tests. The seed number will be chosen to be based on the computers internal clock to help ensure an identical sequence of pseudo-random numbers is never used.

An example of a robust RNG is given by the Monte Carlo Neutral-Particle (MCNP) code development team [39]. They use the linear congruential scheme described by

$$S_{i+1} = S_i G + K \mod 2^M \tag{4.7}$$

and

$$R_i = 2^{-M} S_i \tag{4.8}$$

where S is the seed number, G is a multiplier, K is an additive constant, M is an M-bit integer, and R is the random number generated. The period of the algorithm described is $2^M \approx 7.04$ x 10^{13} when $M = 46$.

An adjustment to the number of drops in each layer had to be made since the way the value was calculated for the deterministic model gave a fractional value. In the Monte Carlo method this value was rounded to the nearest integer. Similarly, the correction had to be made for the number of particles in each layer.

Since the drops are uniformly distributed in the region, as in the deterministic model, the description of the aerosol particle collection process is described on a per

drop basis. Each drop is contained in a rectangular area, A, which is a fraction of the total cross-sectional area of the spray region. We know from experimental and theoretical analyses that the probability of particle-drop interaction is given by η, which can be used to determine the radius of particle collection in A by using the ratio $\eta = \beta^2/d_c^2$, where β is the limiting radius of particle collection. We can use β and the equivalent radius for a circle with the same area as A to calculate the probability of particle collision.

If we randomly sample the particle location and size, corresponding to the particle cumulative size distribution, then we can determine if the particle survives. If the particle survives it is counted and the size information is retained. The size information must be kept because that information will then determine the particle cumulative size distribution for the next layer of drops.

The calculations are repeated for the number of drops in each layer. Following each layer calculation, the particle size distribution is recalculated to correctly represent the particles that survive. All calculations are then repeated for each drop layer in the spray region until the total collection efficiency for each particle size is determined. The total overall collection efficiency is a simple summation of the discrete particle size efficiencies.

The Monte Carlo method also requires the calculation of a SDOM. The SDOM is defined by

$$SDOM = \sqrt{\left(\frac{1}{N-1}\right)\left[\left(\frac{tally}{N}\right) - \left(\frac{tally}{N}\right)^2\right]} \tag{4.9}$$

where *tally* is the tally of surviving particles.

4.3 Non-Ideal Particle Collection

An issue with the calculations arises when the type of aerosol particulate matter used in the experiment is considered. The Arizona test dust composition presented in Section 3.1.3 suggests that the material is hydrophobic. Examining the theoretically

and experimentally determined collection efficiencies for discrete drops it should be recalled that they were derived for an ideal collection situation. In other words, the particulate matter is hydrophilic and any collision with the drop results in removal. This deficiency will be addressed in this section.

4.3.1 Potential Flow Around a Sphere

Previously, in Section 2.1.2, it was noted that earlier researchers used what was described as the classical solution for potential flow around a sphere. They proceeded to present the equations as [27]

$$u_{g,x} = 1 - \frac{2x^2 - y^2}{2(x^2 + y^2)^{2.5}} \tag{4.10}$$

and

$$u_{g,y} = \frac{-3xy}{2(x^2 + y^2)^{2.5}} \tag{4.11}$$

with no explanation as to how the equations were derived. The insufficient description prompted a search for another method of solving for the potential flow around a sphere. Batchelor [40] and Currie [41] provide the method of solution. The following derivation is taken from Currie [41].

If we take the fluid flow to be inviscid, incompressible, and irrotational, then a velocity potential exists, given by Laplace's equation. Since the flow is taken to be around a sphere it is advantageous to expand Laplace's equation is spherical coordinates using the fact that $\partial/\partial\omega = 0$ for an axisymmetric flow. Laplace's equation is then given by

$$\frac{1}{r^2}\frac{\partial}{\partial r}\left(r^2\frac{\partial\phi}{\partial r}\right) + \frac{1}{r^2\sin\theta}\frac{\partial}{\partial\theta}\left(\sin\theta\frac{\partial\phi}{\partial\theta}\right) = 0 \tag{4.12}$$

In the spherical coordinate system the velocity components related to the velocity potential are

$$u_r = \frac{\partial\phi}{\partial r} \tag{4.13}$$

and

$$u_\theta = \frac{1}{r}\frac{\partial \phi}{\partial \theta} \tag{4.14}$$

The stream function is a function that satisfies the two-dimensional continuity equation. Although we are dealing with a three-dimensional object, the stream function can still be used since we are assuming an axisymmetric flow. If we substitute Equations 4.13 and 4.14 into Equation 4.12 and relate the velocity components to the stream function, ψ, by

$$u_r = \frac{1}{r^2 \sin\theta}\frac{\partial \psi}{\partial \theta} \tag{4.15}$$

and

$$u_\theta = -\frac{1}{r \sin\theta}\frac{\partial \psi}{\partial r} \tag{4.16}$$

then all the continuity equation can be satisfied for all stream functions, ψ. The stream function is useful for interpreting flow fields because for $\psi = Constant$, the slope of the stream function is the same as the slope of the streamlines [42]. The velocity potential, ϕ, and stream function, ψ, are also found to be orthogonal.

Now that we have a relationship between ϕ and ψ, we can solve Laplace's equation for the velocity potential and, by way of the relationship, obtain corresponding stream function. The velocity potential can be solved by separation of variables. If the velocity potential is defined by

$$\phi(r, \theta) = R(r)T(\theta) \tag{4.17}$$

and then substituted into Equation 4.12, we have

$$\frac{T}{r^2}\frac{d}{dr}\left(r^2\frac{dR}{dr}\right) + \frac{R}{r^2 \sin\theta}\frac{d}{d\theta}\left(\sin\theta\frac{dT}{d\theta}\right) = 0 \tag{4.18}$$

which can be reduced and separated by multiplying by $r^2/(RT)$. The separated equation is given by

$$\frac{1}{R}\frac{d}{dr}\left(r^2\frac{dR}{dr}\right) = -\frac{1}{T \sin\theta}\frac{d}{d\theta}\left(\sin\theta\frac{dT}{d\theta}\right) \tag{4.19}$$

The equations can now be separated and set equal to some function, λ. In this case $\lambda = b(b+1)$ because this selection results in the ordinary differential equation for $T(\theta)$ to appear in standard form. If the separated equations were simply set to λ, then the equation for $T(\theta)$ would require another transformation to be solved.

The general solution for $R(r)$ is given by Equation 4.20. This solution is obtained by searching for the solution in the form of $R(r) = Kr^{\alpha}$, which when substituted back into the differential equation for $R(r)$ is satisfied by $\alpha = b$ and $\alpha = -(b+1)$.

$$R_b(r) = K_{1,b}r^b + \frac{K_2, b}{r^{b+1}} \tag{4.20}$$

where K_1 and K_2 are arbitrary constants.

The equation for $T(\theta)$ is found to be Legendre's equation, which can be reduced to its standard form by the transformation $x = \cos\theta$. The general solution to the equation for $T(\theta)$ is a combination of Legendre's function of the first and second kind, given by

$$T_b(\theta) = K_{3,b}P_b(\cos\theta) + K_{4,b}Q_b(\cos\theta) \tag{4.21}$$

where K_3 and K_4 are constants, P_b is Legendre's function of the first kind, and Q_b is Legendre's function of the second kind. Legendre's function of the second kind diverges for $\cos\theta = \pm 1$ for all values of b, meaning K_4 must be zero, since no singularities are allowed in the flow field.

Combining the solutions of Equation 4.20 and 4.21, we find that the solution for the velocity potential for all integers b is

$$\phi(r,\theta) = \sum_{b=0}^{\infty} \left(K_{1,b}r^b + \frac{K_{2,b}}{r^{b+1}} \right) P_b(\cos\theta) \tag{4.22}$$

where,

$$P_b(x) = \frac{1}{2^b b!}\frac{d^b}{dx^b}(x^2-1)^b \tag{4.23}$$

The solution for Equation 4.22 for uniform flow can be solved by setting $K_1 = 0$ for $b \neq 1$, $K_1 = u$ for $b = 1$, and $K_2 = 0$ for all b. Legendre's function of the first kind for $b = 1$ of $\cos\theta$ is just $\cos\theta$, so Equation 4.22 reduces to

$$\phi(r,\theta) = ur\cos\theta \tag{4.24}$$

Since we now have an equation for the velocity potential, we can apply the definitions of Equation 4.13 and 4.15 to obtain the solution of the stream function.

$$\psi = \frac{1}{2} u r^2 \sin^2\theta + f(r) \tag{4.25}$$

where $f(r)$ is any function of r. The same solution can be obtained by solving Equations 4.14 and 4.16 for ψ, except the additional function is going to be a function of θ. Since the solution is the same, the functions of r and θ should be equal. If we take these functions to be zero, then the general solution for the steam function in a uniform flow field is given by

$$\psi = \frac{1}{2} u r^2 \sin^2\theta \tag{4.26}$$

The solution of the velocity potential for a source or sink is required to solve for flow due to a doublet. The solution for the velocity potential for a source or sink can be solved by letting $K_1 = 0$ for all b, $K_2 = 0$ for $b \neq 0$, and $K_2 \neq 0$ for $b = 0$, and knowing that the Legendre function of the first kind for $b = 0$ of $\cos\theta$ equals unity. The resulting velocity components result in a purely radial velocity.

$$u_r = -\frac{K_{2,0}}{r^2} \tag{4.27}$$

and

$$u_\theta = 0 \tag{4.28}$$

It may be noticed from Equation 4.27 that the magnitude of the velocity increases as it approaches the origin, and at the origin there is a singularity. The volume of fluid entering or leaving the singularity can be assessed by enclosing it in a spherical control surface. If we let q be the volume of liquid, then $q = \int_s u \cdot n ds$, but since the velocity is radial $u \cdot n$ becomes $|u|$ and $ds = r^2 \sin\theta d\theta d\omega$. So the equation for q becomes,

$$q = \int_0^{2\pi} d\omega \int_0^{\pi} \left(\frac{K_{2,0}}{r^2} \right) r^2 \sin\theta d\theta = -4\pi K_{2,0} \tag{4.29}$$

Solving Equation 4.29 for $K_{2,0}$ we can obtain the equation for the velocity potential for a source or sink.

$$\phi(r,\theta) = -\frac{q}{4\pi r} \tag{4.30}$$

Flow due to a doublet can be solved by superimposing the potential velocity equations for a source and sink of equal strength, when the source and sink are a small distance, δx, apart and letting that distance go to zero. The equation for the velocity potential then becomes

$$\phi(r,\theta) = -\frac{q}{4\pi r} + \frac{q}{4\pi(r-\delta r)} \tag{4.31}$$

Since the source and sink are only located a small distance apart, the equation for the velocity potential can be expanded and simplified to be

$$\phi(r,\theta) = \frac{q}{4\pi r}\left[\frac{\delta r}{r} + O\left(\frac{\delta r}{r}\right)^2\right] \tag{4.32}$$

The triangle formed by the distance δx and the two vectors r and $r-\delta r$ can be used to solve for the value δr by using the cosine rule (i.e. $(r-\delta r)^2 = r^2+\delta x^2-2r\delta x\cos\theta$). The the result is

$$\phi(r,\theta) = \frac{q}{4\pi r}\left\{\frac{\delta x}{r}\cos\theta\left[1+O\left(\frac{\delta r}{r}\right)\right]\right\} \tag{4.33}$$

If we let $\delta x \to 0$, $q \to \infty$, and $q\delta x \to \mu$, then the solution of the velocity potential due to a doublet is

$$\phi(r,\theta) = \frac{\mu}{4\pi r^2}\cos\theta \tag{4.34}$$

Solving the velocity potential equation for the stream function we get

$$\psi(r,\theta) = -\frac{\mu}{4\pi r}\sin^2\theta \tag{4.35}$$

The solution for the stream function for flow around a sphere can be obtained by superimposing the solutions of the stream function for uniform flow and that due to a doublet, as given by Equation 4.36.

$$\psi(r,\theta) = \frac{1}{2}ur^2\sin^2\theta - \frac{\mu}{4\pi r}\sin^2\theta \tag{4.36}$$

Knowing that the stream function at $\psi = 0$ is the solution along the surface of the sphere and that the stream function on the surface equals zero, we can solve for the value of μ. This is done by setting r equal to the radius of the sphere, R, and solving

Equation 4.36. Doing this we find that $\mu = 2\pi u R^3$. Substituting that back into Equation 4.36, we have the stream function for flow around a sphere,

$$\psi(r,\theta) = \frac{u}{2}\sin^2\theta\left(r^2 - \frac{R^3}{r}\right) \tag{4.37}$$

In order to plot the stream lines, as shown in Figure 4.2, the stream function equation has to be solved for r or θ. The approach taken was to solve for the radial position of the velocity at any given angle, θ. When Equation 4.37 is solved for r, we have three solutions

$$r_1 = \frac{1}{6}\frac{a}{u\sin\theta} - \frac{4\psi}{a\sin\theta} \tag{4.38}$$

$$r_2 = -\frac{1}{12}\frac{a}{u\sin\theta} + \frac{2\psi}{a\sin\theta} + \frac{\mathrm{I}\sqrt{3}}{2}\left[\frac{1}{6}\frac{a}{u\sin\theta} + \frac{4\psi}{a\sin\theta}\right] \tag{4.39}$$

$$r_3 = -\frac{1}{12}\frac{a}{u\sin\theta} + \frac{2\psi}{a\sin\theta} - \frac{\mathrm{I}\sqrt{3}}{2}\left[\frac{1}{6}\frac{a}{u\sin\theta} + \frac{4\psi}{a\sin\theta}\right] \tag{4.40}$$

where

$$a = \left[u^2\left(108R^3u\sin^3\theta + 12\sqrt{3}\sqrt{\frac{32\psi^3 + 27R^6u^3\sin^6\theta}{u}}\right)\right]^{\frac{1}{3}} \tag{4.41}$$

If we take $180° < \theta < 90°$, Equation 4.38 is used to solve for the potential stream lines around a sphere as shown in Figure 4.2

4.3.2 Particle Trajectory

The particle trajectory is calculated by use of Newton's second law of motion, $\Sigma F = ma$. As in Section 2.1.2, the only force considered to alter the particles trajectory is the drag force. The thermophoretic force is considered to be small because the experiment was performed at environmental temperatures and large temperature gradients are not present. The diffusiophoretic force is ignored, partly for the same reason as the thermophoretic force, because the molecular concentration gradient is considered to be insignificant. The electrostatic force is not considered

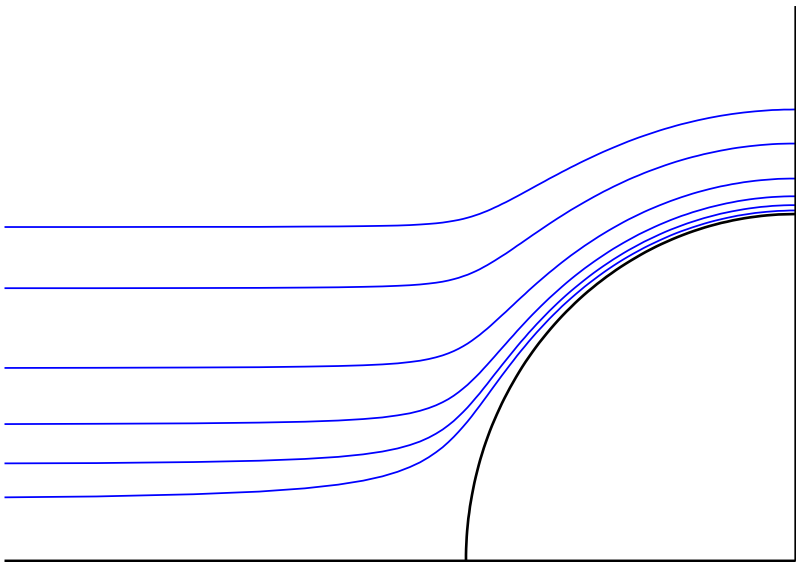

Fig. 4.2. Solution for Potential Flow Around a Sphere

because electrical charges were not measured, although the force may be significant in the aiding the collection of aerosol particles. The gravity force is also not taken into account because of the small contribution due to length scales and particle sizes.

If we consider that the aerosol particle is originally moving with the air streamlines far away from the drop and then expand Newton's second law of motion, we arrive at

$$\frac{dv_p}{dt} = \frac{F_d}{m_p} \tag{4.42}$$

where the drag force, F_d, is described by

$$F_d = \frac{1}{8}\rho_g C_D \pi d_p^2 (u_g - v_p)|u_g - v_p| \tag{4.43}$$

where the term $(u_g - v_p)|u_g - v_p|$ is used to solve for the magnitude and direction of the drag force. The drag coefficient, C_D, is a function of the Reynolds number and given by Equation 2.7. Note that Equation 4.43 will reduce to Stokes Drag for

$Re < 1$. The Reynolds number is defined using the relative gas stream and particle velocities by [43]

$$Re = \frac{d_p|u_g - v_p|}{\mu} \tag{4.44}$$

Since the stream function has been defined for flow around a sphere, the gas velocities at any point can be determined. Solving Equation 4.37 for the any case of ψ and using the definitions given by Equations 4.15 and 4.16, we find that the velocity components are

$$u_r = u\cos\theta\left(1 - \frac{R^3}{r^3}\right) \tag{4.45}$$

and

$$u_\theta = \left[\frac{-ur\sin^2\theta\left(1 - \frac{R^3}{r^3}\right) - \frac{3}{2}\frac{uR^3\sin^2\theta}{r^2}}{r\sin\theta}\right] \tag{4.46}$$

The velocity components given by the stream function are in spherical coordinates, which will be useful for determining particle capture for the non-ideal case. It is useful, however, to convert the velocities into cartesian coordinates to solve for the drag force since it is easier to visualize the drag in x and y coordinates. It is also useful to convert the positions into cartesian coordinates for plotting purposes. The positions are converted using

$$x(t) = r(t)\cos\theta(t) \tag{4.47}$$

and

$$y(t) = r(t)\sin\theta(t) \tag{4.48}$$

Equations 4.47 and 4.48 can be used to find the velocities in cartesian coordinates by

$$\frac{dx}{dt} = u_x = \frac{dr}{dt}\cos\theta(t) - r(t)\sin\theta(t)\frac{d\theta}{dt} \tag{4.49}$$

and

$$\frac{dy}{dt} = u_y = \frac{dr}{dt}\sin\theta(t) - r(t)\cos\theta(t)\frac{d\theta}{dt} \tag{4.50}$$

and we know that $u_r = \frac{dr}{dt}$ and $u_\theta = r\frac{d\theta}{dt}$, so a substitution can be made and Equations 4.49 and 4.50 can be rewritten as a function of the radial and angular velocities.

Euler's Method is used to calculate the trajectory from the ordinary differential equations describing the particle motion, the general form is given by [44]

$$w_{i+1} = w_i + hf(t_i, w_i) \tag{4.51}$$

where w is the value that is being solved for, h is the time step, and f is a function that describes w with time. Euler's Method is a first order numerical method, but was found to be sufficient for solving the trajectory problem.

Any particle collision with a drop results in collection for the ideal case. The condition for collection for the non-ideal case based on the amount of work required to penetrate the surface of the drop. Since the interfacial tension is high between the particle and drop, in the case of non-wettable particles, collection is based on work done against the drop surface tension. When the particle collides normal to the drop, the total work required for the particle to be captured is

$$W = \frac{8}{3}\pi r^2 \gamma \tag{4.52}$$

where γ is the surface tension of the liquid drop. This means that the particle must have an incident kinetic energy at least equal to W to be captured. Since we solved the particle velocity components in spherical coordinates, we can use the radial velocity at the surface of the drop to determine if the particle has the required kinetic energy to penetrate the surface of the drop and be captured. The condition for capture is given by

$$v_{p,r} \geq \left[\frac{16\pi r_p^2 \gamma}{3m_p}\right]^{\frac{1}{2}} \tag{4.53}$$

The collision efficiency is found by tracking particles until a grazing trajectory is found, done by changing the particle starting y position. The limiting y position give a radius that is used in the definition of the collision efficiency. The definition of collection efficiency is simply the ratio of the particle found in the grazing trajectory to the the particles found in the "shadow" of the collection drop. In other words, the collection efficiency is $\frac{\beta^2}{d_c^2}$, where β is the diameter of the circle created by the

grazing trajectories. The definition of the collection efficiency for the non-ideal case is essentially the same, but β is defined by the limiting case in which particle penetrate the surface of the drop.

4.3.3 Non-Ideal Collection Results

The results of the analysis for non-ideal collision efficiency are shown in Figure 4.3. The figure shows that the analysis undertaken using the outlined method fits the experimental data of Walton and Woolcock [17] and the theoretical analyses of Langmuir and Blodgett [23] and Slinn [29] for the ideal collection case. As a matter of fact, it may be argued that the collection efficiency curve generated using the described method fits the experimental data better than previous researchers attempts.

Knowing that the ideal collection efficiency case is representative of the experimental data, it is assumed that the non-ideal case is also representative of non-wettable particle collection. The non-ideal collection curve was expected to show a lower collection efficiency than the ideal case. This expected trend is exhibited except at higher Stokes numbers.

The non-ideal curve can be used to estimate the collection efficiency of the hydrophobic particulate matter used in the experiment from this research. This is done by simply replacing the collection efficiencies for the ideal cases with the non-ideal case in the deterministic and Monte Carlo models described previously.

4.4 Results and Analysis

A direct comparison of the numerical models against the experimental data of Tomb [11] could not be done because there was insufficient data available. Tomb *et al.* did not clearly define the distance that the spray is ejected or the length between the aerosol samplers. This information is needed to make a valid comparison to their

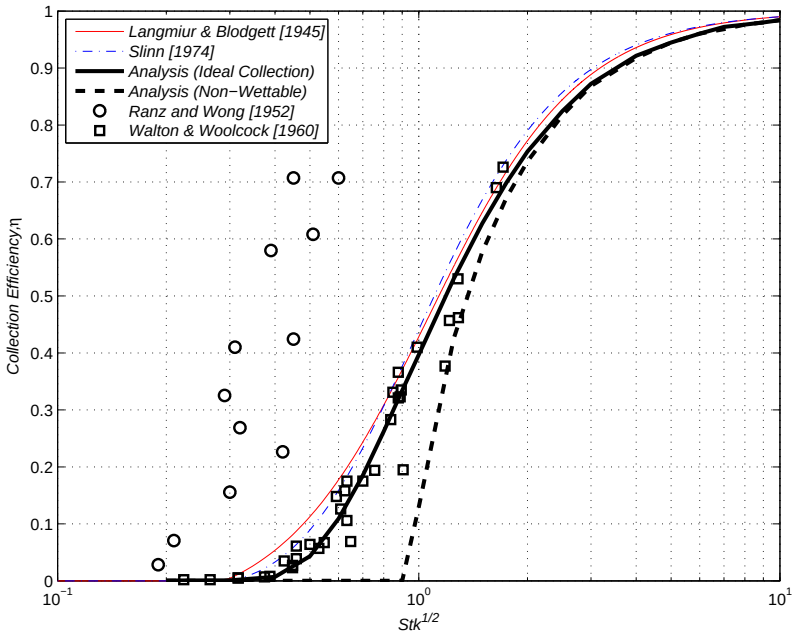

Fig. 4.3. Impaction Collision Efficiency for Ideal and Non-Ideal Cases

experimental data, since length is used to define the number of spray drops in the "collection" region. The drop size distributions was also not reported, making it difficult to make the comparison.

However, if a comparison was made using the theoretical drop travel length, average drop velocity, and a uniform dust size distribution, the results show that the deterministic and Monte Carlo ideal collection cases correlate the best with the experimental data. Figure 4.4 presents the ideal collection case for the deterministic and Monte Carlo models, Figure 4.5 presents the non-ideal cases, and Figure 4.6 and Figure 4.7 compare the ideal and non-ideal collection cases for the deterministic and Monte Carlo models, respectively. From Figure 4.4 it appears that the Monte Carlo model estimates the collection efficiency better than the deterministic for the ideal collection case, especially for the larger particle sizes. It is apparent that both model are insufficient for the non-ideal collection case. The dust particles used in the Tomb *et al.* experiments were pulverized Pennsylvania coal dust, the composition of which

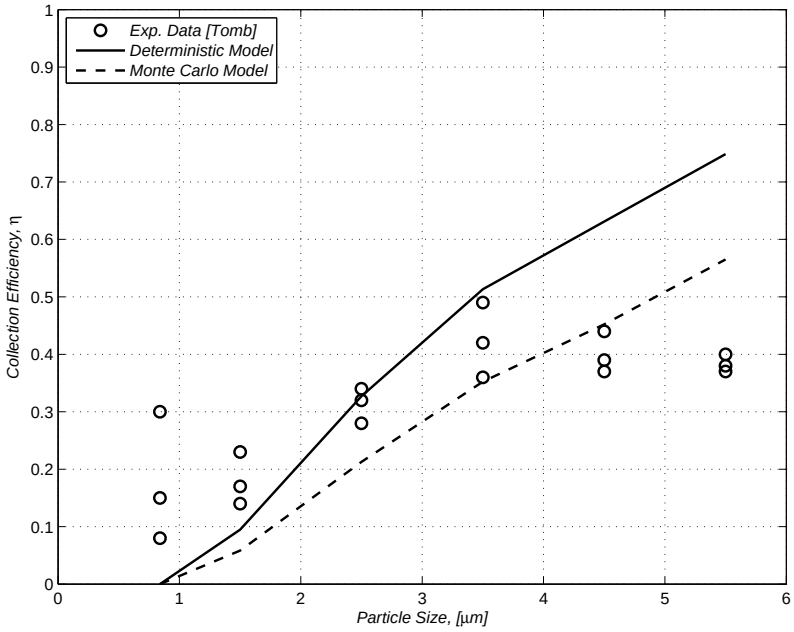

Fig. 4.4. Ideal Collection Model Comparison to Experimental Data from Tomb *et al.*

was not listed by Tomb, but the assumption that the coal dust is not water soluble is probably valid, suggesting that more factors are at work for the collection of small diameter dust particles.

The overall collection efficiency results for the deterministic model using ideal collection are presented in Figures 4.8 and 4.9, against air flow rate and non-dimensionalized number density, respectively . The collection efficiency was calculated for 100 to 500 micron drops and compared to the average overall collection efficiency from the experimental data. Both the deterministic and Monte Carlo models assume a once-thru approach, meaning the aerosol particle pass straight through the spray region. As will be seen later in Section 5.4, the once-thru assumption breaks down in the physical system because of the flow fields produced.

The deterministic model shows the same general trend as the experimental data. The smaller air flow rates result in a higher collection efficiency. Note that the

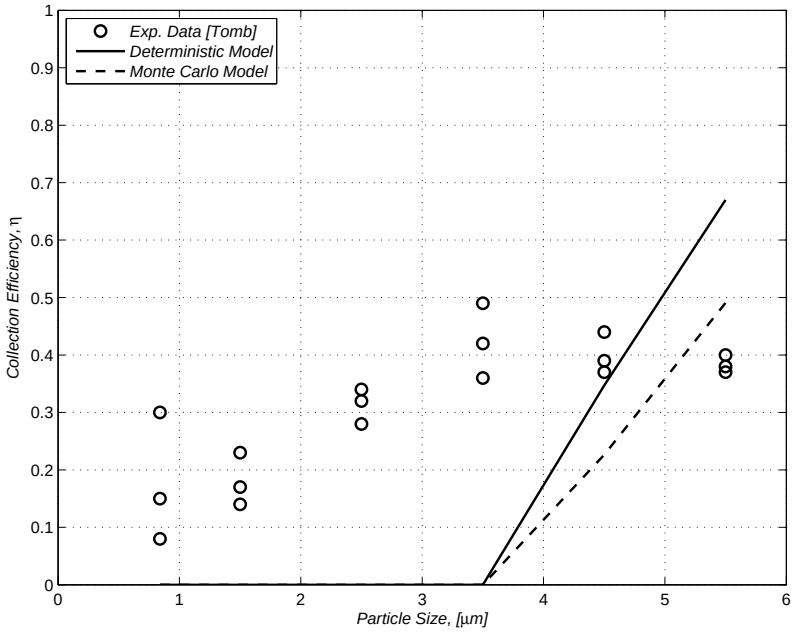

Fig. 4.5. Non-Ideal Collection Model Comparison to Experimental Data from Tomb *et al.*

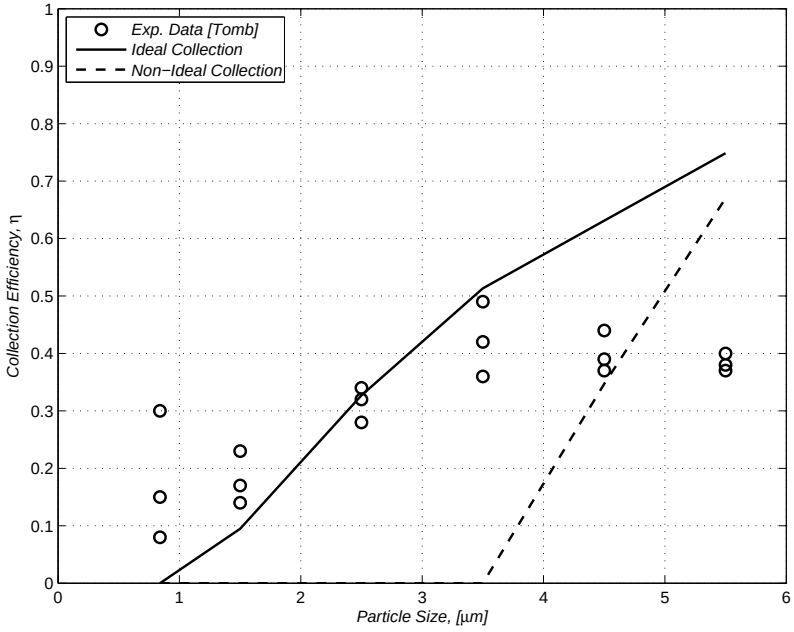

Fig. 4.6. Deterministic Model Compared to Experimental Data from Tomb *et al.*

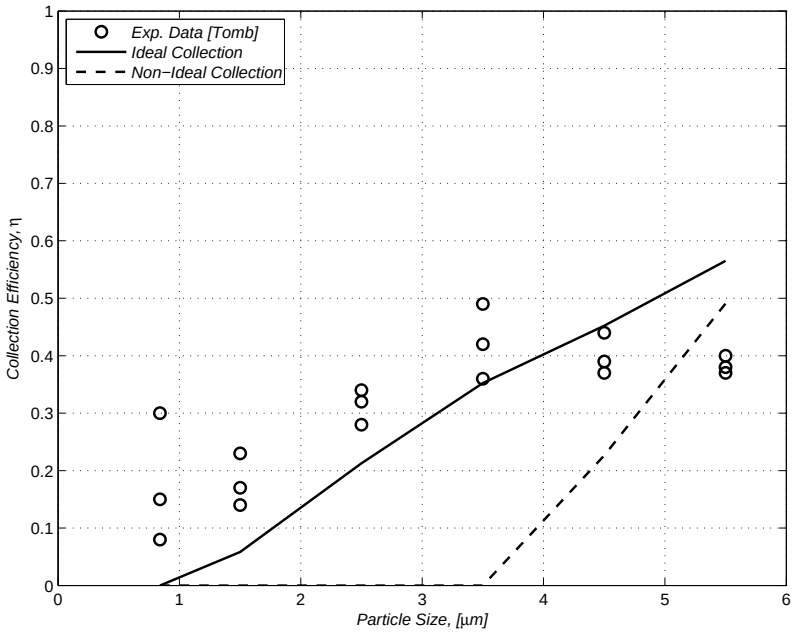

Fig. 4.7. Monte Carlo Model Compared to Experimental Data from Tomb *et al.*

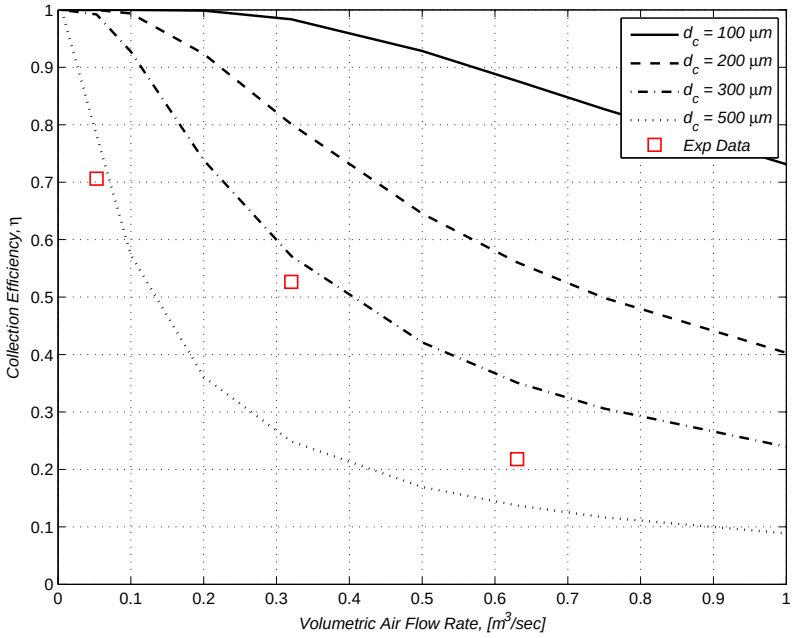

Fig. 4.8. Model Collection Efficiency vs. Air Flow Rate for Ideal Collection [Deterministic]

collection efficiency for the smaller drops are counter-intuitively higher than the larger drops. This is simply because the theoretical velocity for the larger drops are lower than the small drops, at a certain distance from the nozzle, because of the increased effect of the drag force. The results suggest that the average size of the drops in the experimental system are between 300 and 500 microns. Unfortunately, the drop size in the experiment is an unknown. The nozzle company reported the volume mean diameter (VMD) as about 850 microns at a water pressure of 40 psi [35], but did not report the geometric standard deviation, σ_g. This means that the number mean diameter could not be calculated from the given data.

An estimate of the maximum drop size was suggested by Walton and Woolcock [17] related to the velocity of the drop. They suggest that the maximum drop radius is given by $u^2R = 306$, where u is the velocity in m/s, and R is the drop radius in mm. The superficial exit velocity of the drops in the experiment conducted

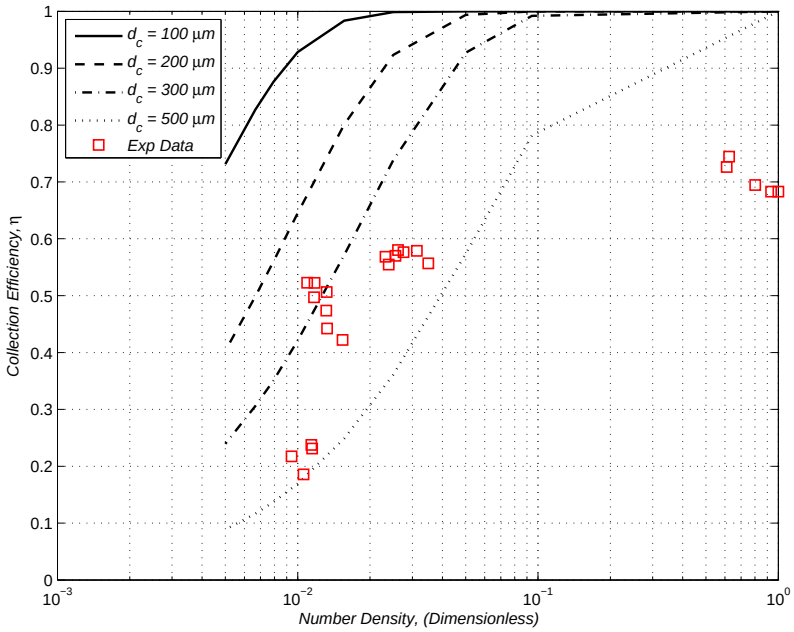

Fig. 4.9. Collection Efficiency vs. Non-Dimensionalized Number Density for Ideal Collection [Deterministic]

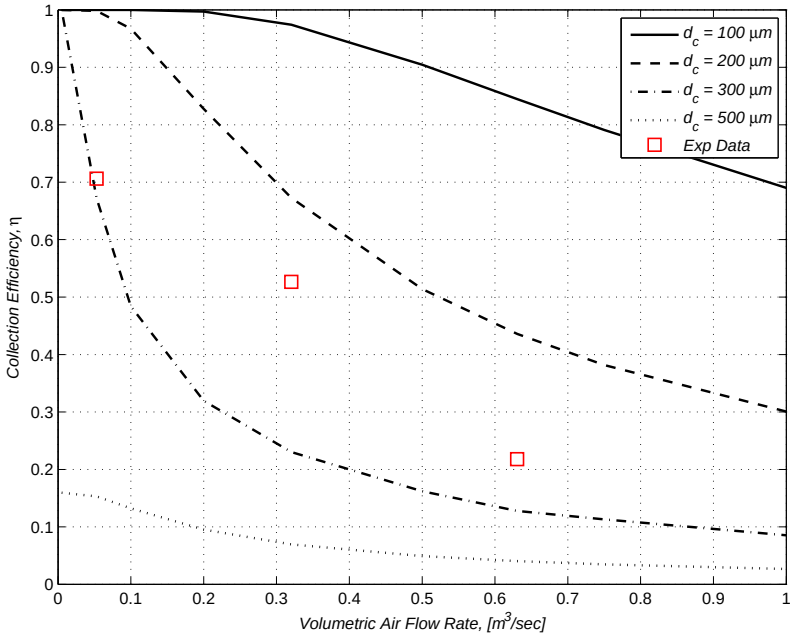

Fig. 4.10. Collection Efficiency vs. Air Flow Rate for Non-Ideal Collection [Deterministic]

in this research was calculated to be about 41.8 m/s. This means that the maximum radius according to Walton and Woolcock would be 175 micron. Obviously, drops will interact with each other and create larger drops, meaning this estimate is probably valid based on Figure 4.8.

The results for the non-ideal collection case for the deterministic model are presented in Figures 4.10 and 4.11. They show the expected result of a lower collection efficiency than the ideal collection case. Based on these results, it appears that the drop size is between 200 and 300 microns. Without the actual drop size measurements, however, no claim can be made that this is actually the case.

The general trend given by the Monte Carlo model analysis is relatively the same as the deterministic model, except the Monte Carlo method estimates lower collection efficiencies than the deterministic model. According to Cheng [10], the deterministic model does not change the interparticle spacing between layers, suggesting the

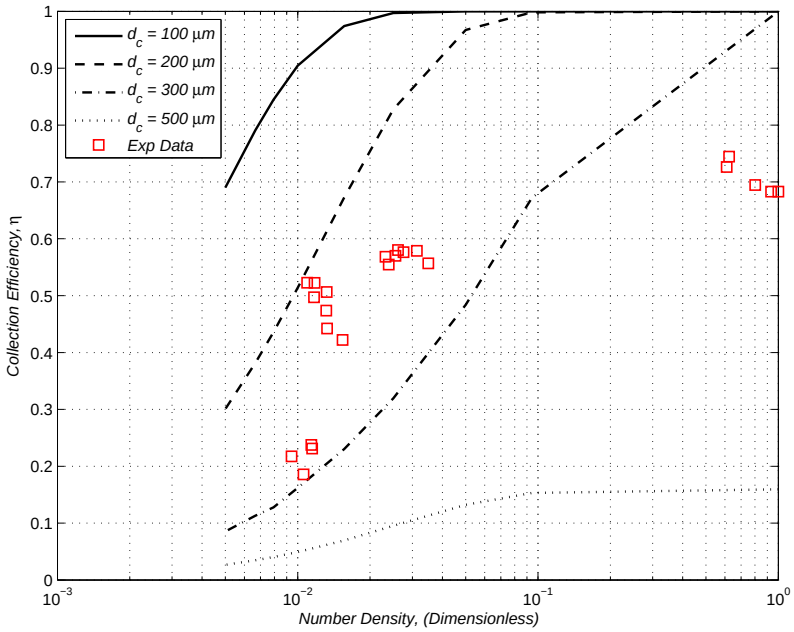

Fig. 4.11. Collection Efficiency vs. Non-Dimensionalized Number Density for Non-Ideal Collection [Deterministic]

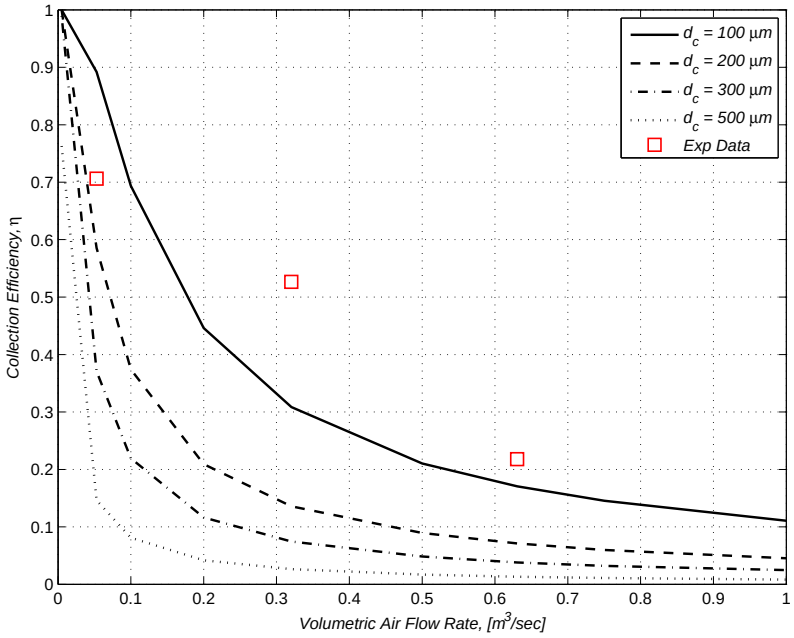

Fig. 4.12. Collection Efficiency vs. Air Flow Rate for Ideal Collection [Monte Carlo]

particle number density is held constant. The Monte Carlo model does adjust the particle number density between layers, accounting for the lower overall collection efficiencies. The results of the ideal collection case for the Monte Carlo method are presented in Figures 4.12 and 4.13, while the results for the non-ideal collection case are presented in Figures 4.14 and 4.15.

A comparison of the deterministic and Monte Carlo methods for a 200 micron size drop are presented in Figures 4.16 to 4.19. The ideal and non-ideal collection for 200 micron drops in the Monte Carlo method are presented in Figures 4.20 and 4.21 simply for direct comparison of the ideal and non-ideal cases. Again, it is difficult to say which method produces the better results because the drop size distribution is unknown.

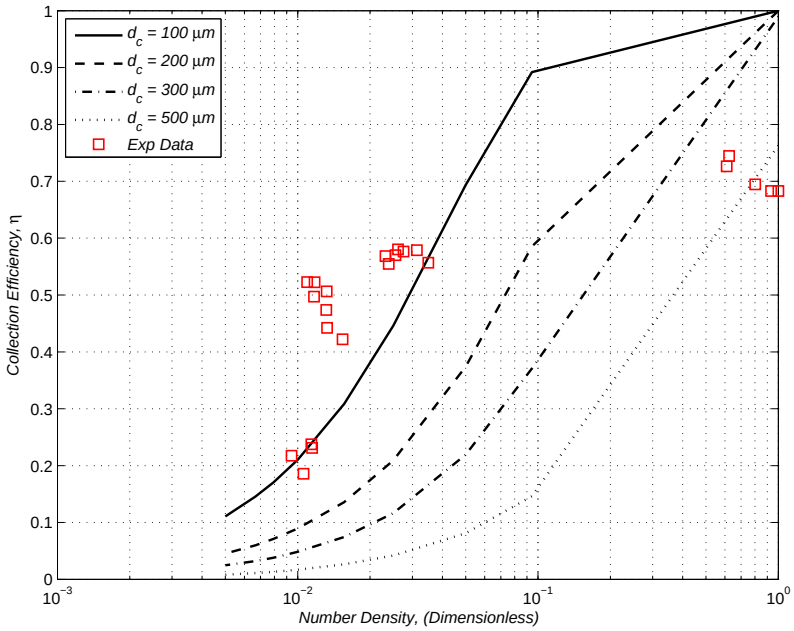

Fig. 4.13. Collection Efficiency vs. Non-Dimensionalized Number Density for Ideal Collection [Monte Carlo]

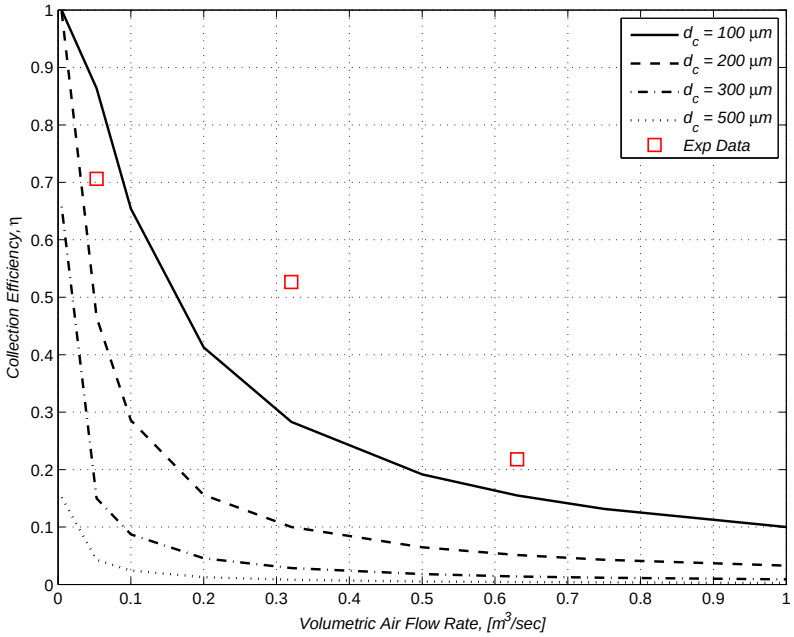

Fig. 4.14. Collection Efficiency vs. Air Flow Rate for Non-Ideal Collection [Monte Carlo]

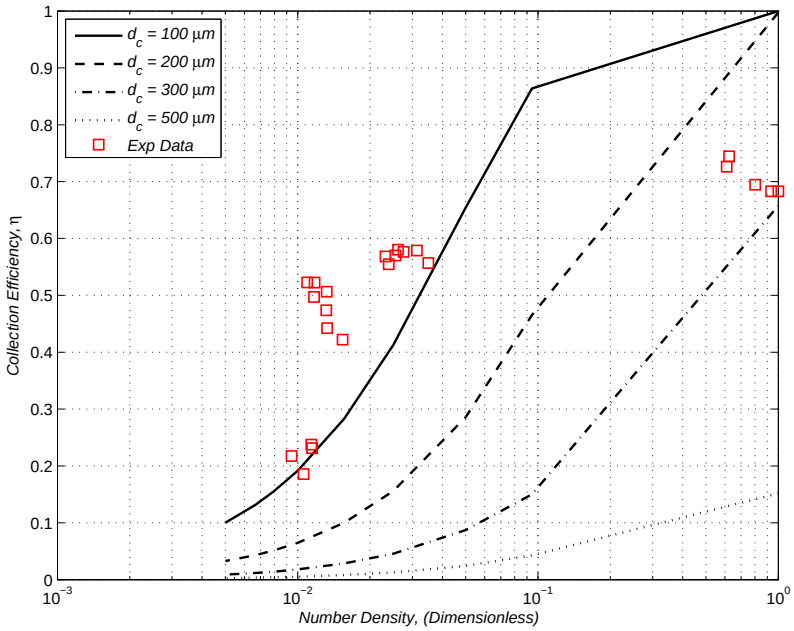

Fig. 4.15. Collection Efficiency vs. Non-Dimensionalized Number Density for Non-Ideal Collection [Monte Carlo]

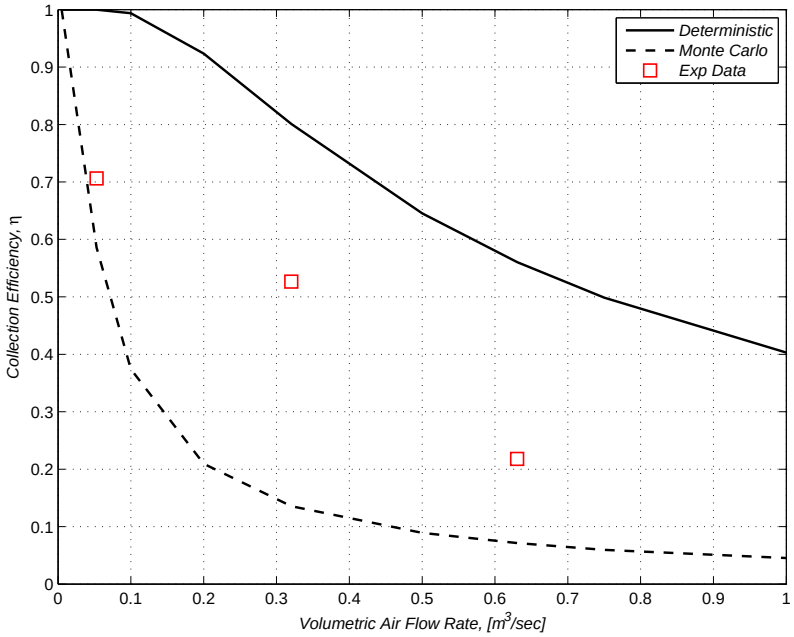

Fig. 4.16. Comparison of Deterministic and Monte Carlo Methods for Ideal Case vs. Air Flow Rate, $d_c = 200\mu m$

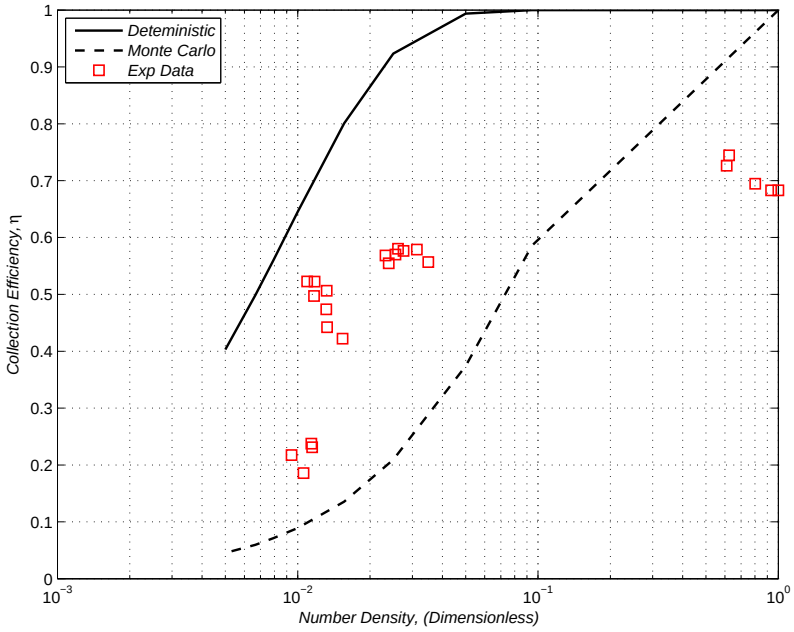

Fig. 4.17. Comparison of Deterministic and Monte Carlo Methods for Ideal Case vs. Non-Dimensionalized Number Density, $d_c = 200\mu m$

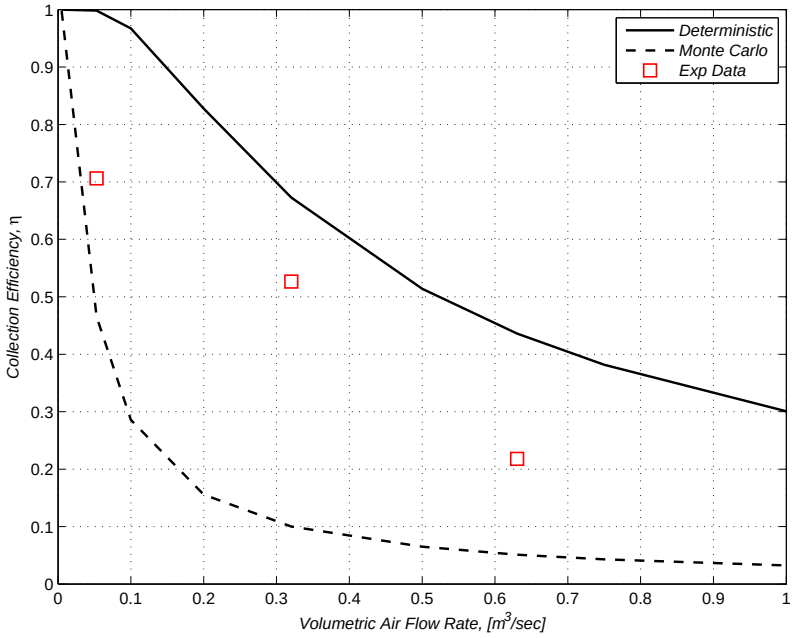

Fig. 4.18. Comparison of Deterministic and Monte Carlo Methods for Non-Ideal Case vs. Air Flow Rate, $d_c = 200\mu m$

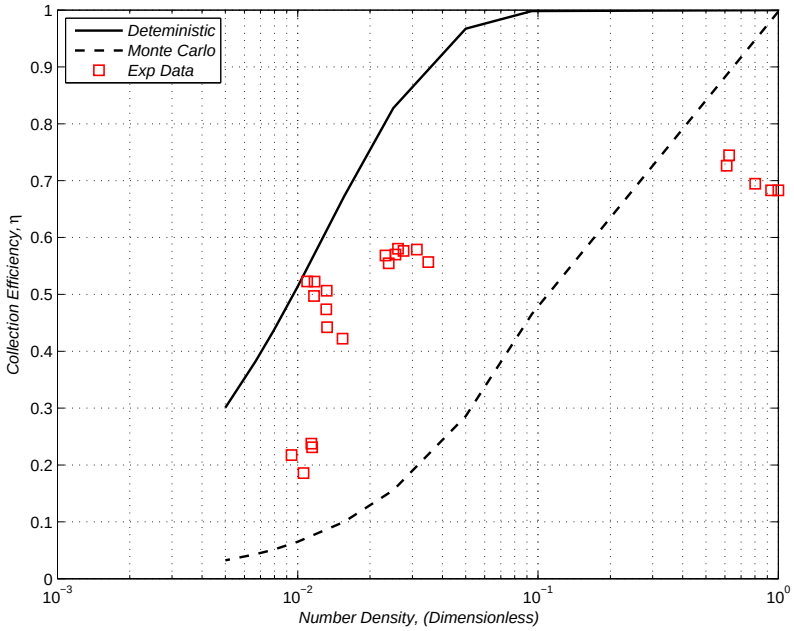

Fig. 4.19. Comparison of Deterministic and Monte Carlo Methods for Non-Ideal Case vs. Non-Dimensionalized Number Density, $d_c = 200\mu m$

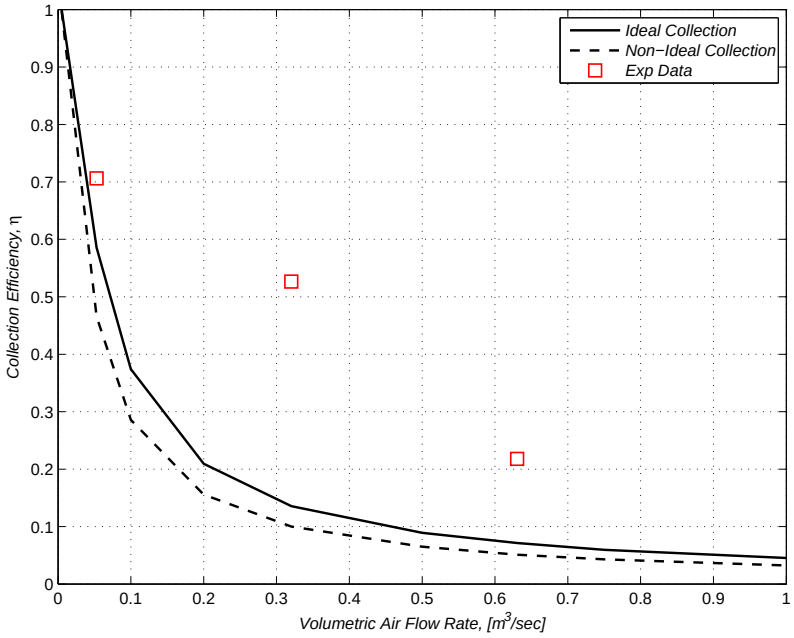

Fig. 4.20. Comparison of Ideal and Non-Ideal Case vs. Air Flow Rate for the Monte Carlo Model, $d_c = 200\mu m$

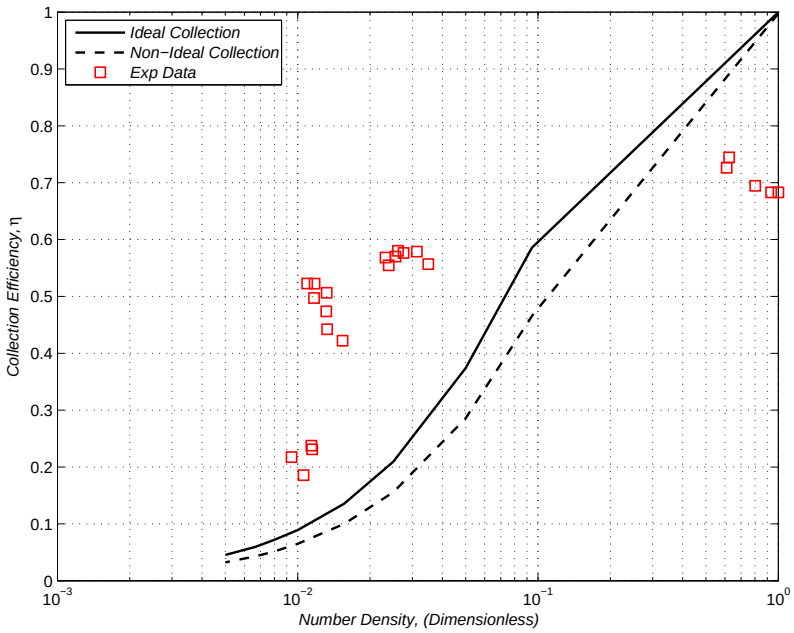

Fig. 4.21. Comparison of Ideal and Non-Ideal Case vs. Non-Dimensionalized Number Density for the Monte Carlo Model, $d_c = 200\mu m$

5. COMPUTATIONAL FLUID DYNAMIC MODELS

Computational Fluid Dynamic (CFD) analyses were performed as a supplement to the experiment and theoretical models outlined in Sections 3 and 4. The CFD calculations will present the flow fields generated by the sprays where the data is either ambiguous or unavailable. The CFD software that will be employed is CD-Adapco's STAR-CD, which has the ability to model some of the phenomenological aspects of water sprays. This section will begin by describing the options available to CFD users to solve the problem at hand. Next, details of a benchmark problem that was selected to ensure the modeling practices used are valid will be discussed. Finally, the experimental CFD models will be described and thier results presented.

5.1 Introduction to CFD Theory and Options

There are numerous computational options available for use in CFD codes. It would be absurd to cover all the options in this section. Instead, the equations and options used in the CFD models for the benchmark and experiment problems will be introduced for the code selected. Among the topics to be discussed include the basic conservation equations, turbulence modeling options, discretization practices, solution algorithms, and Lagrangian models. The information found in this section originates from the CD-Adapco Methodology Manual [45].

The code uses the basic conservation equations for mass and momentum when solving for compressible and incompressible fluid flows. The equations, also known as the Navier-Stokes equations, in Cartesian tensor notation are [45]

$$\frac{\partial \rho}{\partial t} + \frac{\partial}{\partial x_j}(\rho u_j) = s_m \tag{5.1}$$

and

$$\frac{\partial (\rho u_i)}{\partial t} + \frac{\partial}{\partial x_j}(\rho u_j u_i - \tau_{ij}) = -\frac{\partial p}{\partial x_i} + s_i \tag{5.2}$$

where x_i is the Cartesian coordinate, u_i is the absolute fluid velocity component in the x_i direction, p is the piezometric pressure, τ_{ij} is the stress tensor, s_m are the mass sources, and s_i are the momentum sources. STAR-CD also uses the basic equations for heat transfer, but since the benchmark and experiment are taken to be isothermal those equations will not be covered here. The reader is directed to the CD-Adapco Methodology manual [45] for more information on the basic conservation and closure equations used.

The code offers a variety of turbulent modeling capabilities including Eddy Viscosity, Reynolds Stress, Large Eddy Simulation, and Detached Eddy Simulation models. Each model has its own approximations and should be applied to the appropriate situations, which is usually determined by experience. The Eddy Viscosity model was selected for this study.

The Eddy Viscosity model is based on the relationship between molecular gradient-diffusion and turbulent motion. The stress tensor due to the random fluctuations of the velocity around the ensemble averaged velocity, or Reynolds stresses, are determined by a turbulent viscosity and diffusivity. The turbulent viscosity is resolved from a characteristic turbulent velocity and length scale. Two variations of the Eddy Viscosity model applied to the benchmark problem include the k-ϵ and k-ω models.

The k-ϵ model consists of transport equations for the turbulent kinetic energy, k, and turbulent dissipation rate, ϵ, defined by the characteristic turbulent velocity and length scale, respectively. There are multiple realizations of the k-ϵ model, but only the Standard form is utilized. The general form of the turbulent kinetic energy transport equation for the Standard k-ϵ model is given by Equation 5.3 and the dissipation rate given by Equation 5.8.

$$\frac{\partial}{\partial t}(\rho k) + \frac{\partial}{\partial x_i}\left[\rho u_j k - \left(\mu + \frac{\mu_t}{\mathrm{Pr}_t}\right)\frac{\partial k}{\partial x_j}\right] = \mu_t(P + P_B) - \rho\epsilon - \frac{2}{3}\left(\mu_t\frac{\partial u_i}{\partial x_i} + \rho k\right)\frac{\partial u_i}{\partial x_i} + \mu_t P_{NL} \tag{5.3}$$

where

$$P \equiv S_{ij}\frac{\partial u_i}{\partial x_j} \tag{5.4}$$

$$P_B \equiv -\frac{g_i}{\mathrm{Sc}_t}\frac{1}{\rho}\frac{\partial \rho}{\partial x_i} \tag{5.5}$$

$$P_{NL} = -\frac{\rho}{\mu_t}\overline{u_i' u_j'}\frac{\partial u_i}{\partial x_i} - \left[P - \frac{2}{3}\left(\frac{\partial u_i}{\partial x_i} + \frac{\rho k}{\mu_t}\right)\frac{\partial u_i}{\partial x_i}\right] \tag{5.6}$$

and Pr_t is the turbulent Prandlt number, Sc_t is the turbulent Schmidt number, S_{ij} is the mean strain, u' is the velocity fluctuation around the ensemble averaged flow velocity, and μ_t is the turbulent viscosity given by Equation 5.7.

$$\mu_t = f_\mu \frac{C_\mu \rho k^2}{\epsilon} \tag{5.7}$$

where C_μ is an empirical coefficient and f_μ is the damping function. In Equation 5.3 the first term on the right hand side is the the turbulent generation by shear and normal stresses and buoyancy forces, the second term is the viscous dissipation, the third term describes the increase or decrease in turbulence due to compressibility effects, and the last term is required when a non-linear set of equations is utilized.

$$\begin{aligned}\frac{\partial}{\partial t}(\rho\epsilon) + \frac{\partial}{\partial x_j}\left[\rho u_j \epsilon - \left(\mu + \frac{\mu_t}{\mathrm{Pr}_t}\right)\frac{\partial \epsilon}{\partial x_j}\right] = \\ C_{\epsilon 1}\frac{\epsilon}{k}\left[\mu_t P - \frac{2}{3}\left(\mu_t \frac{\partial u_i}{\partial x_i} + \rho k\right)\frac{\partial u_i}{\partial x_i}\right] + C_{\epsilon 3}\frac{\epsilon}{k}\mu_t P_B - \\ C_{\epsilon 2}\rho\frac{\epsilon^2}{k} + C_{\epsilon 4}\rho\epsilon\frac{\partial u_i}{\partial x_i} + C_{\epsilon 1}\frac{\epsilon}{k}\mu_t P_{NL}\end{aligned} \tag{5.8}$$

In Equation 5.8, the C_ϵ terms are given coefficients. Also in Equation 5.8, the first term on the right hand side is the turbulent dissipation production from linear stresses and compression effects, the second term is the contribution due to buoyancy, the third term is the turbulent dissipation dampening, the fourth term accounts for the increase in dissipation due to density changes, and the last term accounts for non-linear stresses.

The k-ω model is similar to the k-ϵ model, but relates the turbulent kinetic energy to the specific turbulent dissipation rate, ω, which is proportional to k/ϵ. Details of the k-ω model can be found in the CD-Adapco Methodology manual [45].

The conservation equations outlined previously are discretized by the finite volume (FV) method. The face-based data structure is used in STAR-CD for polyhedral control volumes (CV), which were used for meshing the solution domain in the benchmark and experiment models. The code gives the user the ability to chose from a list of first-order or second-order schemes.

First-order schemes typically generate easily solved discretized equations, but sometimes result in gradient smearing, also known as numerical diffusion. The only first order spatial discretization scheme available for use in STAR-CD is the Upwind Differencing (UD) scheme.

Second-order schemes can solve problems that possess steep gradients, but the resulting discretized equations are more difficult to solve. These schemes can sometimes have numerical instabilities and/or give non-physical spatial oscillations. The oscillations are sometimes referred to as numerical dispersion. The second or higher-order schemes available in STAR-CD include Linear Upwind Differencing (LUD), Central Differencing (CD), Monotone Advection and Reconstruction Scheme (MARS), and Blended Differencing. MARS was chosen for the benchmark and experiment problems.

MARS is a two-step scheme that does not rely on any problem dependent parameters to operate correctly. In the first step of the scheme a set of monotone gradients are computed using the Total Variation Diminishing scheme. The cell flow properties and gradients from this step define the discretization. The second step uses reconstructed cell flow properties from the first step to compute fluxes for all the advection properties.

As for the temporal discretization, STAR-CD only uses implicit schemes. There are two options available for approximating the time derivatives including the fully-

implicit Euler scheme and the quadratic backward implicit scheme. The scheme choice depends on the solution algorithm used to solve the problem, which include the PISO and SIMPLE algorithms.

Solution algorithms have been created to solve the sets of simultaneous equations that the implicit method produces. The two algorithms available for use are the PISO and SIMPLE algorithms. The PISO algorithm is typically used to solve transient problems, while the SIMPLE algorithm can be employed to solve a transient or steady-state problem. The benchmark and experiment models developed are solved for the steady-state condition, so the SIMPLE algorithm is employed.

The SIMPLE algorithm solves the set of equations using a predictor-corrector strategy that allows decoupling of the flow equations from each other, allowing them to be solved sequentially. The predictor stage produces a temporary velocity field from the momentum equations and pressure distribution. The velocity field from the predictor stage are used in the corrector stage to check for simultaneous satisfaction of the momentum and continuity balances. Under-relaxation techniques are used for the algorithm to promote convergence.

The convergence of a problem is determined by the normalized absolute residual sum given by

$$R_\phi^k \equiv \frac{\sum |r_\phi^k|}{M_\phi} \tag{5.9}$$

where r_ϕ^k is the residual of the FV solution at a particular cell at iteration k, and M_ϕ is a normalization factor. The computation is terminated when R_ϕ^k becomes smaller than some user defined value. The user defined value is typically on the order 10^{-3}.

The benchmark and experiment problems that will be described later make use of water sprays, making them multi-phase flow problems. The conservation equations for these types of problems are written in a Lagrangian or Eulerian form. The continuous phase is written in Eulerian form while the discrete phase is written in Lagrangian form. A statistical approach is taken when solving the discrete phase for

a large number of dispersed elements, which gives rise to the concept of a parcel. A computational parcel represents a cluster of elements that have the same properties.

The conservation equations for the carrier gas, or continuous phase, are the same as described at the beginning of this section, but with modifications for the volume fraction, α. The momentum equation for the discrete phase are of the same form as in Section 2.1.2, using Newton's second law of motion. The forces used to describe the momentum of the discrete phase include the drag force, of the exact same form given by Equation 2.5, a pressure force, a virtual mass force, and general body forces. The pressure force is given by

$$F_p = -V_d \nabla p \tag{5.10}$$

The virtual mass force is the force required to accelerate the carrier fluid by the drop, given by

$$F_{am} = -C_{am} \rho V_d \frac{d(u_d - u)}{dt} \tag{5.11}$$

where C_{am} is the virtual mass coefficient. The general body force is the effect of gravity on the drop. STAR-CD also has the ability to solve for drop heat and mass transfer for the discrete phase, but those models will not be discussed here since an isothermal condition was assumed for the models that are were developed for the benchmark and experiment problems.

There are numerous droplet breakup models that the user can select when modeling sprays. These models include Reitz and Diwakar, Pilch and Erdman, and Hsiang and Faeth models. All these models rely on the Weber number and wave instabilities to simulate droplet breakup. The Reitz and Diwakar model was chosen for no particular reason.

The Reitz and Diwakar drop break-up model is based on the aerodynamic forces on the drop and can be described by two processes, Bag break-up and Stripping break-up. In Bag break-up the drop expands due to the non-uniform pressure field

and eventually breaks-up when the surface tension forces are overcome. The instability for bag break-up is determined by

$$\mathrm{We} \equiv \frac{\rho|u-u_d|^2 d_c}{2\gamma} \geq C_{b1} \tag{5.12}$$

where We is the Weber number and C_{b1} is an empirical coefficient with a value of 3.6 to 8.4. In Stripping break-up, the drop breaks-up due to shearing off the drop surface. The criteria for the onset of stripping break-up is given by

$$\frac{\mathrm{We}}{\sqrt{Re_d}} \geq C_{s1} \tag{5.13}$$

where C_{s1} is a coefficient with the value 0.5.

STAR-CD also has the ability to model nozzles. Nozzle flow models include the Max Planck Institute (MPI) model and the Modified MPI model. These models identify the creation of a separation/cavitation region emanating from the nozzle entrance. This results in a reduction of the exit cross-sectional area which causes the injection velocity to be higher than expected, when compared to the geometric cross-sectional area of the nozzle. These models define the spray half-angle and size distribution theoretically. There is also an option that allows the user to define the spray half-angle and drop size distribution. The size distribution is given by either a Rosin-Rammler distribution, defined by Equation 5.14, or by a normal distribution, defined by Equation 5.15.

$$Q = 1 - e^{\left[-\left(\frac{D}{X}\right)^q\right]} \tag{5.14}$$

$$f(D) = \frac{1}{s_n\sqrt{2\pi}} e^{\left[-\frac{1}{2s_n^2}(D-\bar{D})^2\right]} \tag{5.15}$$

In Equation 5.14, Q is the fraction of volume occupied by drops of diameter less than D and X and q are constants supplied by the user. In Equation 5.15, s_n is the deviation of the drop of size D from the mean diameter $\bar{D}$.

The code allows a number of phenomena to be modeled when running a transient calculation, such as collisions between drops and drop splashing when colliding with

walls. The collision model only pertains to collisions between drops of the same species, therefore STAR-CD can not model aerosol capture by sprays. Hence, the key aspects to be quantified using STAR-CD will be air entrainment and characterization of the resultant velocity field.

5.2 Benchmark Problem

When first using any code it is good practice to demonstrate the codes accuracy for the problem being modeled and to make sure the user is properly modeling the problem. For this reason a benchmark problem was selected to verify the accuracy and use of the CFD code selected for this research. The benchmark problem [46, 47] was selected to demonstrate the validity of CFD on the hydrodynamic effects of sprays on a quiescent atmosphere.

5.2.1 Description

St-Georges and Buchlin [46] studied the effectiveness of liquid sprays and curtains absorbing toxic or flammable gases. Their study experimentally measured the characteristics of a single spray. They then developed a numerical model and compared results. The experimental measurements will be used in this study for CFD comparison purposes.

The experimental measurements were done at the von Karman Institute, in Belgium, using laser velocimetry to measure droplet velocity data and the phase method to determine the drop size distribution. The lenses used for the Phase-Doppler Particle Analyzer (PDPA) receiver allowed measurement of droplets of about 10 to 2000 μm to be measured. Measurements were taken at distances of 0.25, 0.45, 0.65, 0.85, and 1.05 m from the nozzle tip.

Measurements were performed on a Lechler number 402.962 full cone pressure nozzles with a spray half angle of 30° and an orifice diameter of 6.25 mm. The

nozzle was fed by a volumetric pump that could deliver up to $10^{-3}m^3/s$ under 800 kPa. The characteristics measured for the liquid phase included the local drop size distribution, average drop diameter, velocity distribution, and the flow rate. The spray envelope was measured based on the definition, which states that 95 % of the total liquid flow rate is contained within the spray envelope.

The gas phase measurements could not be done directly using laser velocimetry. The gas phase velocity was measured indirectly using the small drops present within the spray. The average velocity of the small drops can be considered close to the gas phase because of their low inertial and drag forces. The drop size considered to be small enough for these measurements was about 20 μm or smaller. This method of gas phase velocity measurement is sufficient in the spray region, but could not be used in the envelope region. In the envelope region additional particles were introduced. The particles used were from incense smoke and had a diameter on the order of 20 μm.

The numerical model they developed is comprised of a complete system of coupled ordinary differential equations (ODE) of the first order. The equations for the model are derived from the mass and momentum conservation equations and are then solved using a fourth order Runge-Kutta scheme. Their model assumes steady state flow, an axisymmetric spray, a droplet size distribution with a finite number of class sizes, spherical droplets, and negligible heat and mass transfer. The reader is referred to the St-Georges [46] article for more information on the numerical model.

5.2.2 Model Setup

The CFD model was created to emulate the experimental setup described in Section 5.2.1. The CFD model developed was a three-dimensional problem that used a polyhedral mesh. An optimization study was conducted to determine the mesh size that should be used for the desired results.

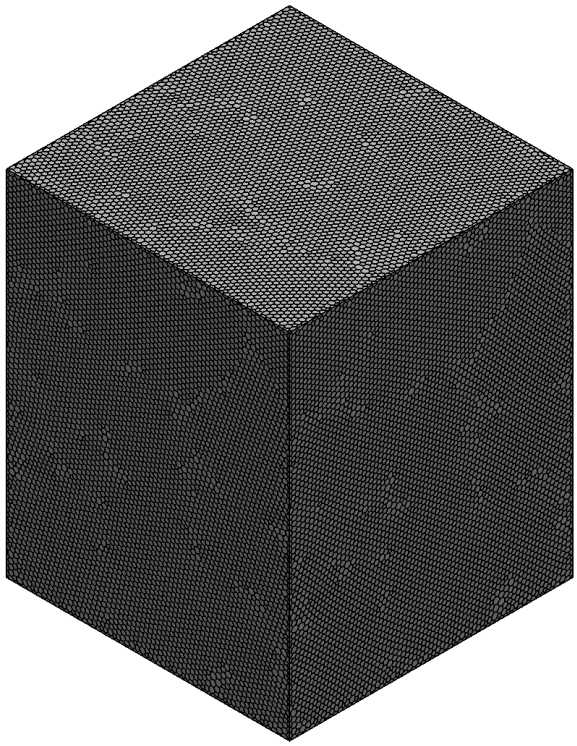

Fig. 5.1. Isometric View of the Benchmark Meshed Computational Domain

The computational domain is simply a rectangular region, see Figure 5.1 that is 2 m in width, 2 m in length, and 2.5 m tall. The top of the region is defined as a wall, the sides are pressure boundaries, and the bottom is defined as an outlet. The mesh size was varied during the optimization study from 4.5 % to 1.0 % of the model size, which relates to a mesh size of 0.0975 m to 0.0217 m. Table 5.1 details the mesh sizes and Figure 5.2 presents a close up view of the polyhedral cells.

The steady-state solution for the domain velocity field was desired, so the SIMPLE algorithm was used to solve the problem with the MARS discretization scheme employed. The problem was assumed to be isothermal, so liquid and gas properties, at 20°C, were held constant. The k-ϵ and k-ω turbulence models were used at the optimum mesh size for comparison purposes.

Table 5.1
Mesh Sizes Used in Optimization Study

Relative Sizing	**Absolute Sizing**		
% of Model	**Surface Mesh**	**Subsurface Thickness**	**Hex Core**
4.5	0.0975	0.0325	0.0975
3.5	0.0758	0.0253	0.0758
2.5	0.0542	0.0180	0.0542
1.5	0.0325	0.0108	0.0325
1.0	0.0217	0.0072	0.0217

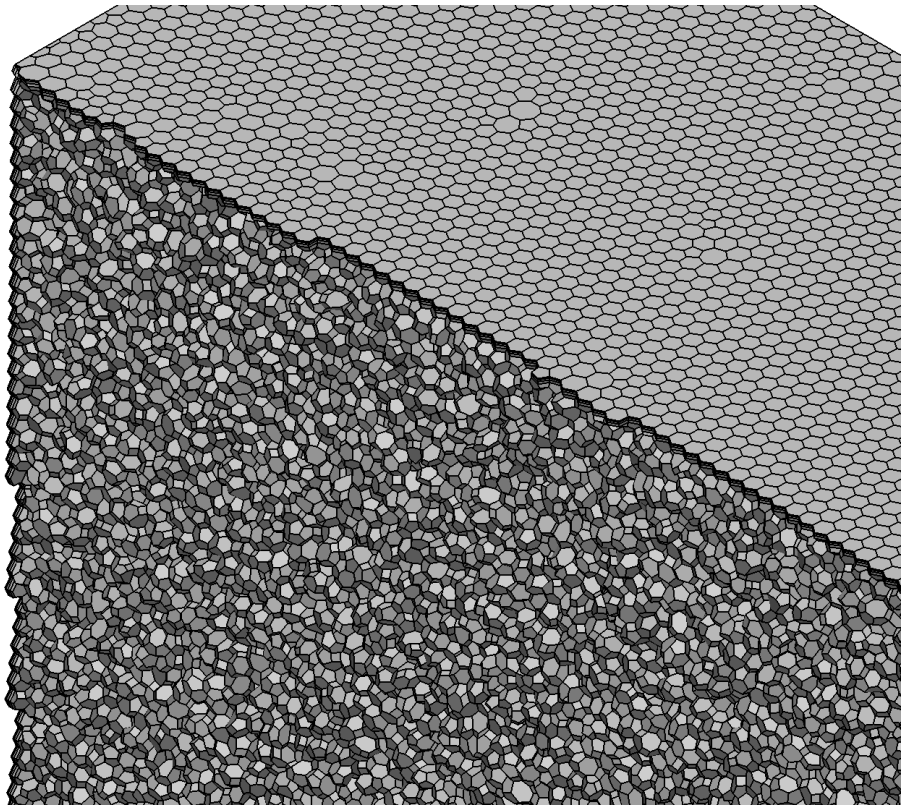

Fig. 5.2. View of Polyhedral Mesh Cells

The spray injection point was located centrally in the domain at a height of 2.3 m. Turbulent dispersion and gravity effect the drop trajectories, and a standard momentum transfer model was used. The drops break-up according to the Reitz and Diwakar model. The Nozzle parameters were defined based on the nozzle used in the benchmark experiment, which corresponds to a spray half angle of 18.5° for a water pressure of 264 kPa. The spray drop size distribution was given by St-Georges [46] in terms of the Rosin-Rammler distribution, with $X = 943.66$ x 10^{-6} m and $q = 2.73$. The water mass flow rate was also given to be 0.4972 kg/s.

5.2.3 Results and Analysis

The results of the optimization study for the k-ϵ turbulence model are presented in Figures 5.3 to 5.6. Figure 5.3 shows the problem central processing unit (CPU) time and total elapsed time for the optimization study versus the problem case number. In conjunction with Figures 5.5 and 5.6, Figure 5.3 demonstrates that the best mesh size to use to optimize both results and execution time is 1.5 % of the model size. Figure 5.4 presents the spray envelope radius, which does not vary much between cases because the initial angle is defined by the user.

It is quite obvious that the sectioned average gas velocity, in Figure 5.5 does not agree with the experimental data from the St-Georges study. This could be because of the measurement technique used for the gas phase. Near the nozzle even the smaller water drops ejected from the nozzle will have an induced velocity from the ejection and may not be the same as the gas velocity at that point. If this is the case, the flow rate would be expected to be larger than the gas flow rate near the nozzle. Further from the nozzle the CFD results still disagree with the experimental results, but not to the degree of the first data point. An interesting result from the experimental study was that the gas velocity profile develops a double hump profile far from the nozzle. This profile does not develop in the CFD results, seen in Figure 5.7. A possible explanation for the double hump profile could be that the

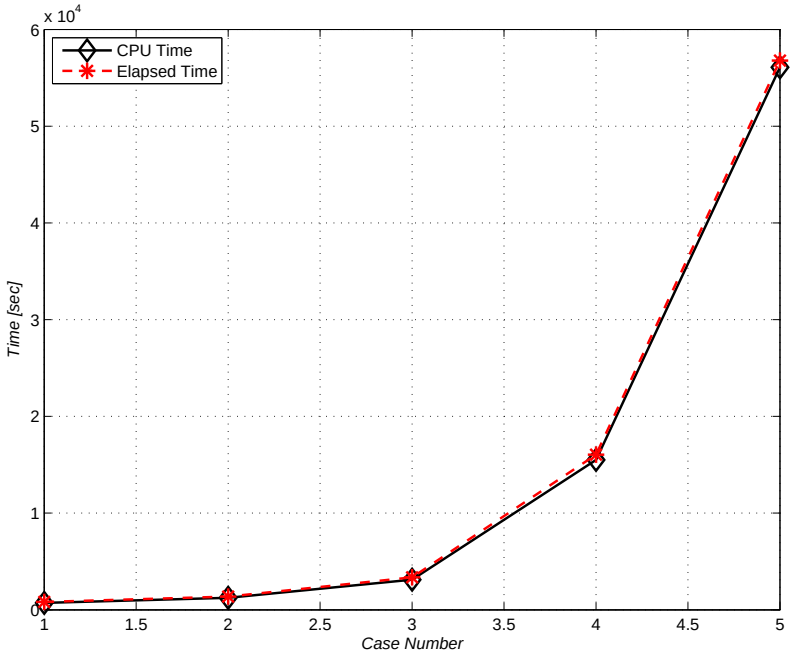

Fig. 5.3. CFD Execution Time for Mesh Optimization Study

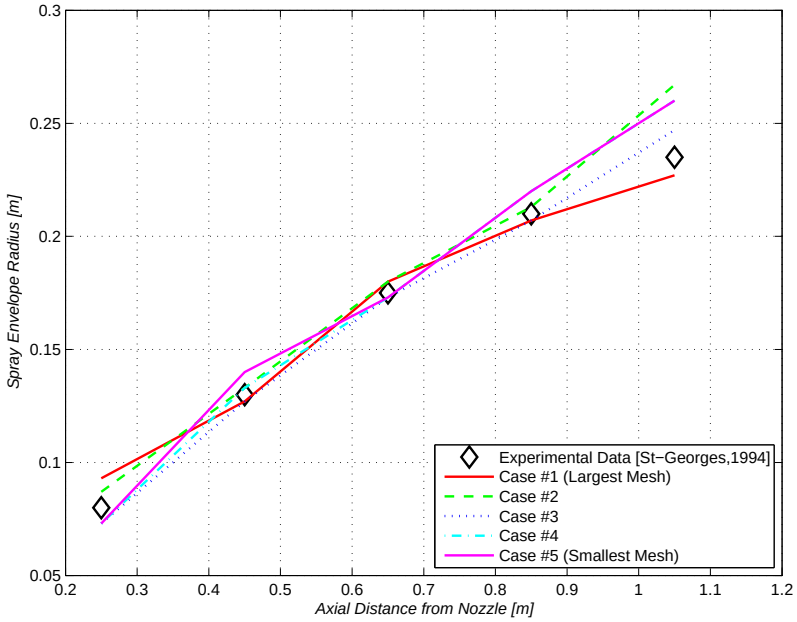

Fig. 5.4. Envelope Radius for Mesh Optimization Study

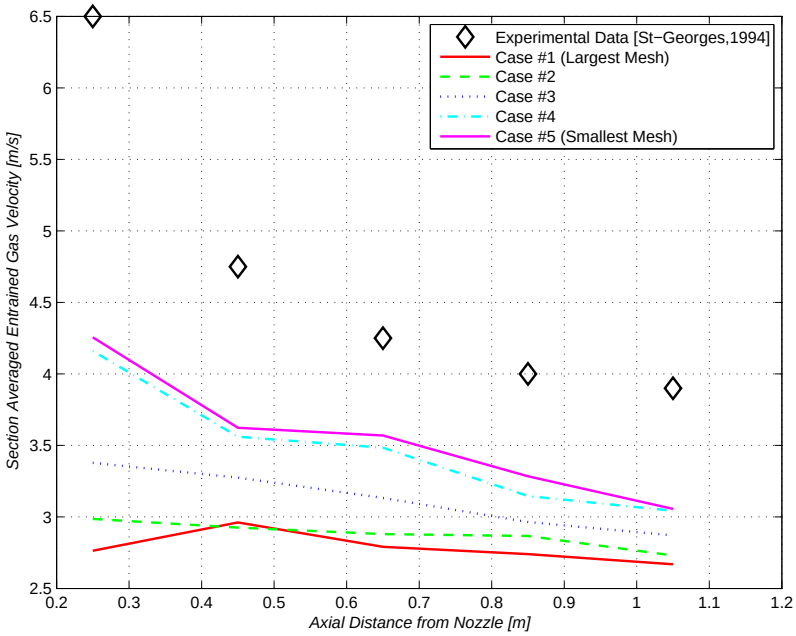

Fig. 5.5. Section Averaged Gas Velocity for Mesh Optimization Study

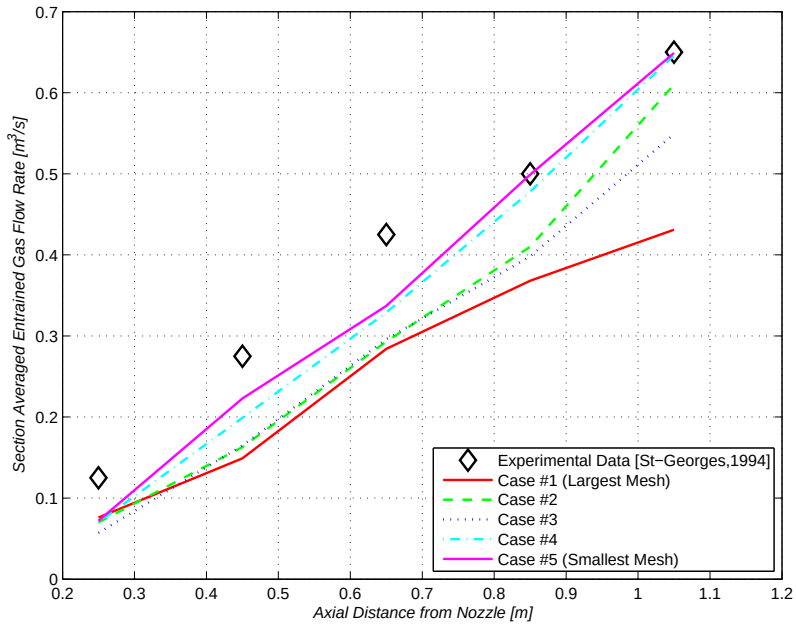

Fig. 5.6. Section Average Gas Flow Rate for Mesh Optimization Study

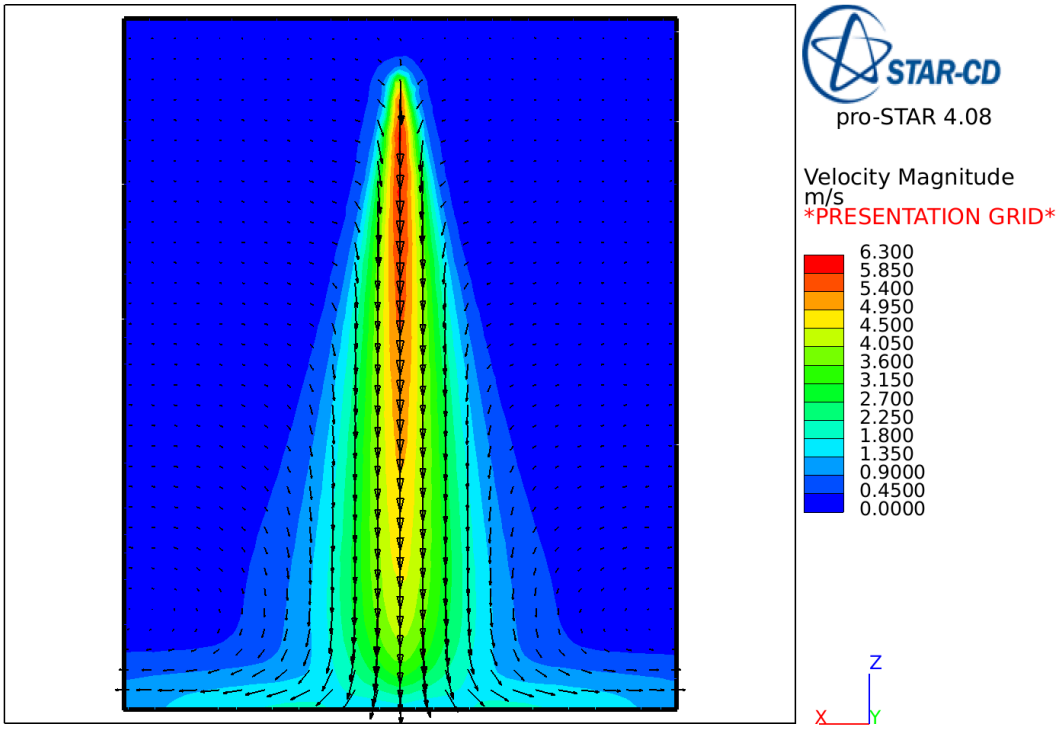

Fig. 5.7. CFD Benchmark Gas Velocity Profile for k-ϵ Turbulence Model

larger water drops are preferentially located near the edges of the spray envelope because of the angular velocity produced at the tip of the nozzle.

The k-ϵ model produces more accurate results than the k-ω model for this problem, as can be seen in Figures 5.8 to 5.10. It is not obvious from the envelope radius (Figure 5.8), but the section averaged gas velocity (Figure 5.9) and gas flow rate (Figure 5.10) show that the k-ϵ model is significantly better than the k-ω model for the given mesh size.

Figure 5.11 is the velocity profile produced for the k-ω model. As proof that the problem is axisymmetric, the iso-surface for the spray is shown in Figure 5.12 for the k-ω models. The iso-surface for the k-ϵ model also shows asymmetry.

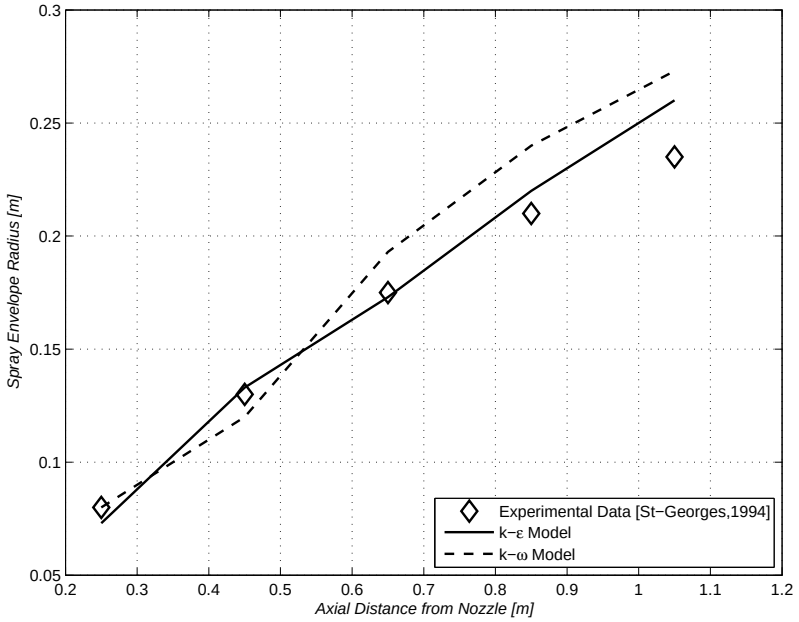

Fig. 5.8. Envelope Radius for Turbulence Models

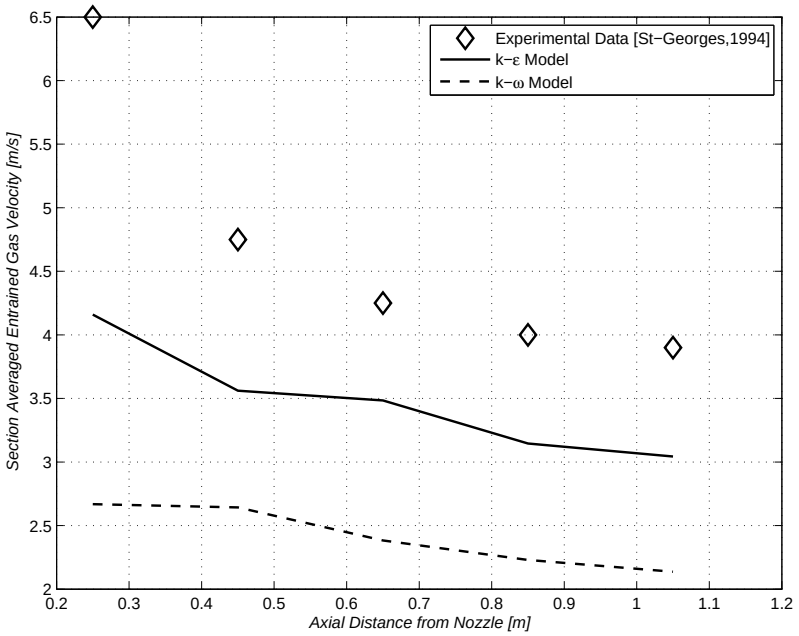

Fig. 5.9. Section Averaged Gas Velocity for Turbulence Models

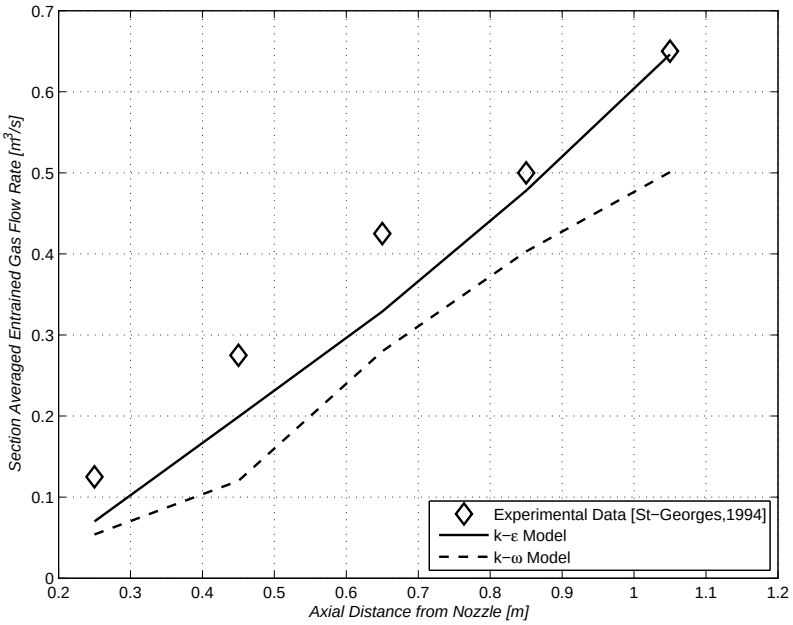

Fig. 5.10. Section Average Gas Flow Rate for Turbulence Models

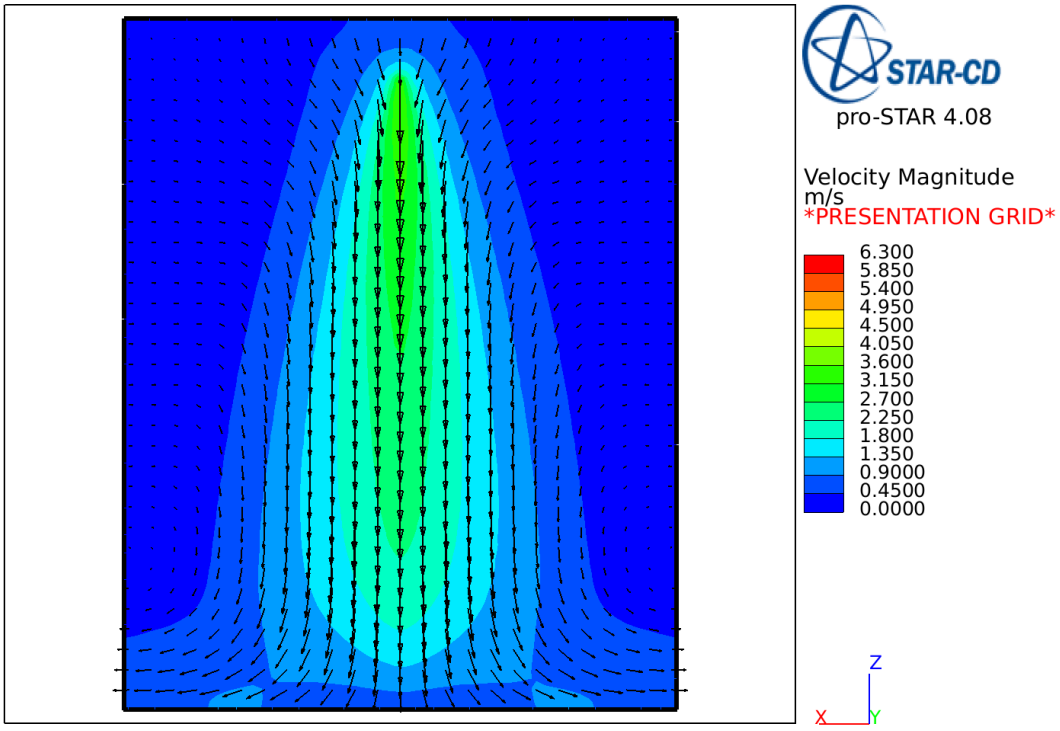

Fig. 5.11. CFD Benchmark Gas Velocity Profile for k-ω Turbulence Model

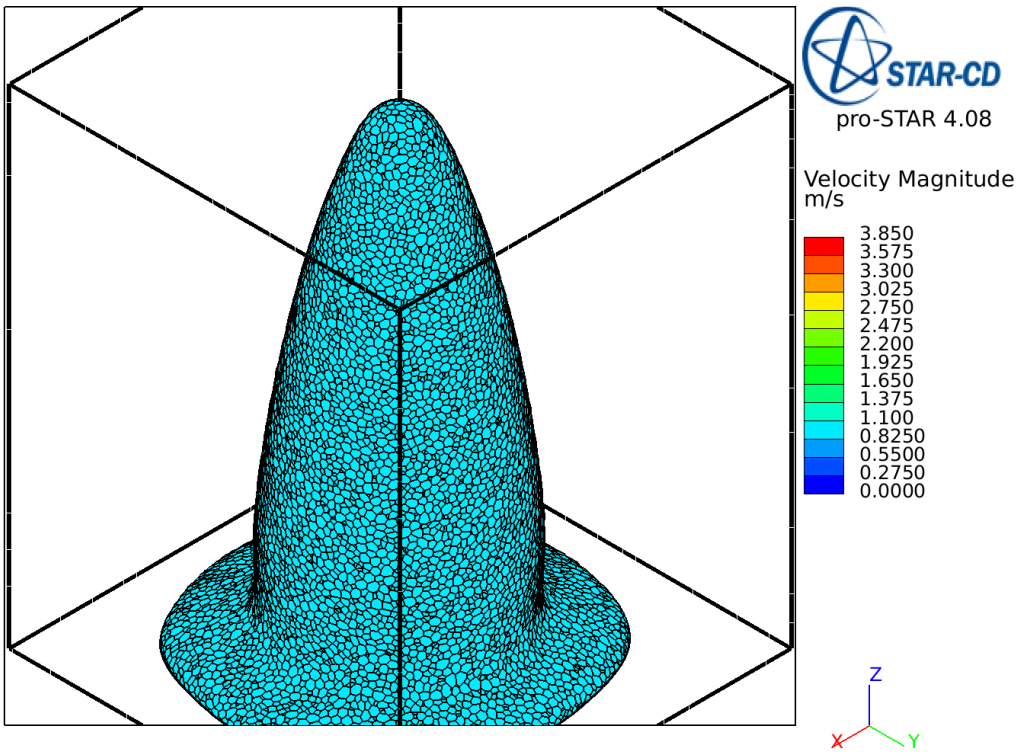

Fig. 5.12. Iso-Surface for k-ω Turbulence Model

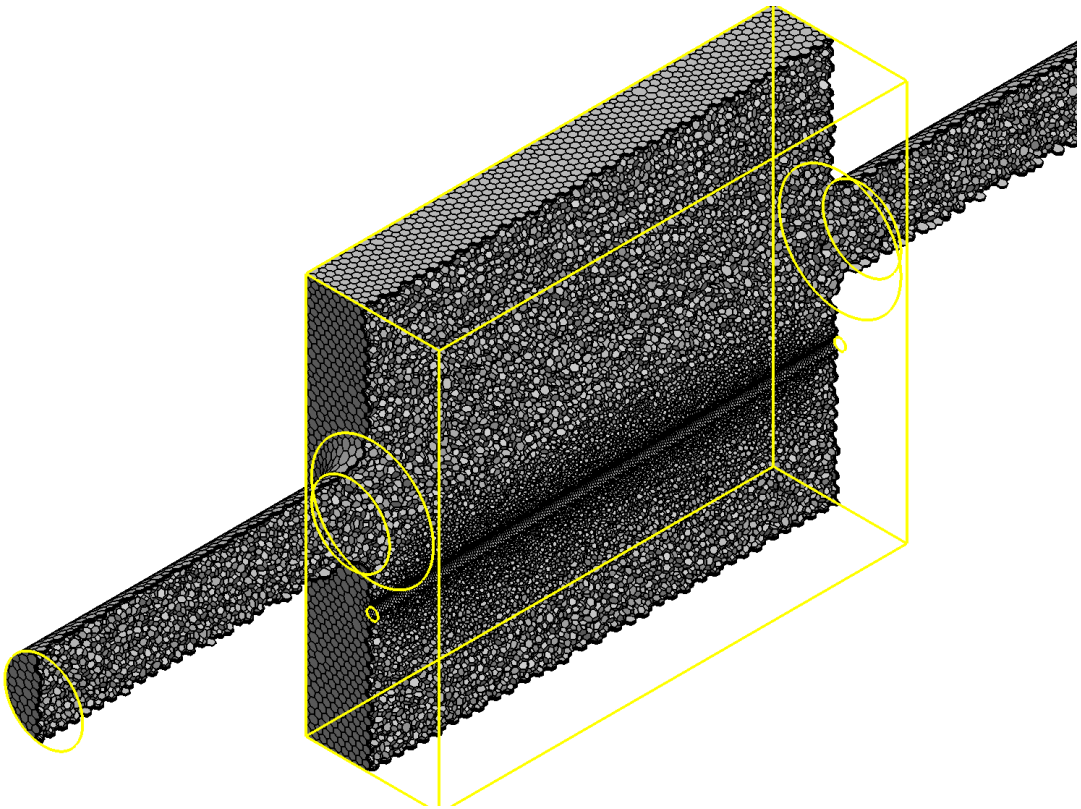

Fig. 5.13. Isometric Cutaway View of Experimental CFD Model

5.3 Experimental Model

The CFD experimental model has the same dimensions given in Figure 3.3 and described in Section 3.1. The problem is meshed using a polyhedral mesh using the generally same surface mesh size found in the optimization study. A finer mesh is used in regions that have tighter curves and angles. The computational domain and mesh is shown in Figure 5.13. The problem is run for a number of different conditions, although the computational domain is kept the same. The computation matrix is given in Table 5.2, where the Nozzle Configuration is defined by Figure 3.4

The fluid and gas material properties in the model were held constant for a temperature of 20°C. The k-ϵ turbulence model was selected for this problem. A steady-state solution is desired, so the SIMPLE algorithm with MARS discretization

Table 5.2
Computational Matrix for Experiment CFD Model

Water Flow Rate [gal/min]	**Air Velocity** [ft/min]	**Nozzle Configuration**
0.0	105	–
0.0	635	–
0.0	1250	–
0.42	635	2
0.42	635	3
0.84	105	1
0.84	635	1
0.84	1250	1

is employed. The water pressure in the experiment was regulated at 50 psi creating a spray half-angle of 27.75° according to the Spray System Co manual [35] for the nozzle model used in the experiment.

The drop size distribution used in the models, unfortunately, may not be representative of the physical system drop size distribution. According to the Spray System Co manual [35], the VMD for the nozzle used at 40 psi is 850 μm, but no geometric standard deviation is reported. Even though the VMD is listed, the geometric standard deviation can significantly change the drop size distribution. For example, for a geometric standard deviation of 1.5, the number mean diameter is 519 μm, while for a geometric standard deviation of 2.0 gives a number mean diameter of 201 μm. This is a significant shift in the size distribution for a change in deviation of 0.5. The geometric standard deviation used for the CFD analysis was 2.0 based on visual inspection of the sprays. This is a significant assumption and needs to be addressed by measuring the spray drop size distribution experimentally.

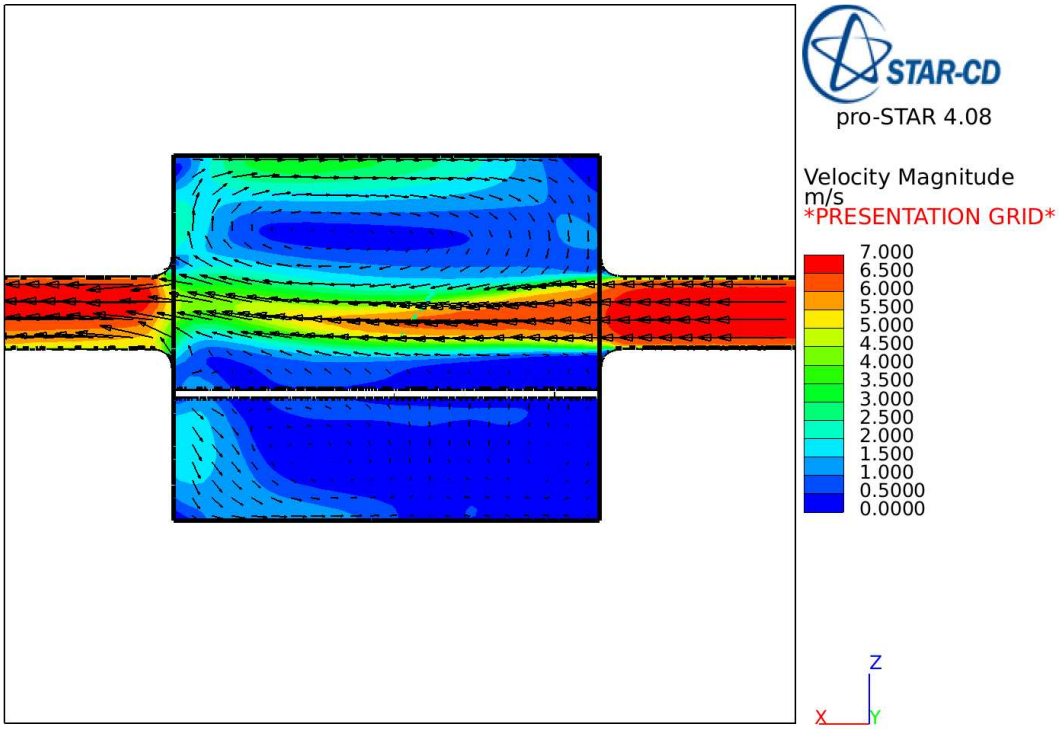

Fig. 5.14. Flow Field for AFR = 1250 *ft/min* and WFR = 0 *gal/min*

5.4 Results and Analysis

The flow fields generated in the experimental design by sprays and the induced air velocity will be presented in this section. Ultimately, the interest is really in how the particles flow through the domain, which will also be presented and discussed. Since no experimental data was taken related to the flow fields generated, the results will be used as a supplement to the experiment and numerical models previously discussed.

Figures 5.14 to 5.16 present the results for a zero water flow rate. As expected, the flow essentially flows directly through the spray region and produces recirculation zones above and below the air flow.

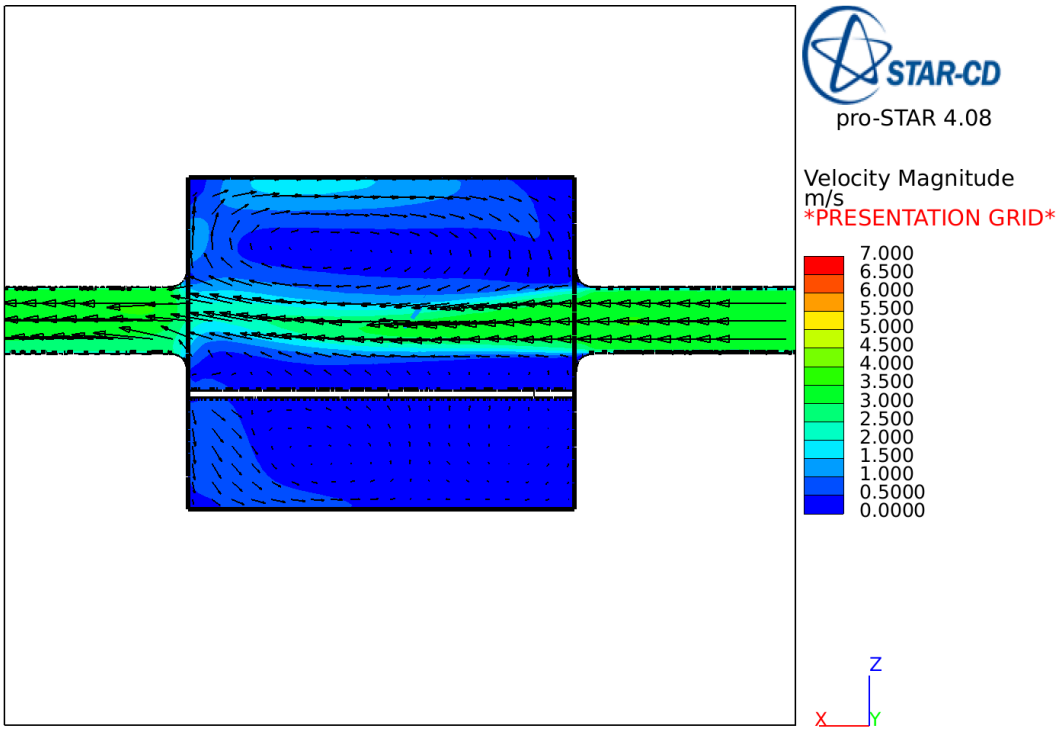

Fig. 5.15. Flow Field for AFR = 635 *ft/min* and WFR = 0 *gal/min*

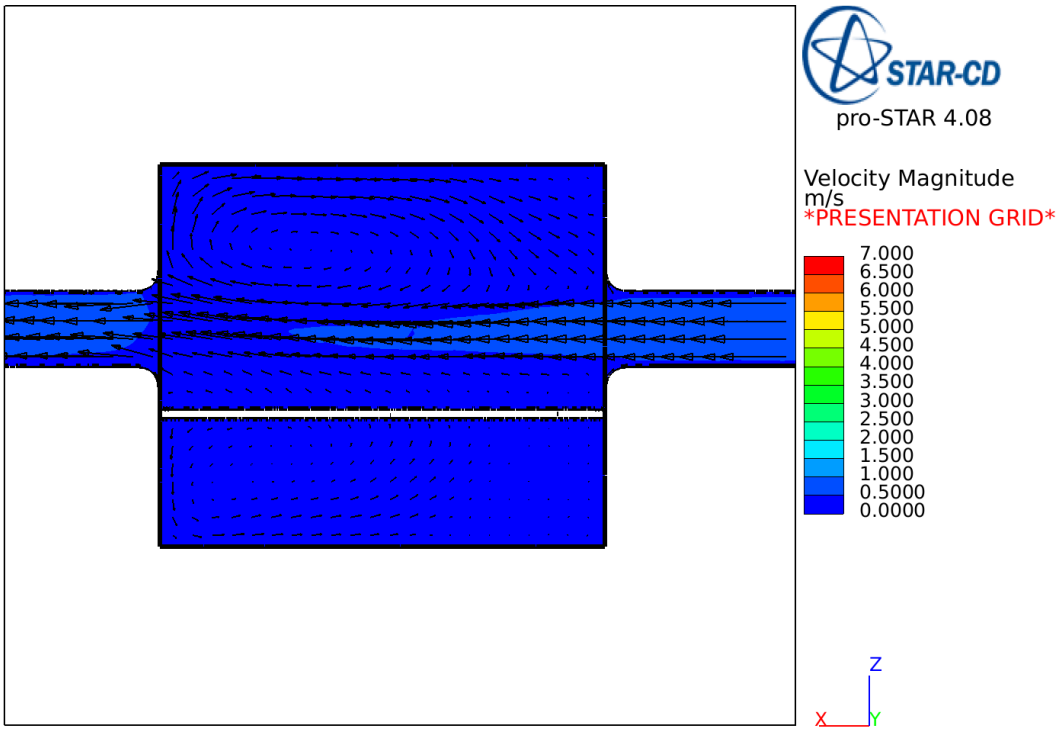

Fig. 5.16. Flow Field for AFR = 105 *ft/min* and WFR = 0 *gal/min*

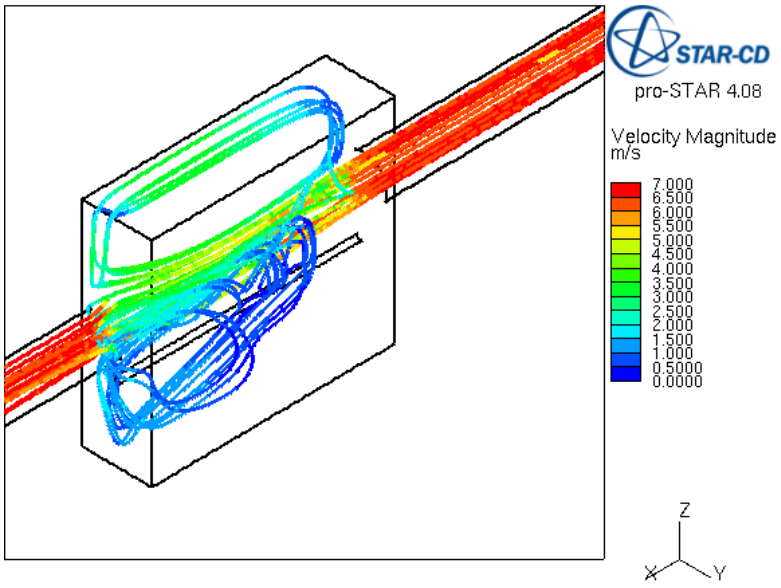

Fig. 5.17. Particle Tracks for AFR = 1250 *ft/min* and WFR = 0 *gal/min*

The corresponding particle tracks were calculated using virtual particles in STAR-CD, which are just particles tracks calculated using the solved flow field (i.e. the particles have no effect on the flow field). The particles diameters were set equal to 20 μm and had a density of 2650 kg/m^3. The tracks are shown in Figures 5.17 to 5.19. The tracks show that the majority of the particles flow right through the spray region, and that those that do not get entrained in the recirculation zones. The particles that get caught in the recirculation zones accounts for a certain percentage of particles that are collected in the system. The particles in these zones could be removed by impacting walls.

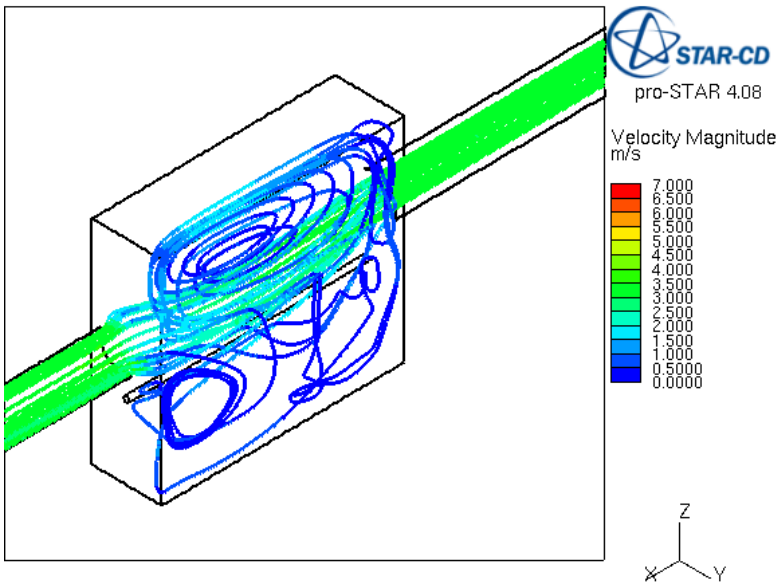

Fig. 5.18. Particle Tracks for AFR = 635 *ft/min* and WFR = 0 *gal/min*

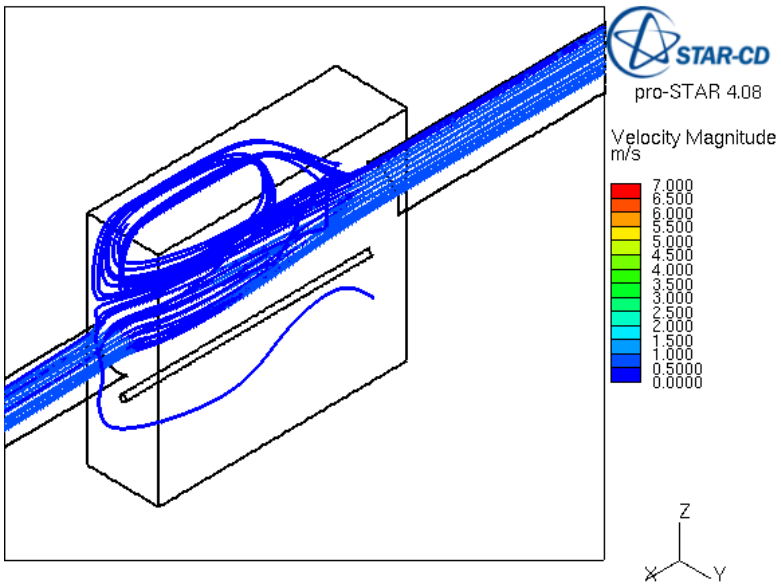

Fig. 5.19. Particle Tracks for AFR = 105 *ft/min* and WFR = 0 *gal/min*

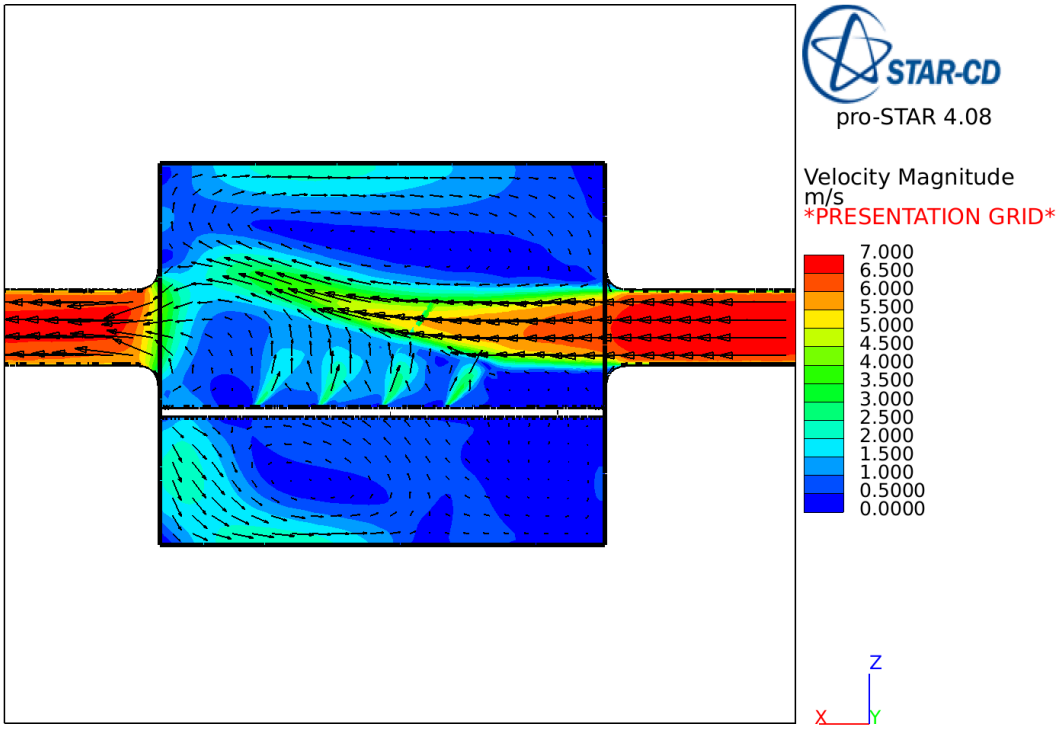

Fig. 5.20. Flow Field for AFR = 1250 *ft/min* and WFR = 0.84 *gal/min*

The results for the highest water flow rate (WFR), nozzle configuration 1, at all air flow rates (AFR) are presented in Figures 5.20 to 5.22. The hydrodynamic effect of the sprays begin to dominate for the lower air flow rate cases, which in essence captures more particles in the spray region, as can be seen in Figures 5.23 to 5.25. It should be noted that the term capture is used to describe the number of particles retained in the spray region due to the hydrodynamic effects of the sprays and not the capture by the drops themselves. The CFD code is unable to calculated collisions between different species, and therefore can not calculate the capture by drops. The longer retention times in the spray region, however, can lead to increased drop-particle interactions.

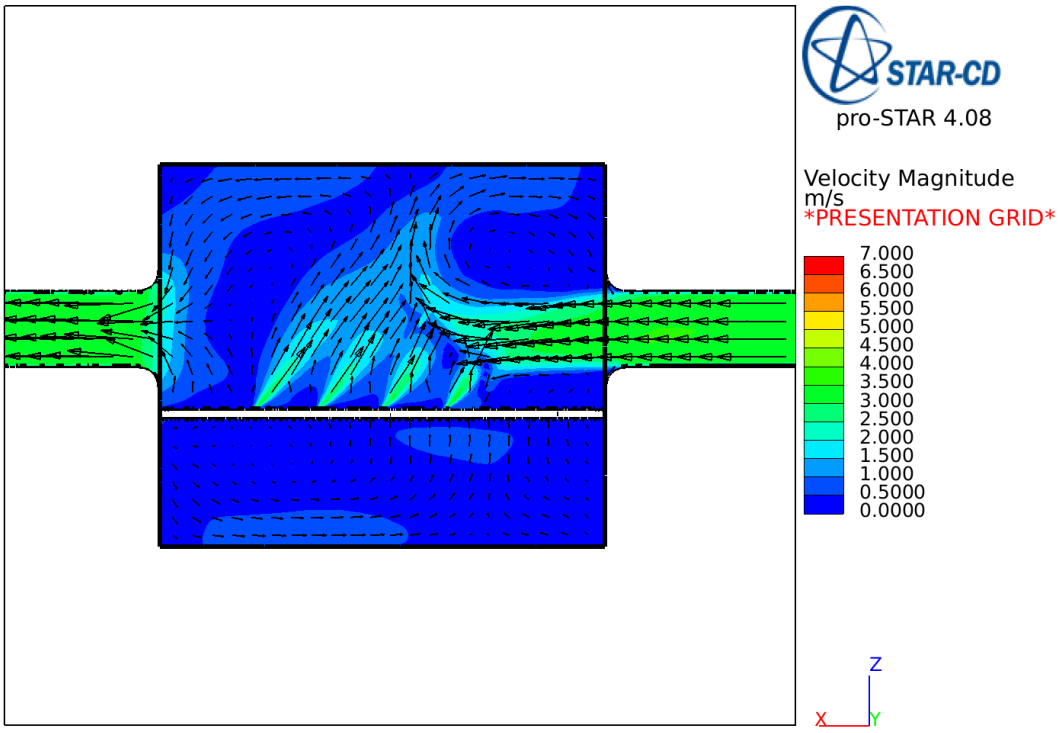

Fig. 5.21. Flow Field for AFR = 635 *ft/min* and WFR = 0.84 *gal/min*

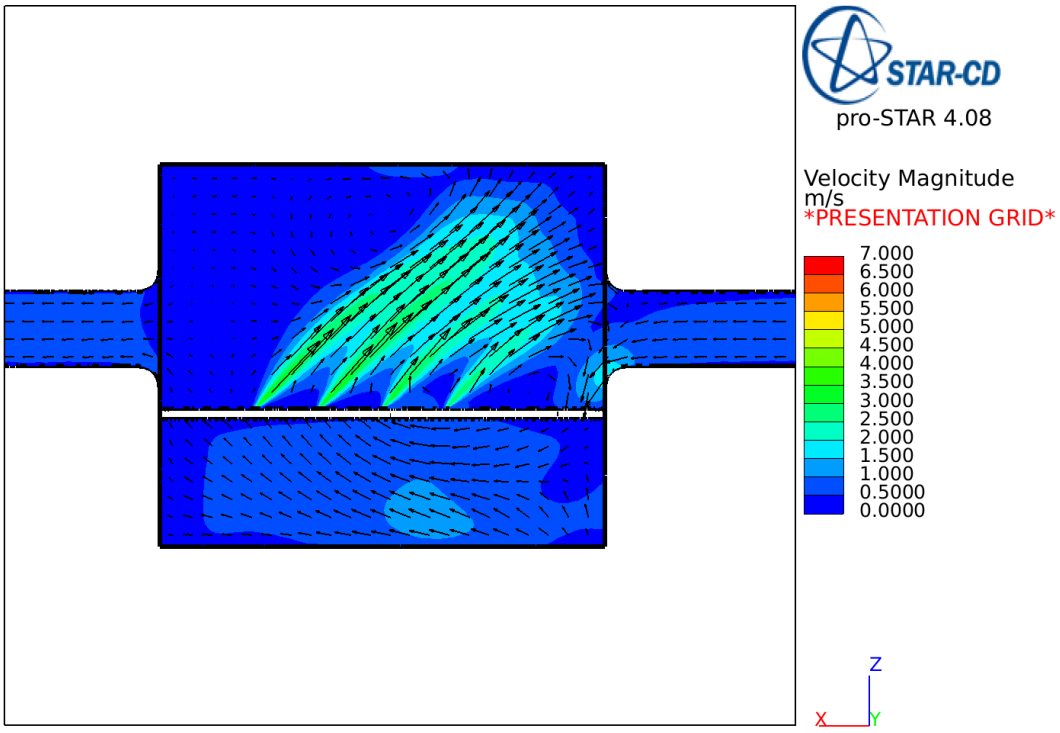

Fig. 5.22. Flow Field for AFR = 105 *ft/min* and WFR = 0.84 *gal/min*

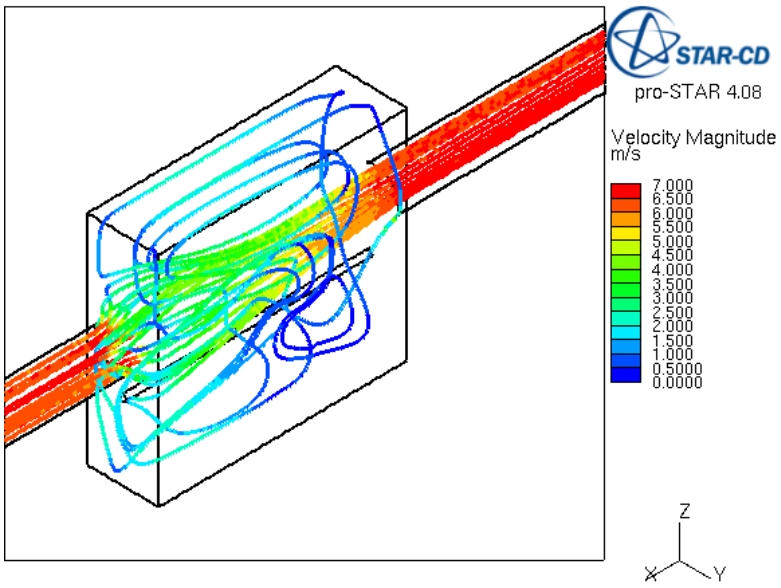

Fig. 5.23. Particle Tracks for AFR = 1250 *ft/min* and WFR = 0.84 *gal/min*

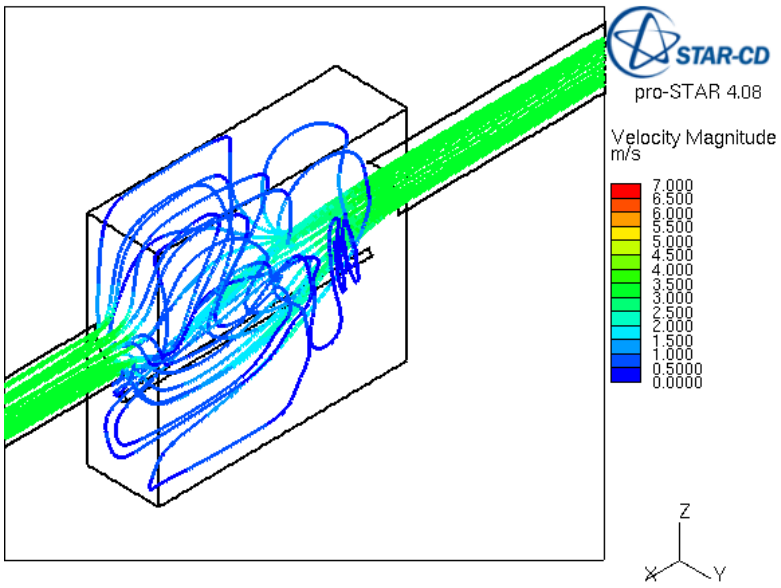

Fig. 5.24. Particle Tracks for AFR = 635 *ft/min* and WFR = 0.84 *gal/min*

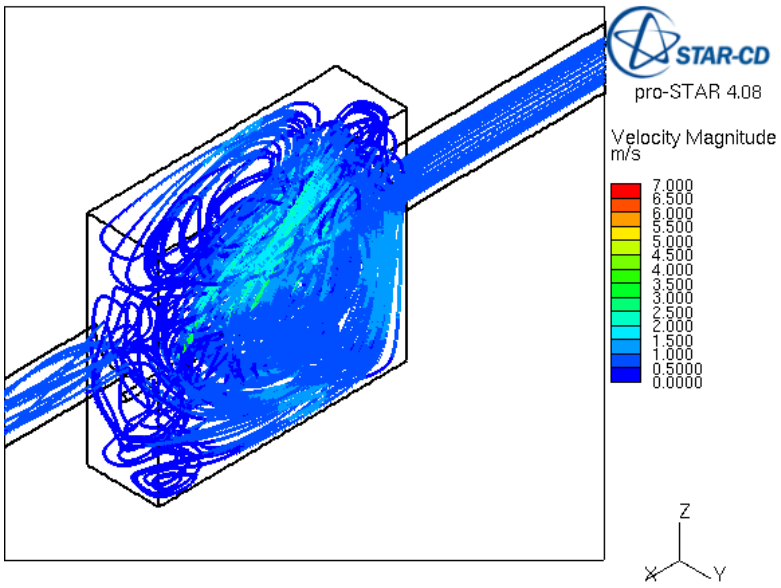

Fig. 5.25. Particle Tracks for AFR = 105 *ft/min* and WFR = 0.84 *gal/min*

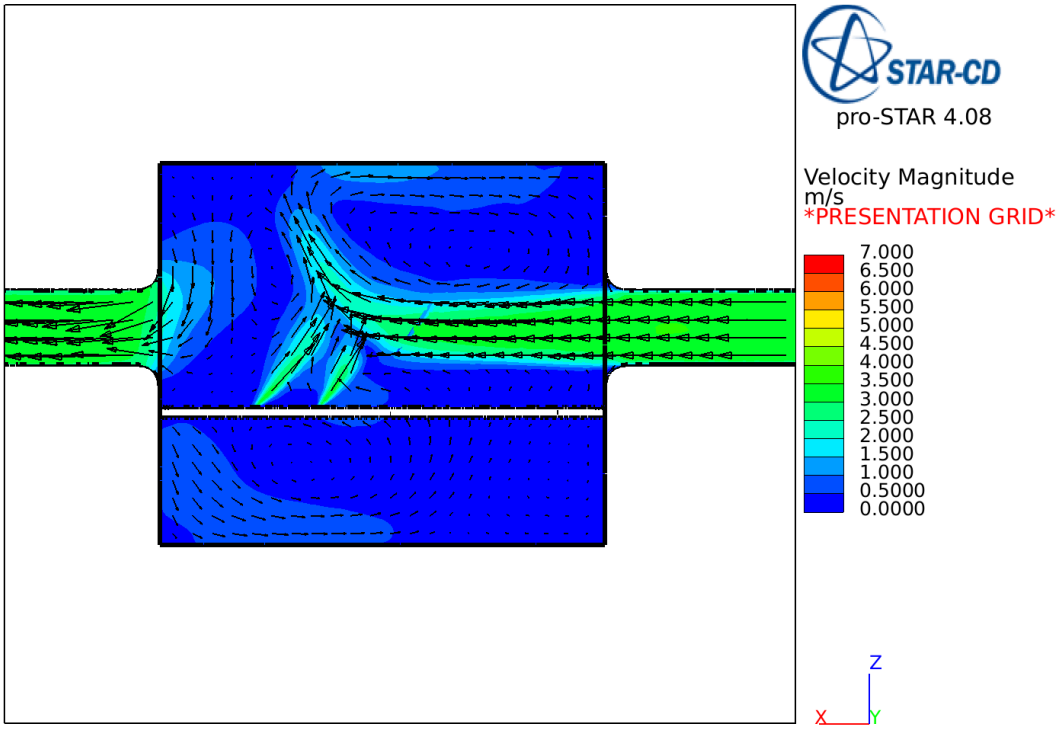

Fig. 5.26. Nozzle Configuration 2 Flow Field for AFR = 635 *ft/min* and WFR = 0.42 *gal/min*

There are two nozzle configurations used for a water flow rate of 0.42 *gpm*, as shown previously in Section 3.2. The overall collection efficiencies for these two configurations was relatively the same. This may be the result of the flow fields generated being relatively the same, as shown in Figures 5.26 and 5.27 for configuration 2 and 3, respectively. The particle tracks seem to confirm that the flow fields generated are essentially the same, since about the same number of particles get trapped in the recirculation zones.

The results in this section, to some extent, can be used to explain the particle residency time within the spray regions. The particle track figures are helpful for this purpose, but it must be kept in mind that some of these tracks may be terminated

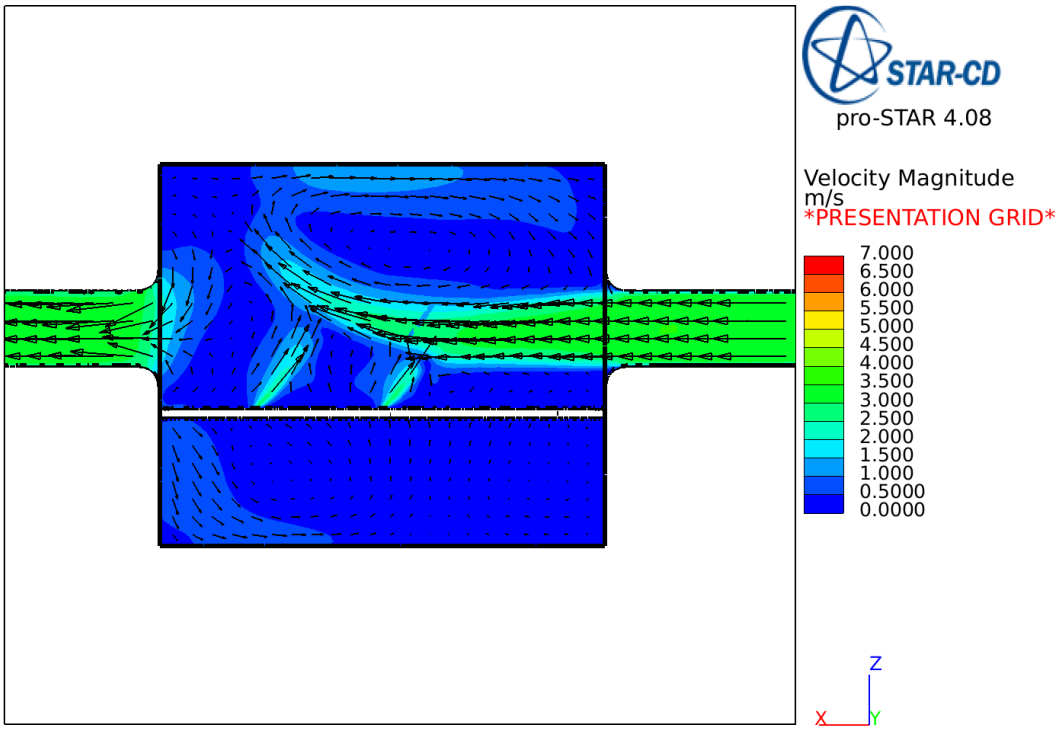

Fig. 5.27. Nozzle Configuration 3 Flow Field for AFR = 635 *ft/min* and WFR = 0.42 *gal/min*

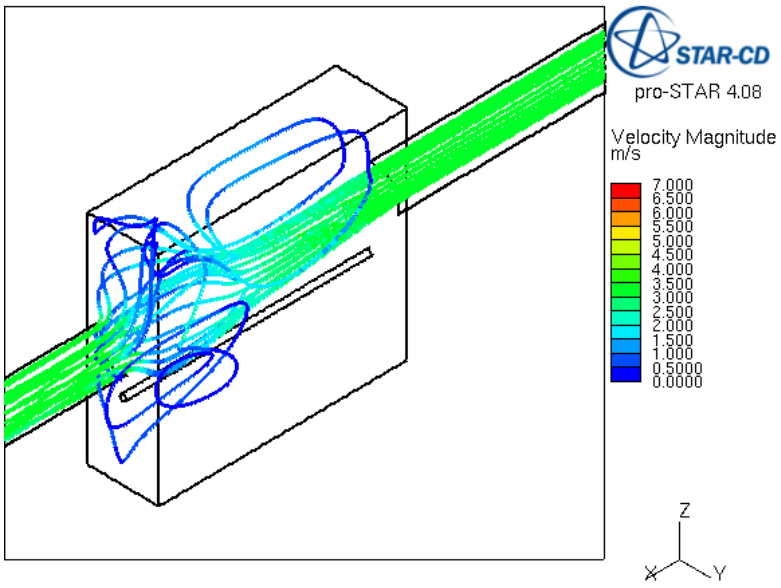

Fig. 5.28. Nozzle Configuration 2 Particle Tracks for AFR = 635 *ft/min* and WFR = 0.42 *gal/min*

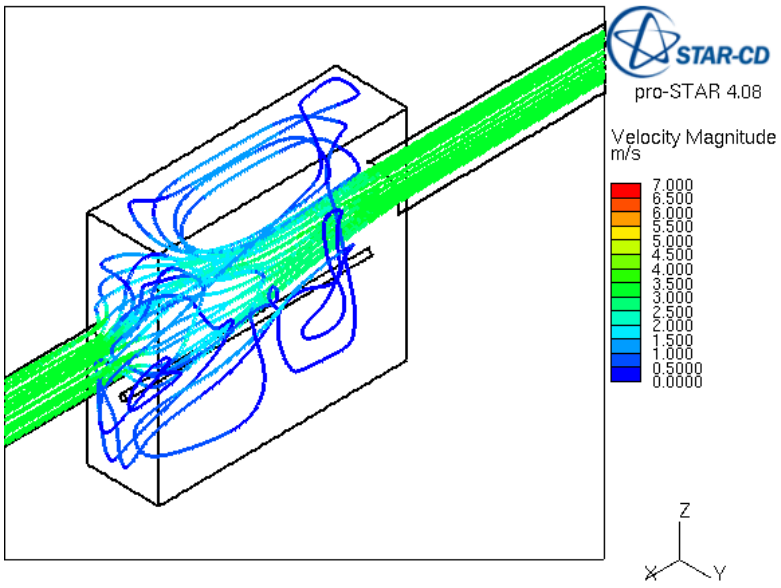

Fig. 5.29. Nozzle Configuration 3 Particle Tracks for AFR = 105 *ft/min* and WFR = 0.42 *gal/min*

by a drop-particle capture. Another important feature that should be taken from the particle track figures are that the relative velocity of the particle-drop system depends upon location and direction of both particle and drop.

6. CONCLUSIONS AND RECOMMENDATIONS

The experiment conducted proved that sprays can be used to remove airborne particulate matter and that the amount removed is directly correlated to the water flow rate and air flow rate. The result trends were expected with higher collection efficiencies at higher water flow rates and lower air flow rates. This is a result of increased residency time in the spray region, resulting in an increased probability of particle-drop interactions.

The most glaring deficiency in the experiment was that the drop size distribution and related velocity was not measured. From theoretical results it is obvious that the drop size is needed to make an estimation of collection efficiency. Not so obvious from looking at the results of Section 4.4 is that the particle-drop relative velocity is also very important when trying to theoretically determine the collection efficiency. It would be extremely beneficial to conduct experiments that measure these drop characteristics, not only for a single spray nozzle, but for multiple spray nozzles, since the sprays overlap in the current experiment.

Additional experiments should be conducted on nozzle configurations. The two configurations using for a 0.42 gpm water flow rate showed a slight difference in collection efficiency, but more data needs to be collected to make a conclusion. It would be interesting to see if other configurations could enhance the collection efficiency, include experiments that consisted of changing nozzle locations and angles into the incoming air flow.

A more difficult endeavor would be to conduct experiments that measure the effects of an electrostatic charge on collection efficiency. Theory suggests that drops and particles with opposing charges should be more readily collected. Of particular interest would be increasing collection efficiency of particles smaller than 1 μm.

Also, experiments on the collection efficiency of a discrete drop for non-wettable particles could be used to compare to the theoretical values derived in this work. It

appears from previous researchers that non-wettable particles, assuming pulverized coal dust is not water soluble, act the same as hydrophobic particles. This is based on the results of the theoretical models compared to previous researchers results in Section 4.4. Is may be possible that other mechanisms are at work, but more research would be needed.

Additional things that may help with experimentation would include building a more rigid structure and introducing the dust in a more consistent fashion. The current experiment had to be built with a wooden structure surrounded by plastic liners due to funding constraints. A more rigid structure would provide more reliable results. The dust was added in a manner that allowed varying particle number densities. Fabricating a more consistent way of introducing dust would definitely change collection results, since collection efficiency is also related to number density.

The two numerical models show promise, but no definitive conclusion can be made because the drop size distribution of the sprays was not known. The current state of the models are for a once-thru approach, where the particles pass straight through the spray region. As the CFD results show, this is not the case in the physical system. The flow fields created by the sprays create particle recirculation, which will increase their residency time.

There are two options that could increase the accuracy of the codes. The first would be to add a model to the CFD code itself. Collisions in CFD are currently only allowed between materials of the same species (e.g. drop-drop interactions). It should be possible to add a model that tracks both particles and drops in CFD and estimate the collection efficiency based on the theory found in this research, which of course is not trivial. The other option would be to discretize the current deterministic and/or Monte Carlo models. This would allow a better approximation of collection efficiency based on specific node physical characteristics.

Additional collection mechanisms could also be added to the current models. Mechanisms such as diffusiophoresis, thermophoresis, electrophoresis, turbulent cap-

ture, and wake capture, among others, have been ignored in the current models. The main reason they were excluded was because the major collection mechanism for the particle size distribution was inertial impaction and electrostatic effects were not measured. The addition of the other mechanisms would allow the code to be used for a wider range of particle sizes.

REFERENCES

[1] W.C. Hinds, Aerosol Technology: Properties, Behavior, and Measurement of Airborne Particles, 2nd ed., John Wiley & Sons, Inc., New York, NY, 1999.

[2] S.K. Friedlander, D.Y.H. Pui, Emerging issues in nanoparticle aerosol science and technology, Journal of Nanoparticle Research 6 (2) (2004) 313–320.

[3] H.R. Pruppacher, J.D. Klett, Microphysics of Clouds and Precipitation, 2nd ed., Kluwer Academic Publishers, Dordrecht, The Netherlands, 1996.

[4] C. Papastefanou, Radioactivity in the Environment Volume 12: Radioactive Aerosols, 1st ed., Elsevier, Amsterdam, The Netherlands, 2008.

[5] F.E. Haskin, A.L. Camp, S.A. Hodge, D.A. Powers, Perspectives on reactor safety, SAND93-0971, Sandia National Laboratories, Albuquerque, NM, January 1993.

[6] D.A. Petti, R.R. Hobbins, D.L. Hagrman, The composition of aerosols generated during a severe reactor accident: Experimental results from the power burst facility severe fuel damage test 1-4, Nuclear Technology 105 (3) (1994) 334–345.

[7] D.A. Powers, K.E. Washington, J.L. Sprung, S.B. Burson, A simplified model of aerosol removal by natural processes in reactor containments, NUREG/CR–6189, Nuclear Regulatory Commission, Washington, DC, July 1996.

[8] D.A. Powers, S.B. Burson, A simplified model of aerosol removal by containment sprays, NUREG/CR–5966, Nuclear Regulatory Commission, Washington, DC, June 1993.

[9] D.A. Powers, J.H. Schaperow, A simplified model of decontamination by BWR steam suppression pools, NUREG/CR–6153, Nuclear Regulatory Commission, Washington, DC, May 1997.

[10] L. Cheng, Collection of airborne dust by water sprays, Industrial & Engineering Chemistry Process Design and Development 12 (3) (1973) 221–225.

[11] T.F. Tomb, J.E. Emmerling, R.H. Kellner, Collection of airborne coal dust by water spray in a horizontal duct, American Industrial Hygiene Association Journal 33 (11) (1972) 715–721.

[12] P.R. Jonas, P. Goldsmith, The collection efficiencies of small droplets falling through a sheared air flow, Journal of Fluid Mechanics 52 (3) (1972) 593–608.

[13] A.N. Dingle, D.F. Gatz, Rain scavenging of particulate matter from the atmosphere: Final report, ORA Project 02921, University of Michigan, September 1963.

[14] P. Goldsmith, H.J. Delafield, L.C. Cox, The role of diffusiophoresis in the scavenging of radioactive particles from the atmosphere, Quarterly Journal of the Royal Meteorological Society 89 (379) (1963) 43–61.

[15] S.M. Greenfield, Rain scavenging of radioactive particulate matter from the atmosphere, Journal of the Atmospheric Sciences 14 (2) (1957) 115–125.

[16] W.E. Ranz, J.B. Wong, Impaction of dust and smoke particles on surface and body collectors, Industrial & Engineering Chemistry 44 (6) (1952) 1371–1381.

[17] W.H. Walton, A. Woolcock, The suppression of airborne dust by water spray, International Journal of Air Pollution 3 (1) (1960) 129–153.

[18] J.R. Starr, B.J. Mason, The capture of airborne particles by water drops and simulated snow crystals, Quarterly Journal of the Royal Meteorological Society 92 (394) (1966) 490–499.

[19] M.N. Golovin, A.A. Putnam, Inertial impaction on single elements, Industrial & Engineering Chemistry Fundamentals 1 (4) (1962) 264–273.

[20] K.R. May, R. Clifford, The impaction of aerosol particles on cylinders, spheres, ribbons and discs, Annals of Occupational Hygiene 10 (1) (1967) 83–95.

[21] F. Prodi, F. Tampieri, The removal of particulate matter from the atmosphere: The physical mechanisms, Pure and Applied Geophysics 120 (2) (1982) 286–325.

[22] S.L. Soo, Fluid Dynamics of Multiphase Systems, 1st ed., Blaisdell, Waltham, Massachusetts, 1967.

[23] I. Langmuir, K.B. Blodgett, A mathematical investigation of water droplet trajectories, Army Air Forces Technical Report 5418 (1) (1946) 65–208.

[24] C.J. Stairmand, Dust collection by impingement and diffusions, Chemical Engineering Research and Design 28 (a) (1950) 130–139.

[25] A.C. Chamberlain, Aspects of travel and depostion of aerosol and vapour clouds, AERE-HP/R-1261, Atomic Energy Research Establishment, Harwell, Berks,(England), September 1953.

[26] R.G. Dorsch, P.G. Saper, C.F. Kadow, Impingement of water droplets on a sphere, NACA TN 3587, National Advisory Committee for Aeronautics, November 1955.

[27] M.J. Pilat, A. Prem, Calculated particle collection efficiencies of single droplets including inertial impaction, brownian diffusion, diffusiophoresis and thermophoresis, Atmospheric Environment 10 (1) (1976) 13–19.

[28] C.S. Pemberton, Scavenging action of rain on non-wettable particulate matter suspended in the atmosphere, International Journal of Air Pollution 30 (1) (1960) 168–178.

[29] W.G.N. Slinn, C.L. Simpson, Analytical investigations of inertial deposition of small aerosol particles from laminar flows onto large obstacles. Part B. Large stokes number solution by the method of matched asymptotic expansion, BNWL 1850 PT3, Battelle Pacific Northwest Laboratory, April 1974.

[30] C.R. McCully, M. Fisher, G. Langer, J. Rosinski, H. Glaess, D. Werle, Scavenging action of rain on air-borne particulate matter, Industrial & Engineering Chemistry 48 (9) (1956) 1512–1516.

[31] E. Porcheron, P. Lemaitre, D. Marchand, W. Plumecocq, A. Nuboer, J. Vendel, Experimental and numerical approaches of aerosol removal in spray conditions for containment application, October, 2008, 12th International Topical Meeting on Nuclear Reactor Thermal Hydraulics.

[32] A.H. Lefebvre, X.F. Wang, C.A. Martin, Spray characteristics of aerated-liquid pressure atomizers, Journal of Propulsion 4 (4) (1988) 293–298.

[33] T. Han, D.L. O'Neal, C.A. Ortiz, A generic-tee-plenum mixing system for application to single point aerosol sampling in stacks and ducts, Health Physics 92 (1) (2007) 40–49.

[34] K. Willeke, Baron P.A., Aerosol Measurement: Principles, Techniques, and Applications, 1st ed., Van Nostrand Reinhold, New York, NY, 1993.

[35] Spary Systems Co., Industrial spray products, Catalog 70, Spray Systems Co., January 2009.

[36] ISO, Road vehicles - Test dust for filter evaluation, ISO 12103-1 1997, International Organization for Standardization, December 1997.

[37] J.R. Taylor, An Introduction to Error Analysis: The Study of Uncertainties in Physical Measurements, 2nd ed., University Science Books Mill Valley, Sausalito, CA, 1997.

[38] H.R. Pruppacher, K.V. Beard, A wind tunnel investigation of the internal circulation and shape of water drops falling at terminal velocity in air, Quarterly Journal of the Royal Meteorological Society 96 (408) (1970) 247–256.

[39] X-5 Monte Carlo Team, A general monte carlo n-particle transport code, version 5, volume i: Overview and theory, LA-UR-03-1987, Los Alamos National Laboratory, April 2003.

[40] G.K. Batchelor, An Introduction to Fluid Mechanics, 1st ed., Cambridge University Press, Cambridge, MA, 1967.

[41] I.G. Currie, Fundamental Mechanics of Fluids, 3rd ed., Marcel Dekker, New York, NY, 2003.

[42] J.R. Welty, C.E. Wicks, R.E. Wilson, G. Rorrer, Fundamentals of Momentum, Heat, and Mass Transfer, 4th ed., John Wiley & Sons, Inc, New York, NY, 2001.

[43] K.R. Spurny, Advances in Aerosol Filtration, 1st ed., Lewis Publishers, Boca Raton, FL, 1998.

[44] D. Zwillinger, CRC Standard Mathematical Tables and Formulae, 31st ed., Chapman & Hall, Boca Raton, FL, 2003.

[45] CD-Adapco, Methodology, Version 4.08, CD-Adapco, January 2008.

[46] M. St-Georges, J.M. Buchlin, Detailed single spray experimental measurements and one-dimensional modelling, International Journal of Multiphase Flow 20 (6) (1994) 979–992.

[47] M. St-Georges, J.M. Buchlin, M.L. Riethmuller, J.P. Lopez, J. Lieto, F. Griolet, Fundamental multidisciplinary study of liquid sprays for absorption of pollutant or toxic clouds, Process Safety and Environmental Protection 70 (b) (1992) 205–213.

APPENDIX A. RAW DATA

The raw data collected for the experiment will be presented in a series of tables. The pump flow rate were the values taken previous to introducing the aerosols. Nozzle configurations are represented by Figure 3.4.

Table A.1
Raw Data for WFR = 0.00 *gpm* for AFR = 105 & 1250 *ft/min*

						1^{st} *Weighing*	2^{nd} *Weighing*
Air Flow Velocity [***ft/min***]	**Nozzle Configuration**	**Delta Time** [***sec***]	**Location**	**Pump Flow Rate** [***SCFH***]	**Initial Weight** [***grams***]	**Final Weight** [***grams***]	**Final Weight** [***grams***]
105	–	60	Upstream	135	2.2504	2.3304	2.3301
			Downstream	135	2.3089	2.3628	2.3626
105	–	60	Upstream	135	2.3141	2.3912	2.3909
			Downstream	135	2.3325	2.3786	2.3788
105	–	60	Upstream	135	2.2541	2.3519	2.3519
			Downstream	135	2.2313	2.2946	2.2948
105	–	60	Upstream	135	2.3014	2.3816	2.3807
			Downstream	135	2.2826	2.3340	2.3338
105	–	60	Upstream	135	2.2566	2.3440	2.3449
			Downstream	135	2.2910	2.3473	2.3473
1250	–	60	Upstream	132	2.3275	2.3461	2.3462
			Downstream	130	2.2866	2.3056	2.3059
1250	–	60	Upstream	132	2.3205	2.3337	2.3345
			Downstream	130	2.3017	2.3156	2.3169

Table A.2
Raw Data for WFR = 0.00 *gpm* and AFR = 635 *ft/min*

						1^{st} *Weighing*	2^{nd} *Weighing*
Air Flow Velocity [***ft/min***]	**Nozzle Configuration**	**Delta Time** [***sec***]	**Location**	**Pump Flow Rate** [***SCFH***]	**Initial Weight** [***grams***]	**Final Weight** [***grams***]	**Final Weight** [***grams***]
635	–	180	Upstream	128	2.2742	2.2989	2.2986
			Downstream	128	2.2975	2.3182	2.3182
635	–	120	Upstream	128	2.2942	2.3196	2.3188
			Downstream	128	2.2684	2.2885	2.2881
635	–	120	Upstream	128	2.3549	2.3794	2.3790
			Downstream	128	2.2734	2.2930	2.2929
635	–	120	Upstream	132	2.2700	2.2854	2.2867
			Downstream	128	2.3126	2.3290	2.3301
635	–	120	Upstream	128	2.2735	2.2903	2.2912
			Downstream	128	2.2980	2.3154	2.3168
635	–	120	Upstream	128	2.4423	2.4678	2.4681
			Downstream	128	2.2744	2.2990	2.2993
635	–	120	Upstream	128	2.2725	2.2948	2.2952
			Downstream	128	2.2815	2.3031	2.3034

Table A.3
Raw Data for WFR = 0.42 *gpm* and Nozzle Configuration 2

						1^{st} *Weighing*	2^{nd} *Weighing*
Air Flow Velocity [***ft/min***]	**Nozzle Configuration**	**Delta Time** [***sec***]	**Location**	**Pump Flow Rate** [***SCFH***]	**Initial Weight** [***grams***]	**Final Weight** [***grams***]	**Final Weight** [***grams***]
635	2	120	Upstream	128	2.2387	2.2601	2.2598
			Downstream	128	2.2652	2.2796	2.2795
635	2	120	Upstream	128	2.4684	2.4931	2.4930
			Downstream	128	2.4227	2.4472	2.4474
635	2	120	Upstream	128	2.3833	2.4078	2.4080
			Downstream	128	2.4897	2.5031	2.5034
635	2	120	Upstream	128	2.4503	2.4708	2.4708
			Downstream	128	2.4269	2.4395	2.4392
635	2	120	Upstream	128	2.4251	2.4513	2.4510
			Downstream	128	2.4524	2.4672	2.4671
635	2	120	Upstream	128	2.4138	2.4356	2.4352
			Downstream	128	2.3984	2.4111	2.4107
635	2	120	Upstream	130	2.4311	2.4564	2.4562
			Downstream	128	2.4396	2.4543	2.4545

Table A.4
Raw Data for WFR = 0.42 *gpm* and Nozzle Configuration 3

						1^{st} *Weighing*	2^{nd} *Weighing*
Air Flow Velocity [***ft/min***]	**Nozzle Configuration**	**Delta Time** [***sec***]	**Location**	**Pump Flow Rate** [***SCFH***]	**Initial Weight** [***grams***]	**Final Weight** [***grams***]	**Final Weight** [***grams***]
635	3	120	Upstream	130	2.2981	2.3170	2.3167
			Downstream	128	2.3318	2.3456	2.3450
635	3	120	Upstream	130	2.2661	2.2838	2.2833
			Downstream	128	2.3383	2.3508	2.3509
635	3	120	Upstream	128	2.3095	2.3308	2.3311
			Downstream	128	2.2302	2.2455	2.2457
635	3	120	Upstream	128	2.2790	2.2965	2.2969
			Downstream	128	2.2755	2.2876	2.2878
635	3	120	Upstream	128	2.4507	2.4721	2.4725
			Downstream	128	2.4639	2.4778	2.4780
635	3	120	Upstream	128	2.4165	2.4380	2.4381
			Downstream	128	2.3818	2.3960	2.3957
635	3	120	Upstream	128	2.4721	2.4941	2.4945
			Downstream	128	2.4930	2.5069	2.5072

Table A.5
Raw Data for WFR = 0.84 *gpm* and AFR = 105 *ft/min*

						1^{st} *Weighing*	2^{nd} *Weighing*
Air Flow Velocity [***ft/min***]	**Nozzle Configuration**	**Delta Time** [***sec***]	**Location**	**Pump Flow Rate** [***SCFH***]	**Initial Weight** [***grams***]	**Final Weight** [***grams***]	**Final Weight** [***grams***]
105	1	60	Upstream	132	2.2977	2.3986	2.3988
			Downstream	132	2.3490	2.3810	2.3810
105	1	60	Upstream	132	2.2904	2.3534	2.3534
			Downstream	132	2.2966	2.3127	2.3126
105	1	60	Upstream	132	2.2977	2.3986	2.3988
			Downstream	132	2.3490	2.3810	2.3810
105	1	60	Upstream	132	2.2724	2.3339	2.3338
			Downstream	130	2.3072	2.3243	2.3247
105	1	60	Upstream	130	2.3031	2.3987	2.3993
			Downstream	132	2.2877	2.3180	2.3182
105	1	60	Upstream	132	2.2681	2.3490	2.3490
			Downstream	132	2.3363	2.3614	2.3614

Table A.6
Raw Data for WFR = 0.84 *gpm* and AFR = 1250 *ft/min*

						1^{st} *Weighing*	2^{nd} *Weighing*
Air Flow Velocity [***ft/min***]	**Nozzle Configuration**	**Delta Time** [***sec***]	**Location**	**Pump Flow Rate** [***SCFH***]	**Initial Weight** [***grams***]	**Final Weight** [***grams***]	**Final Weight** [***grams***]
1250	1	60	Upstream	132	2.2506	2.2633	2.2636
			Downstream	130	2.3423	2.3528	2.3533
1250	1	60	Upstream	130	2.3211	2.3351	2.3351
			Downstream	132	2.3204	2.3310	2.3311
1250	1	60	Upstream	130	2.3185	2.3324	2.3326
			Downstream	130	2.3847	2.3953	2.3953
1250	1	60	Upstream	130	2.4954	2.5069	2.5070
			Downstream	130	2.3230	2.3320	2.3321

Table A.7
Raw Data #1 for WFR = 0.84 *gpm* and AFR = 635 *ft/min*

						1^{st} *Weighing*	2^{nd} *Weighing*
Air Flow Velocity [***ft/min***]	**Nozzle Configuration**	**Delta Time** [***sec***]	**Location**	**Pump Flow Rate** [***SCFH***]	**Initial Weight** [***grams***]	**Final Weight** [***grams***]	**Final Weight** [***grams***]
635	1	152	Upstream	130	2.3538	2.3746	2.3740
			Downstream	130	2.3913	2.4029	2.4017
635	1	183	Upstream	130	2.4296	2.4518	2.4511
			Downstream	130	2.3932	2.4038	2.4031
635	1	171	Upstream	130	2.3106	2.3339	2.3332
			Downstream	130	2.4690	2.4805	2.4801
635	1	194	Upstream	130	2.2874	2.3182	2.3179
			Downstream	130	2.2590	2.2768	2.2768
635	1	140	Upstream	130	2.2842	2.3011	2.3008
			Downstream	130	2.2486	2.2571	2.2570
635	1	168	Upstream	130	2.3172	2.3400	2.3399
			Downstream	130	2.2933	2.3053	2.3051
635	1	176	Upstream	130	2.2425	2.2624	2.2616
			Downstream	130	2.2513	2.2608	2.2599

Table A.8
Raw Data #2 for WFR = 0.84 *gpm* and AFR = 635 *ft/min*

						1^{st} *Weighing*	2^{nd} *Weighing*
Air Flow Velocity [***ft/min***]	**Nozzle Configuration**	**Delta Time** [***sec***]	**Location**	**Pump Flow Rate** [***SCFH***]	**Initial Weight** [***grams***]	**Final Weight** [***grams***]	**Final Weight** [***grams***]
635	1	120	Upstream	128	2.2835	2.3127	2.3126
			Downstream	128	2.2698	2.2824	2.2822
635	1	120	Upstream	128	2.3214	2.3535	2.3529
			Downstream	128	2.3227	2.3365	2.3357
635	1	120	Upstream	128	2.3530	2.3831	2.3828
			Downstream	129	2.2411	2.2544	2.2537
635	1	120	Upstream	128	2.2699	2.3028	2.3022
			Downstream	129	2.3121	2.3258	2.3250
635	1	120	Upstream	128	2.3072	2.3419	2.3415
			Downstream	128	2.3045	2.3192	2.3188
635	1	120	Upstream	128	2.2679	2.3119	2.3119
			Downstream	128	2.2899	2.3094	2.3090
635	1	120	Upstream	129	2.3181	2.3572	2.3572
			Downstream	128	2.2785	2.2951	2.2948

APPENDIX B. POST-PROCESSED RESULTS

This appendix presents the post-processed experimental results for collection efficiency and non-dimensionalized number density along with the corresponding uncertainties. The results are sorted by the water flow rate. The order of the results directly correspond to the tables in the previous appendix.

Table B.1
Post-Processed Data for WFR = 0.00 *gpm* for AFR = 105 *ft/min* and 1250 *ft/min*

	1^{st} ***weighing***	2^{nd} ***weighing***	1^{st} ***weighing***	2^{nd} ***weighing***
Air Flow Velocity [*ft/min*]	**Collection Efficiency**	**Collection Efficiency**	**Non-Dimensional Number Density**	**Non-Dimensional Number Density**
105	0.326 ± 0.014	0.326 ± 0.014	0.811 ± 0.106	0.806 ± 0.106
105	0.402 ± 0.013	0.397 ± 0.013	0.781 ± 0.102	0.777 ± 0.102
105	0.353 ± 0.013	0.351 ± 0.013	0.991 ± 0.130	0.989 ± 0.130
105	0.359 ± 0.013	0.354 ± 0.013	0.813 ± 0.106	0.802 ± 0.106
105	0.356 ± 0.013	0.362 ± 0.013	0.886 ± 0.116	0.893 ± 0.116
1250	-0.006 ± 0.021	-0.016 ± 0.021	0.015 ± 0.002	0.016 ± 0.002
1250	-0.037 ± 0.026	-0.069 ± 0.025	0.011 ± 0.001	0.012 ± 0.001

Table B.2
Post-Processed Data for WFR = 0.00 *gpm* for AFR = 635 *ft/min*

	1^{st} ***weighing***	2^{nd} ***weighing***	1^{st} ***weighing***	2^{nd} ***weighing***
Air Flow Velocity [*ft/min*]	**Collection Efficiency**	**Collection Efficiency**	**Non-Dimensional Number Density**	**Non-Dimensional Number Density**
635	0.162 ± 0.019	0.152 ± 0.019	0.013 ± 0.002	0.013 ± 0.002
635	0.209 ± 0.018	0.199 ± 0.018	0.020 ± 0.002	0.020 ± 0.002
635	0.200 ± 0.018	0.191 ± 0.019	0.019 ± 0.002	0.019 ± 0.002
635	-0.033 ± 0.024	-0.016 ± 0.023	0.013 ± 0.001	0.014 ± 0.001
635	-0.036 ± 0.023	-0.062 ± 0.023	0.013 ± 0.002	0.014 ± 0.002
635	0.035 ± 0.019	0.035 ± 0.019	0.020 ± 0.002	0.020 ± 0.002
635	0.031 ± 0.020	0.035 ± 0.020	0.018 ± 0.002	0.018 ± 0.002

Table B.3
Post-Processed Data for WFR = 0.42 *gpm* and Nozzle Configuration 2

	1^{st} ***weighing***	2^{nd} ***weighing***	1^{st} ***weighing***	2^{nd} ***weighing***
Air Flow Velocity [*ft/min*]	**Collection Efficiency**	**Collection Efficiency**	**Non-Dimensional Number Density**	**Non-Dimensional Number Density**
635	0.327 ± 0.019	0.322 ± 0.019	0.017 ± 0.002	0.017 ± 0.002
635	0.413 ± 0.018	0.402 ± 0.018	0.020 ± 0.002	0.020 ± 0.002
635	0.453 ± 0.018	0.445 ± 0.018	0.019 ± 0.002	0.019 ± 0.002
635	0.385 ± 0.020	0.400 ± 0.020	0.016 ± 0.002	0.016 ± 0.002
635	0.435 ± 0.018	0.432 ± 0.018	0.021 ± 0.002	0.021 ± 0.002
635	0.417 ± 0.019	0.425 ± 0.019	0.017 ± 0.002	0.017 ± 0.002
635	0.428 ± 0.018	0.416 ± 0.018	0.020 ± 0.002	0.020 ± 0.002

Table B.4
Post-Processed Data for WFR = 0.42 *gpm* and Nozzle Configuration 3

	1^{st} ***weighing***	2^{nd} ***weighing***	1^{st} ***weighing***	2^{nd} ***weighing***
Air Flow Velocity [*ft/min*]	**Collection Efficiency**	**Collection Efficiency**	**Non-Dimensional Number Density**	**Non-Dimensional Number Density**
635	0.281 ± 0.020	0.301 ± 0.021	0.015 ± 0.002	0.015 ± 0.002
635	0.305 ± 0.021	0.279 ± 0.022	0.014 ± 0.002	0.014 ± 0.002
635	0.282 ± 0.019	0.282 ± 0.019	0.017 ± 0.002	0.017 ± 0.002
635	0.309 ± 0.022	0.313 ± 0.021	0.014 ± 0.002	0.014 ± 0.002
635	0.350 ± 0.019	0.353 ± 0.019	0.017 ± 0.002	0.017 ± 0.002
635	0.340 ± 0.019	0.356 ± 0.019	0.017 ± 0.002	0.017 ± 0.002
635	0.368 ± 0.019	0.366 ± 0.019	0.017 ± 0.002	0.017 ± 0.002

Table B.5
Post-Processed Data for WFR = 0.84 *gpm* and AFR = 105 *ft/min*

	1^{st} ***weighing***	2^{nd} ***weighing***	1^{st} ***weighing***	2^{nd} ***weighing***
Air Flow Velocity [*ft/min*]	**Collection Efficiency**	**Collection Efficiency**	**Non-Dimensional Number Density**	**Non-Dimensional Number Density**
105	0.683 ± 0.014	0.683 ± 0.014	1.000 ± 0.131	1.000 ± 0.131
105	0.744 ± 0.015	0.746 ± 0.015	0.624 ± 0.082	0.624 ± 0.082
105	0.726 ± 0.014	0.719 ± 0.014	0.610 ± 0.080	0.610 ± 0.080
105	0.683 ± 0.014	0.683 ± 0.014	0.933 ± 0.122	0.933 ± 0.122
105	0.694 ± 0.014	0.694 ± 0.014	0.802 ± 0.105	0.802 ± 0.105

Table B.6
Post-Processed Data for WFR = 0.84 *gpm* and AFR = 1250 *ft/min*

	1^{st} ***weighing***	2^{nd} ***weighing***	1^{st} ***weighing***	2^{nd} ***weighing***
Air Flow Velocity [*ft/min*]	**Collection Efficiency**	**Collection Efficiency**	**Non-Dimensional Number Density**	**Non-Dimensional Number Density**
1250	0.186 ± 0.026	0.167 ± 0.026	0.011 ± 0.001	0.011 ± 0.001
1250	0.231 ± 0.025	0.224 ± 0.025	0.011 ± 0.001	0.011 ± 0.001
1250	0.237 ± 0.025	0.248 ± 0.024	0.011 ± 0.001	0.011 ± 0.001
1250	0.217 ± 0.028	0.216 ± 0.028	0.009 ± 0.001	0.009 ± 0.001

Table B.7
Post-Processed Data #1 for WFR = 0.84 *gpm* and AFR = 635 *ft/min*

	1^{st} ***weighing***	2^{nd} ***weighing***	1^{st} ***weighing***	2^{nd} ***weighing***
Air Flow Velocity [*ft/min*]	**Collection Efficiency**	**Collection Efficiency**	**Non-Dimensional Number Density**	**Non-Dimensional Number Density**
635	0.442 ± 0.019	0.485 ± 0.020	0.013 ± 0.002	0.013 ± 0.002
635	0.523 ± 0.019	0.540 ± 0.019	0.012 ± 0.001	0.012 ± 0.001
635	0.506 ± 0.018	0.509 ± 0.019	0.013 ± 0.002	0.013 ± 0.002
635	0.422 ± 0.016	0.416 ± 0.016	0.015 ± 0.002	0.015 ± 0.002
635	0.497 ± 0.022	0.494 ± 0.022	0.012 ± 0.001	0.012 ± 0.001
635	0.474 ± 0.019	0.480 ± 0.019	0.013 ± 0.002	0.013 ± 0.002
635	0.523 ± 0.020	0.550 ± 0.021	0.011 ± 0.001	0.011 ± 0.001

Table B.8
Post-Processed Data #2 for WFR = 0.84 *gpm* and AFR = 635 *ft/min*

	1^{st} ***weighing***	2^{nd} ***weighing***	1^{st} ***weighing***	2^{nd} ***weighing***
Air Flow Velocity [*ft/min*]	**Collection Efficiency**	**Collection Efficiency**	**Non-Dimensional Number Density**	**Non-Dimensional Number Density**
635	0.568 ± 0.017	0.574 ± 0.017	0.023 ± 0.003	0.023 ± 0.003
635	0.570 ± 0.017	0.587 ± 0.017	0.026 ± 0.003	0.026 ± 0.003
635	0.555 ± 0.017	0.574 ± 0.017	0.024 ± 0.003	0.024 ± 0.003
635	0.580 ± 0.016	0.597 ± 0.017	0.026 ± 0.003	0.026 ± 0.003
635	0.576 ± 0.016	0.583 ± 0.016	0.028 ± 0.003	0.028 ± 0.003
635	0.557 ± 0.015	0.566 ± 0.015	0.035 ± 0.004	0.035 ± 0.004
635	0.579 ± 0.016	0.586 ± 0.016	0.031 ± 0.004	0.031 ± 0.004

VITA

Andrew S. Goldmann, son of Michael and Pamela Goldmann, was born in the early 1980s in northern Wisconsin. He earned his bachelor's and master's degrees in nuclear engineering from the University of New Mexico in Albuquerque, NM. While working on his master's degree, he was awarded the Advanced Fuel Cycle Initiative Fellowship. His research was focused on the burnup credit of Inert Matrix Fuel in a Light Water Reactor. While attending the University of New Mexico, he worked as a student intern at Sandia National Laboratories, where he gained experience in nuclear waste and severe accident analysis fields.

On completion of his master's degree, he decided to continue his graduate studies at Texas A&M University. His research at Texas A&M University focused on the physics of aerosol capture. This research resulted in both experimental and numerical work. The experimental work took him out of his comfort zone, since his focus in the past was strictly numerical.

Dr. Goldmann's address is 129 Zachary Engineering Bulding, 3133 TAMU, College Station, TX 77843-3133, care of Dr. Yassin Hassan.